Stretto di Messina

Concessionaria per la progettazione, realizzazione e gestione del collegamento stabile tra la Sicilia e il Continente Organismo di Diritto Pubblico
(Legge n° 1158 del 17 dicembre 1971, modificata dal D.Lgs. n°114 del 24 aprile 2003)

EurolinK

# PONTE SULLO STRETTO DI MESSINA

# PROGETTO DEFINITIVO

## EUROLINK S.C.p.A.

IMPREGILO S.p.A. (MANDATARIA)
SOCIETÀ ITALIANA PER CONDOTTE D'ACQUA S.p.A. (MANDANTE)
COOPERATIVA MURATORI E CEMENTISTI - C.M.C. DI RAVENNA SOC. COOP. A.R.L. (MANDANTE)
SACYR S.A.U. (MANDANTE)
ISHIKAWAJIMA - HARIMA HEAVY INDUSTRIES CO. LTD (MANDANTE)
A.C.I. S.C.P.A. - CONSORZIO STABILE (MANDANTE)

| IL PROGETTISTA | IL CONTRAENTE GENERALE | STRETTO DI MESSINA | STRETTO DI MESSINA |
|---|---|---|---|
| COWI<br>Ing. E.M. Veje<br>Dott. Ing. E. Pagani<br>Ordine Ingegneri Milano<br>n° 15408<br>EurolinK | Project Manager<br>(Ing. P.P. Marcheselli) | Direttore Generale e<br>RUP Validazione<br>(Ing. G. Fiammenghi) | Amministratore Delegato<br>(Dott. P. Ciucci) |

PB0035_F0

| | |
|---|---|
| *Unità Funzionale* | OPERA DI ATTRAVERSAMENTO |
| *Tipo di sistema* | STUDI DI BASE |
| *Raggruppamento di opere/attività* | STUDI AERODINAMICI |
| *Opera - tratto d'opera - parte d'opera* | Generale |
| *Titolo del documento* | Prove in galleria del vento, cavi |

CODICE C G 1 0 0 0 | P | R G | D | P | S B | S 3 | 0 0 | 0 0 | 0 0 | 0 0 | 0 3 | F0

| REV | DATA | DESCRIZIONE | REDATTO | VERIFICATO | APPROVATO |
|---|---|---|---|---|---|
| F0 | 20/06/2011 | EMISSIONE FINALE | ALN | SAMI | ALN/EYA |
| | | | | | |
| | | | | | |

NOME DEL FILE: PB0035_F0_ITA.doc

# INDICE

# 1 Relazione di sintesi

La presente relazione descrive le prove in galleria del vento effettuate con l'obiettivo di acquisire i coefficienti di carico da vento per la configurazione del cavo doppio principale del Ponte sullo Stretto di Messina e per effettuare una valutazione qualitativa del rischio di instabilità *galloping* (galoppante) degli stralli.

Le prove in galleria del vento sono giustificate dal fatto che i dati rappresentativi per la configurazione del cavo doppio non sono disponibili per numeri di Reynolds sufficientemente alti, secondo quanto richiesto per poter essere rappresentativi della condizione SILS.

I risultati di queste prove indicano che i coefficienti di carichi da vento rappresentativi per gli elementi di cavo doppio, sono sostanzialmente differenti dai coefficienti validi per bassi numeri di Reynold disponibili nella letteratura. Ulteriori prove indicano due potenziali tipologie di instabilità *galloping* (galoppante) per gli stralli del ponte.

# 2 Sub-test C1

I sub-test C1 sul cavo principale sono stati eseguiti in galleria del vento ad alta pressione presso la DLR, Göttingen, Germania. Lo scopo del lavori dei sub-test C1 è allegato in Appendice 1.

## 2.1 Test con alti numeri di Reynolds

Il numero di Reynolds, Re, di una struttura cilindrica viene definito in termini di diametro del cilindro

d, velocità del flusso di innesco V, viscosità dinamica μ e densità del fluido ρ:

$$Re = \frac{\rho d V}{\mu} = \frac{dV}{\nu}$$

Il rapporto $\nu = \mu/\rho$ rappresenta la viscosità cinematica alla quale viene spesso attribuito il valore $\nu = 1{,}5 \cdot 10^{-5}$ m$^2$/s per applicazioni in ingegneria del vento. La viscosità dinamica dell'aria atmosferica può essere considerata indipendente dalla pressione ambiente, ma rappresenta una funzione debole della temperatura e a 20$^0$ C $\mu \approx 1{,}8 \cdot 10^{-5}$ kg/m/s. Anche la densità dell'aria atmosferica è una funzione debole della temperatura ed è proporzionale alla pressione ambiente. In condizioni atmosferiche ed a 20$^0$ C, la densità dinamica è $\rho \approx 1{,}2$ kg/m$^3$.

Per i cavi principali del Ponte sullo Stretto di Messina in condizione SLIS, il numero di Reynolds di fondo scala viene ottenuto sotto forma di Re ≈ 1,2 m ·70 m/s / $1{,}5 \cdot 10^{-5}$ m$^2$/s = $5{,}6 \cdot 10^6$. E' difficile ottenere un Re così elevato in una galleria del vento tradizionale a pressione ambiente, a meno che la galleria non sia molto grande e in grado di accogliere modelli sovradimensionati. Aumentando la pressione ambiente in galleria del vento al di sopra della pressione atmosferica, è possibile ottenere un Re molto alto anche con modelli piccoli. Per i test in questione, la galleria del vento pressurizzata della DLR è stata fatta funzionare fino ad una pressione di ca. 80 bar e ad una velocità del vento massima di V = 35 m/s. Con un diametro d = 0,038 del cilindro usato come modello si è ottenuto un numero di Reynolds massimo Re ≈ 80·1,2 kg/m$^3$·0,038 m ·35 m/s / $1{,}8 \cdot 10^{-5}$ kg/m/s = $7 \cdot 10^6$ che va incontro ai numeri di Reynolds di fondo scala.

## 2.2 Predisposizione del modello e misurazioni

Le prove sono state eseguite utilizzando un modello costituito da due cilindri in alluminio montato con assi parellele perpendicolari al flusso ad una distanza di 1,57·d. I cilindri sono stati lucidati fino ad ottenere una rugosità superficiale relativa di k/d ≈ $10^{-5}$ corrispondente all'incirca alla rugosità superficiale anticipata dell'avvolgimento di protezione del cavo. Uno dei cilindri è stato fissato alle pareti laterali della sezione di misura, mentre l'altro è stato collegato a ciascuna estremità ad una bilancia di forza ad estensimetri per consentire la misurazione delle forze di portanza e di resistenza in direzioni perpendicolari e parallele al flusso. La bilancia ad estensimetri è stata montata su un tavolo girevole in modo che la posizione del cilindro strumentato possa essere spostata in modo da trovarsi in posizione sopravento e sottovento rispetto al cilindro stazionario. Una vista dell'assetto a doppio cilindro nella sezione di prova rimovibile è riportata in Figura 2.1.

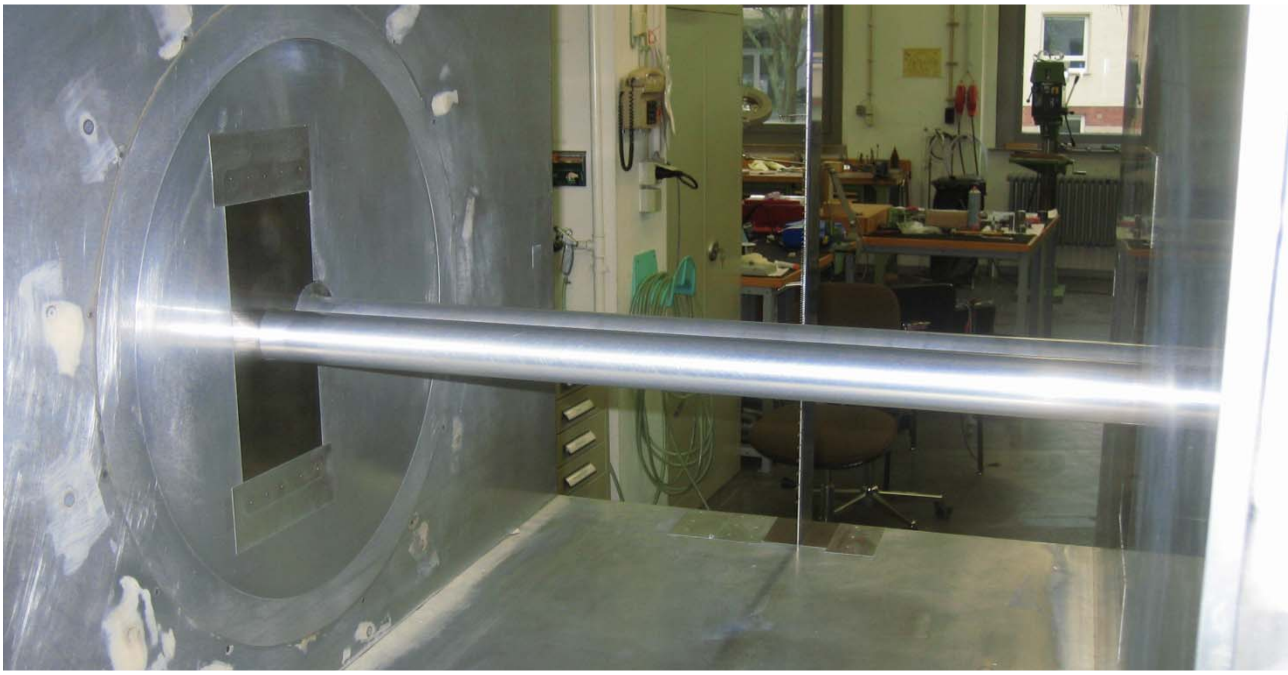

*Figura 2.1 Modello a doppio cilindro dell'assetto cavi principali in galleria del vento pressurizzata della DLR.*

Le misurazioni sono state condotte regolando innanzitutto la pressione ambiente in galleria del vento. Successivamente, il cilindro strumentato è stato posizionato sopravento rispetto al cilindro fisso, la velocità del vento è stata regolata e le forze sono state misurate negli angoli di afflusso distribuiti in un campo di - 24 deg < $\alpha$ < 24 deg con l'orizzontale con incrementi di 2 gradi. Una volta completata la posizione sopravento, il cilindro strumentato è stato spostato in posizione sottovento con ripetizione delle misurazioni ad intervalli di - 20 deg < $\alpha$ < 20 deg interval. Tale procedura è stata ripetuta per una serie di velocità del vento preimpostate e per pressioni ambiente di 20, 40, 60 e 80 bar abbracciando così un campo di numeri di Reynolds di $1{,}5 \cdot 10^5 < Re < 7 \cdot 10^6$.

In [1] viene riportato un resoconto dettagliato delle misurazioni e dei risultati.

# 3 Risultati Chiave

Le forze medie di portanza e resistenza misurate $F_{L,D}$ che agiscono sul modello di cilindro strumentato sono state rese non dimensionali mediante normalizzazione con carico dinamico $½\rho V^2$, lunghezza di estensione del modello $L_A$ e diametro del modello d allo scopo di generare i coefficienti di portanza e resistenza $C_L$, $C_D$:

$$C_{L,D} = \frac{F_{L,D}}{½\rho V^2 L_A d}$$

I segni convenzionali adottati in [1] e la presente relazione sono riportati in Figura 3.1.

**Flusso**

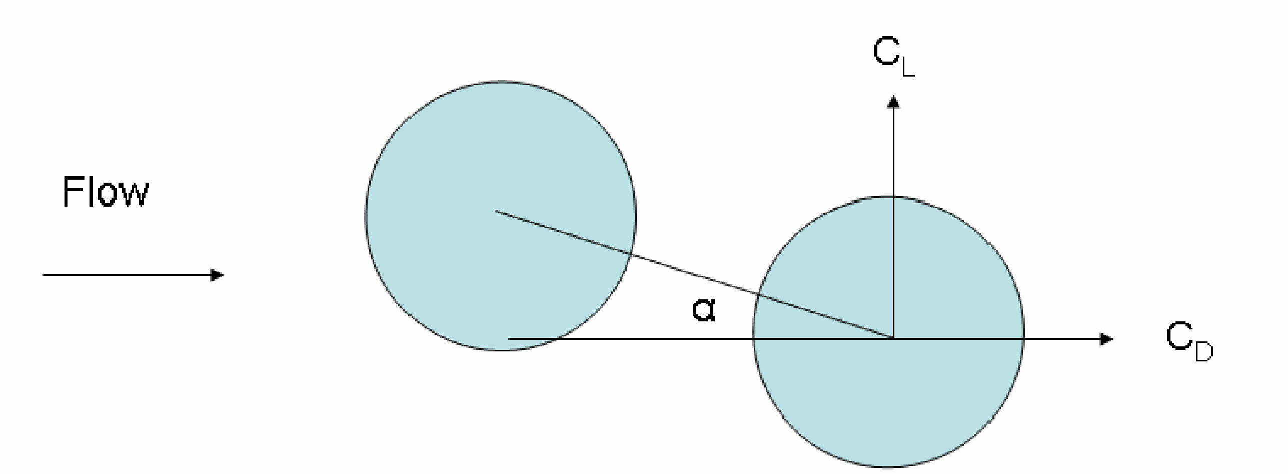


*Figura 3.1 Segni convenzionali di portanza, resistenza ed angolo di attacco adottati nel presente studio*

I risultati chiave sono presentati sotto forma di coefficiente di resistenza del cilindro sopravento ($Cyl_1$) e del cilindro sottovento ($Cyl_2$) in funzione del numero di Reynolds per il flusso in piano dei due cilindri (cioè α = 0 gradi), Figura 3.2 e coefficiente di portanza del cilindro sottovento in funzione dell'angolo di afflusso α, Figura 3.3.

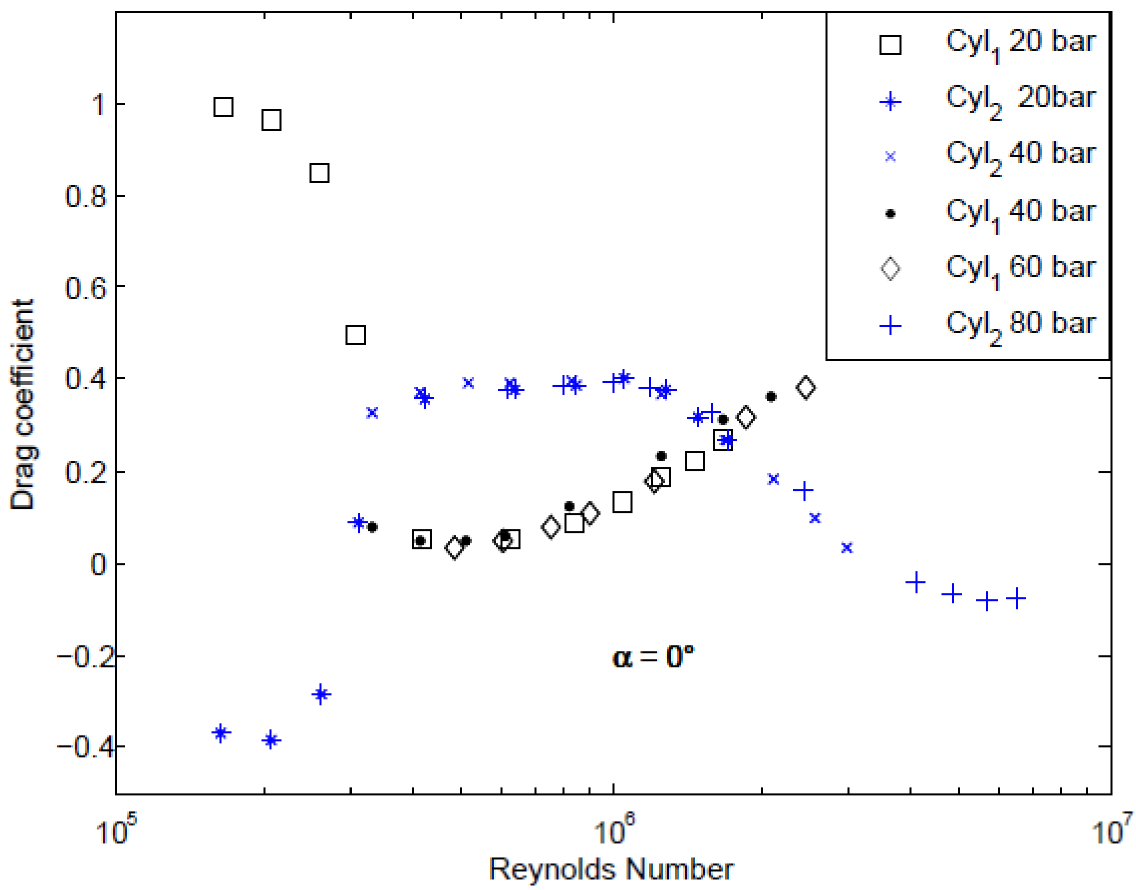


*Figura 3.2 Coefficienti di resistenza del cilindro sopravento ($Cyl_1$) e sottovento ($Cyl_2$) in funzione del Re per flusso nel piano dei due cilindri ($\alpha$ = 0 gradi).*

Dalla Figura 3.2 si nota che il coefficiente di resistenza del cavo sopravento ($Cyl_1$) assume il valore di $C_D \approx 1$ per Re sub-critico ($Re < 3 \cdot 10^5$). Nel campo critico $C_D \approx 0$ non vi è quasi carico da vento sul cavo sopravento, ma $C_D$ aumenta nuovamente nel campo super-critico. Non è stato possibile estendere le misurazioni di $C_D$ oltre $Re \approx 2 \cdot 10^6$ a causa delle gravi vibrazioni prodotte dal distacco dei vortici. Il valore asintotico del coefficiente di resistenza sul plateau con Re alto è previsto essere pari a $C_D = 0,5$ sulla base del rapporto ben noto relativo a singoli cilindri isolati. Per il cavo sottovento la tendenza è contraria in quanto si inizia con $C_D \approx -0.4$ (aspirazione) con Re sub-critico e si finisce asintoticamente con $C_D \approx -0.1$ con numeri di Reynolds supercritici, $Re \approx 7 \cdot 10^6$.

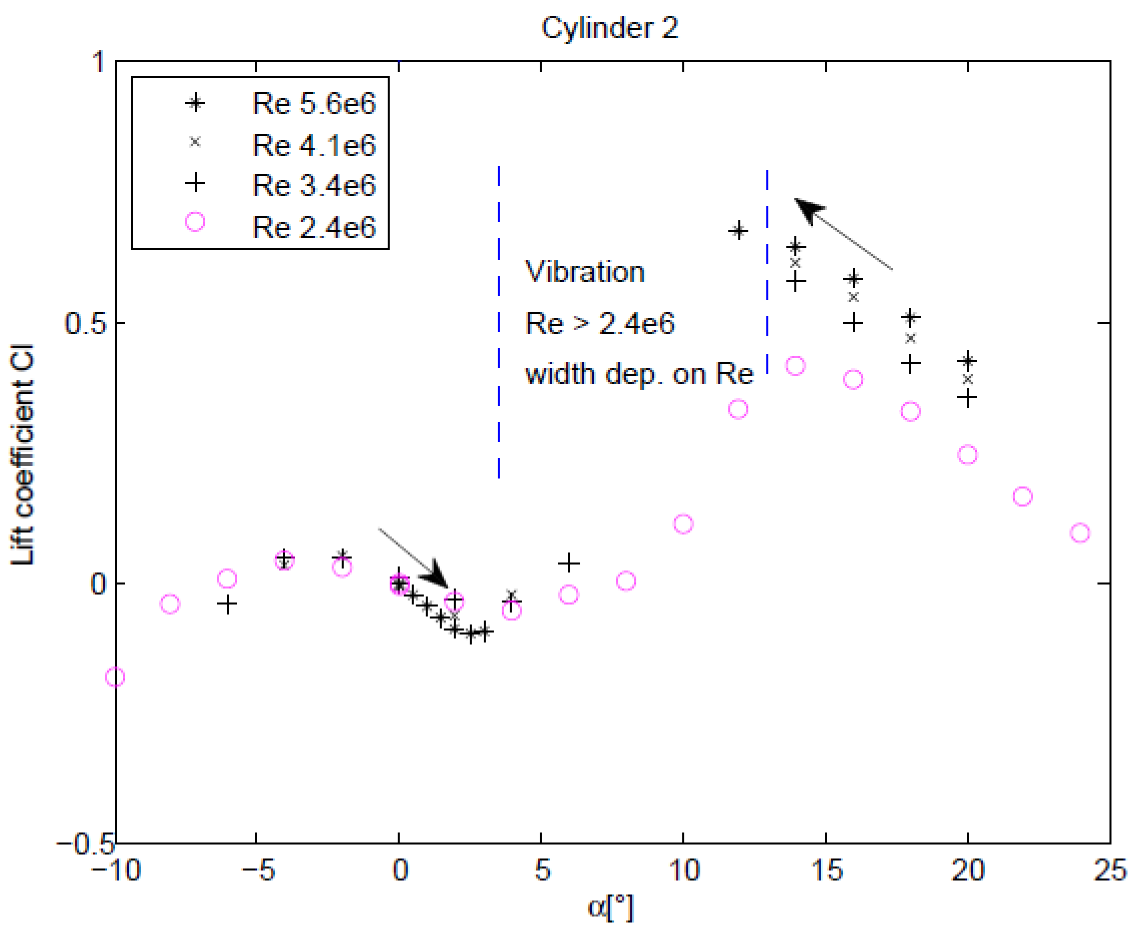


*Figura 3.3 Coefficiente di portanza del cilindro sottovento in funzione dell'angolo di afflusso $\alpha$.*

La Figura 3.3 mostra lo sviluppo del coefficiente di portanza medio $C_L$ del cavo sottovento ($Cyl_2$) in funzione dell'angolo di afflusso e con Re come parametro. Con Re bassissimo ≈ $2{\cdot}10^6$, $C_L \approx 0$ nel

campo degli angoli di afflusso $-8 < \alpha < 8$ deg, ma sale vertiginosamente a $C_L \approx 0.4$ con $\alpha = 14$ deg.

Misurazioni con Re più alti hanno dovuto essere tralasciate nel campo di afflusso $4 < \alpha < 12$ deg a

causa delle gravissime vibrazioni del cavo sottovento. Si ritiene che tali vibrazioni siano causate dal galloping di interferenza come descritto in [2] e verranno comunque trattate ulteriormente in [3].

La Figura 3.4 mostra lo sviluppo dei coefficienti medi di resistenza e di portanza $C_D$, $C_L$ del cavo sopravento ($Cyl_1$) in funzione dell'angolo di afflusso e con Re come parametro. Per l'Re massimo

raggiunto ≈ $2,4{\cdot}10^6$, si nota una peculiare diminuzione di $C_L$ nel campo di afflusso $-6 < \alpha < 6$ deg.

rappresentativa di una classica instabilità galloping den Hartog potenziale per il cavo sopravento.

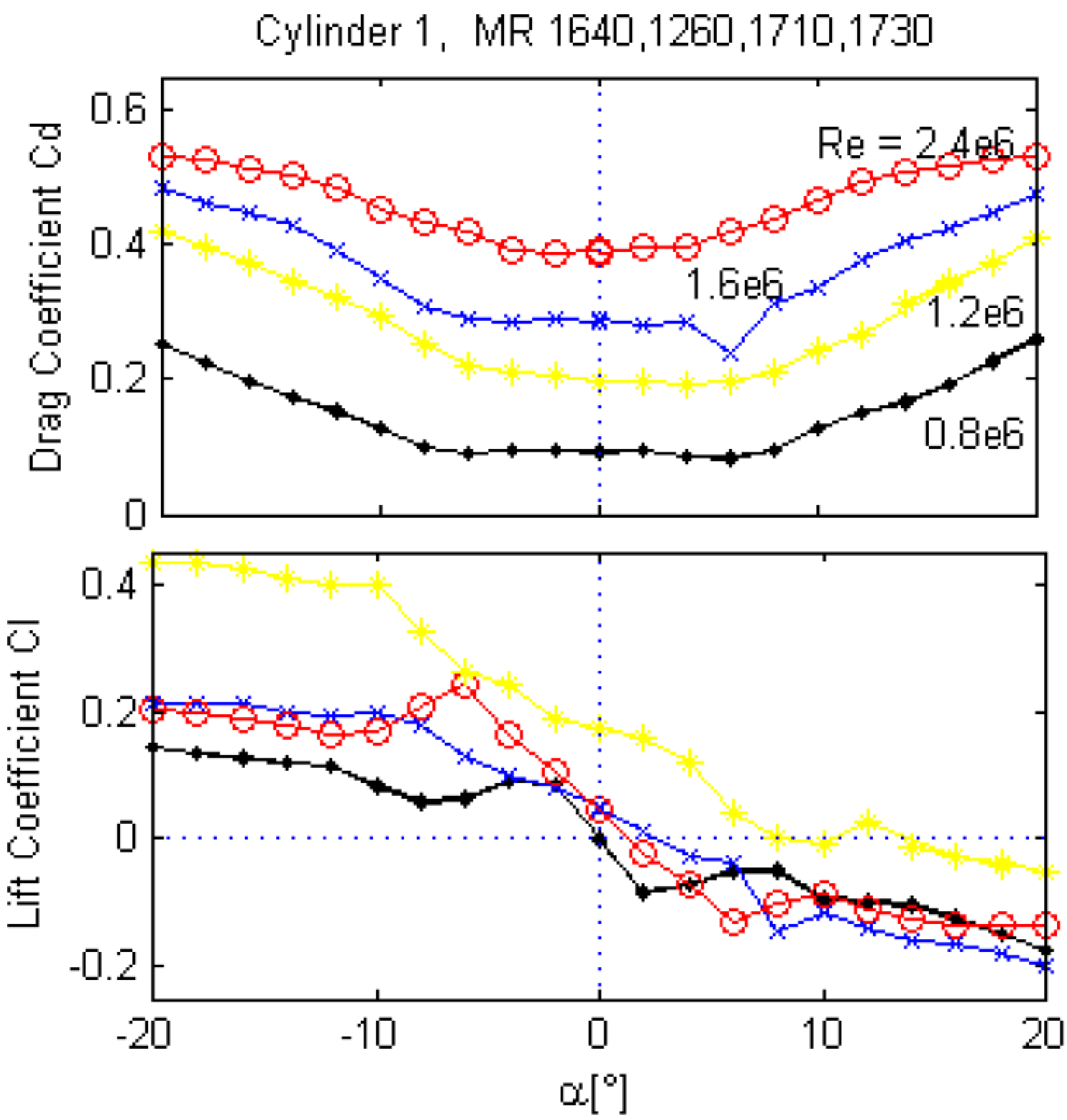


*Figura 3.4 Coefficienti di resistenza e portanza per il cilindro sopravento in funzione dell'angolo di afflusso α.*

# 4 Conclusioni

Le misurazioni dei coefficienti di portanza e resistenza per un modello di cavo principale con numeri di Reynolds di fondo scala hanno previsto coefficienti di carico da vento per il cavo principale e un'indicazione del possibile galloping di interferenza e del galloping den Hartog classico tra i due cavi.

Un confronto tra i coefficienti di portanza e di resistenza ottenuti dalle prove in questione e disponibili in letteratura [4] è presentato nella Tabella 4.1 sotto indicata.

*Tabella 4.1 Confronto tra i coefficienti di resistenza ottenuti dalle prove in questione ed i valori riscontrati in letteratura.*

| Coefficiente di resistenza $C_D$ | ESDU 70013 | Sub-test C1 in questione, distanziamento 1,57·diameter | |
|---|---|---|---|
| | $Re < 3 \cdot 10^5$ | $Re = 1.8 \cdot 10^5$ | $Re = 5.6 \cdot 10^6$ |
| Elemento sopravento | ≈1.1 | 1.0 | 0.5 |
| Elemento sottovento | ≈-0.4 | -0.4 | -0.1 |

Sulla base dei risultati del sub-test C1, verranno applicati nei calcoli di progetto i seguenti coefficienti di resistenza per il cavo principale doppio:

Cavo sopravento: $C_D = 0.5$ Cavo sottovento $C_D = -0.1$

Un'ulteriore valutazione delle potenziali instabilità galloping è presentata in [3].

# 5 Riferimenti

1 DNW-GUK report: Reynolds Number Effects in Flow around a Tandem-Cylinder from Re = $10^5$ up to $6 \cdot 10^6$. G. Schewe and M. Jacobs, 21.12.2010

2 Rusheweyh, H.: Dynamishe Windwirkung an Bauwerken 2. Bauverlag 1982

3 EUROLINK S.C.p.A. CG1000-P-CL-D-P-SB-S3-00-00-00-00-04, Rev. B/ 2011-03-07, Calcoli aerodinamici, cavi 2011.

4 ESDU data item 70013. Fluid Forces on Circular Cylinders for Application in General Engineering. Part I, Long Cylinders in Two-dimensional Flow. 1971.

# Appendice - Scopo del Lavoro

COWI

**Memo** Eurolink s.c.p.a.

**Title** Wind tunnel tests cables, Sub-tests C1, Scope of work

**Date** 7 July 2010

**To** Eurolink, EYA

**Copy** ALN

**From** SAMI

COWI A/S

Parallelvej 2
DK-2800 Kongens Lyngby
Denmark

Tel +45 45 97 22 11
Fax +45 45 97 22 12
www.cowi.com

## 1 Introduction

This memo details the scope of work for section model tests of the main cables, sub-test C1, following the overall aerodynamic design methodology for the Progetto Definitivo phase.

The objective of this test is to identify the risk of galloping oscillations of the main cable twin assembly. Experience from suspension bridges has shown that long unsupported stretches of cable bundles may enter into galloping instabilities at high wind speeds. For the Messina Bridge, the main cables are largely unsupported in the back stays with only a few hangers close to the pylons, and during construction before the deck is suspended.

## 2 Sub-test C1

Circular cross sections are known to be highly susceptible to Reynolds Number effects. It is therefore very important that the tests shall reflect the prototype Reynolds number range (up to $6 \cdot 10^6$, corresponding to a full scale wind speed of 75 m/s).

This can be achieved in the pressurised wind tunnel at DLR-Institut für Aeroelastik in Göttingen, Germany. With a maximum flow speed in the wind tunnel of 35 m/s and assuming a pressure of 70 bar, a main cable model diameter of 35 mm - 40 mm corresponds to Reynolds Numbers of approximately $6.0 \cdot 10^6$ - $6.5 \cdot 10^6$. Forces are measured in a static set-up using a piezo-electric multi-component balance.

A preliminary test using only one main cable model shall be carried out to identify the lower end of the test Reynolds Number range, defined such that the critical region where the aerodynamic forces displays a sudden drop is included.

A model representing the twin cable assembly is then tested in the same Reynolds Number range.

The measurements shall establish the force coefficients in the along wind and cross wind direction $C_x$, $C_y$ for the down wind cable model as function of the angle β between the wind direction and the line connecting the two cable model centres.

It is envisaged that β is varied in the range $-4^0$ to $20^0$ with at $2^0$ increments which may be effectuated by moving the upwind cylinder in a vertical plane. The tests are envisaged to be repeated at approximately 10 Reynolds Numbers over the test range.

The tests shall be carried out in smooth flow, $I_U < 2\%$.

## 3 Model

Preliminary contact Schewe/Larsen has indicated that DLR may be in possession of wind tunnel models which may be made available for the tests.

The surface of the main cables shall be slightly rough, corresponding to a wrapped and painted cable surface.

## 4 Data analysis and reporting

The results of test runs shall be documented in a data report, which shall also documents the particulars of the section model.

The results of the analyses shall be reported with a complete documentation of the applied procedures and observations made in course of the tests.

Test data shall be provided in digital form upon request.

## 5 Time schedule

It is envisaged that the tests can be completed and reported by mid September 2010.

Access Level II: restricted internal and restricted external access

IB 232 – 2011 C 01

G. Schewe, M. Jacobs

# Reynolds-Number Effects in Flow around a Tandem-Cylinder from Re = $10^5$ up to $6{\cdot}10^6$

Date: Jan. 2011
Contractors: EUROLINK K.S.C.p.A. Milano
Cost centre: 3004526
Cost unit: 23215

This report contains:
16 pages including
12 figures
1 table
5 references



**German Aerospace Center (DLR)**
**Institut für Aeroelastik**
**Göttingen**

# Reynolds Number-Effects in Flow around a Tandem-Cylinder from Re = $10^5$ up to $6 \cdot 10^6$


## Abstract

Force measurements on two circular cylinders in cross flow were performed for Reynolds numbers from sub- up to transcritical values. The tandem cylinder represented a twin cable assembly of the main cable of the Messina Bridge. The measurements were carried out in a special high Reynolds number facility, the DNW High Pressure Wind tunnel in Göttingen. The steady forces on each of both cylinders were measured using a both sided strain gauge balance. The Reynolds number was varied in the range from Re = $2 \cdot 10^5$ up to $6 \cdot 10^6$, the latter at a maximal pressure of p = 80 bar and a maximal wind speed of $U_{max}$ = 38 m/s. In all relevant Reynolds number ranges, for both cylinders polar diagrams were taken i.e. the dependence of the force coefficient upon the angle of incidence $\alpha$. At the maximal $\alpha$ the blockage did not exceed 10%. As given by the prototype value, the dimensionless roughness of both cylinders was $10^{-4}$ and the distance between the centres of the cylinders had a value of 1.56 times the diameter. For the purpose of comparison also the single cylinder was tested. For all configurations drastic changes of the global values depending on the Reynolds number were observed.


This report contains
16 pages including
14 figures
1 table
5 references


**German Aerospace Center (DLR)**
**Institut für Aeroelastik**
**Göttingen**

| Head of Institute | Heads of Departments | Authors |
| --- | --- | --- |
| Prof. Dr.-Ing. L. Tichy | Dr.-Ing. H. Hennings | Dr. rer. nat. G. Schewe<br>Senior scientist |
| | | Dr.-Ing. M. Jacobs<br>DNW Head of Project Management |

**Introduction**

The tests concern force measurement on two circular cylinders in cross flow, representing a twin cable assembly of the main cable of the Messina Bridge. The reason for the tests are to look for the risk of flow induced vibrations at the prototype of the bridge.
Ruscheweyh (1983) described the aeroelastic interference effects for a tandem cylinder arrangement at subcritical Reynolds numbers ($Re \approx 10^5$) as follows: Selfexcited oscillation of the downwind cylinder can occur for small distance $d/D < 3$ and when a critical angle of incidence is exceeded. Below the critical value the downstream cylinder is completely in the wake of the first one and consequently there is no lift or traverse force. Beyond the critical angle the flow is able to stream with high velocity through the gap between the two cylinders producing high negative pressure associated with high lift force on the downwind cylinder. The lift forces i.e. the across wind forces have the tendency to center the downstream cylinder, that is, draw it toward the centreline of the wake, as it is formulated in Simiu & Scanlan (1986). In the polar diagram $Cl(\alpha)$ this behaviour is reflected in a steep increase of the lift with positive slope beginning at the critical angle.
The main objective of the tests, is to find out, if this behaviour, representing aeroelastic stability and typical for subcritical Reynolds numbers is depending on the Reynolds number. The desired maximal Reynolds number is $Re \approx 6 \cdot 10^6$ based on the prototype value of the cable diameter 1.28 m and an assumed maximal wind speed of $U_{max} = 60$ m/s. The distance between the cables is 2m.
The measurements were performed in a special high Reynolds number facility, the DNW High Pressure Wind tunnel in Göttingen. This continuous running wind tunnel was especially designed for investigating civil engineering structures in incompressible flow and at very high Reynolds numbers up to $Re \approx 10^7$. Many investigations concerning Reynolds number effects in flow around bluff bodies have been performed in this facility, which are partly summarized in Schewe (2001). In particular results and interpretations about flow around single smooth cylinders can be found in Schewe (1983, 1986).
The steady forces on both cylinders were measured in individual test runs using a both sided strain gauge balance, which is mounted on a turn table. The force coefficients concern the along wind component drag Cd and the crosswind direction the lift Cl. The Reynolds No was varied in the range from $Re = 2 \cdot 10^5$ up to $6 \cdot 10^6$, the latter at a maximal pressure of $p = 80$ bar and a maximal wind speed of $U_{max} = 38$ m/s. In all relevant Reynolds No ranges, for both cylinders polar diagrams were taken i.e. the dependence of the force coefficient upon the angle of incidence $\alpha$ in the range $-20° < \alpha < 20°$. The diameter of the cylinders and with that the aspect ratio was chosen such that also at the maximal angle of incidence the blockage did not exceed 10%.
The surface roughness can play an important role regarding Reynolds number effects, thus some effort was necessary to achieve the desired dimensionless roughness given by the prototype value of $10^{-4}$.
The distance between the centres of the cylinders was rather close i.e. 1.56 times the diameter. Concerning the general test condition we can state that, the desired maximal Reynolds number was reached without compromising the size of the model, Mach number effects (0.1), blockage effects (6.3%), surface roughness or turbulence in the oncoming flow.

## Experimental Arrangement

### Wind tunnel

The high pressure wind tunnel shown in Figure 1 is built with the purpose of achieving very high Reynolds numbers in incompressible flow, thus making the tunnel ideal for wind engineering purposes. The entire wind tunnel tube, which is of the closed return type, can be pressurised up to 100 bar, which allows maximum Reynolds numbers of $10^7$ to be achieved in incompressible flow. The main particulars of the wind tunnel are as follows:

| | |
|---|---|
| • Maximum flow speed | $U = 38$ m/s |
| • Size of square test section | $0.6 \times 0.6$ $m^2$ |
| • Pressure range | $1 \leq p \leq 100$ bar |
| • Reynolds number range | $10^4 < Re < 10^7$ based on dimension $l = 0.06$ m |
| • Contraction ratio | 5.6:1 |
| • Power consumption | $N = 470$ kW |

The closed test section is 1 m long and can be removed from the wind tunnel by means of an air lock system while the tunnel tube is kept under pressure. The turbulence intensity of the flow in the test section increases slightly with increasing Re but is less than 0.4%.

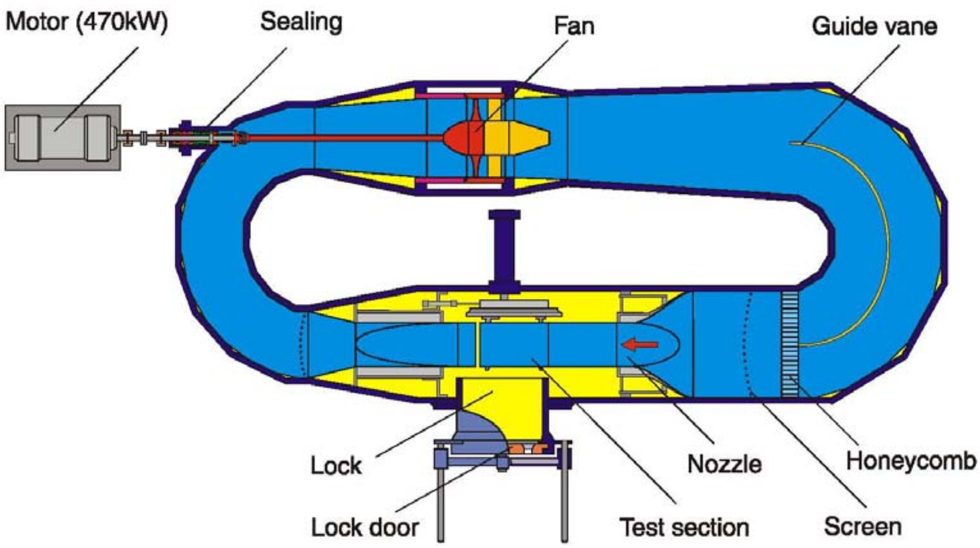


Figure 1 High pressure wind tunnel of German-Dutch Wind Tunnels (DNW) in Göttingen, Germany.

In the high pressure wind tunnel it is in principle possible to investigate the same model at Reynolds numbers spanning 3 orders of magnitude by merely varying the flow parameters.

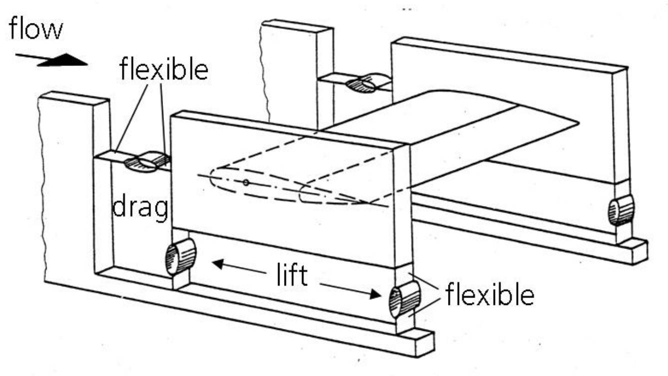


Fig. 2: Principal sketch of a strain gauge balance for 3-component force measurements. The strain gauges are affixed on the individual rings

## Strain gauge balance

Fig. 2 depicts the principle of a typical strain gauge balance for three component measurements on a two-dimensional airfoil-model. The model is fixed at both ends by a force conducting plate supported by three elastic ring elements. The ring elements, on which the strain gauges are applied, represent the force transducers. The flexible parts are necessary for the following reason: When considering for example the drag direction (x), it is obvious that a sufficient measuring deflection in the ring element for drag requires a corresponding flexibility of the lift measuring elements also in the x-direction and vice versa. In other words, the necessary measuring deflections for every component require a mechanical decoupling of the individual components, which are perpendicular to the desired one. In reality, the strain gauge balance of the High pressure wind tunnel is more sophisticated using six high end force transducers manufactured by Hottinger and special elastic elements for decoupling. The balance was oriented in such away that the main drag force was acting on the four elements, that is also the reason that the lowest eigenfrequency in drag direction is higher than in lift direction (figure 5a).

## Test Setup

The leading cylinder will be attached in such away that the angle $\alpha$ between the wind direction and the line connecting the two cylinder centres can be varied by the turn table (figure 3 and 4). The cylinder diameter is $d = 0.038$m, thus for the maximal angle desired $\alpha = 20°$ the blockage is not higher than about 10%. The distance D between the cylinders is $D/d = 1.56$.

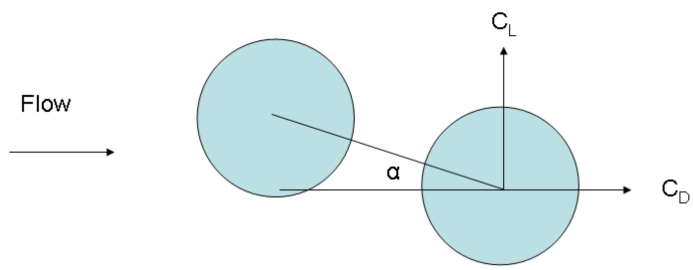


Figure 3: Coordinate system of cylinder arrangement. The cylinder under force-measurement remains always in the center of the turn table. Thus the second cylinder is moved around the central one.

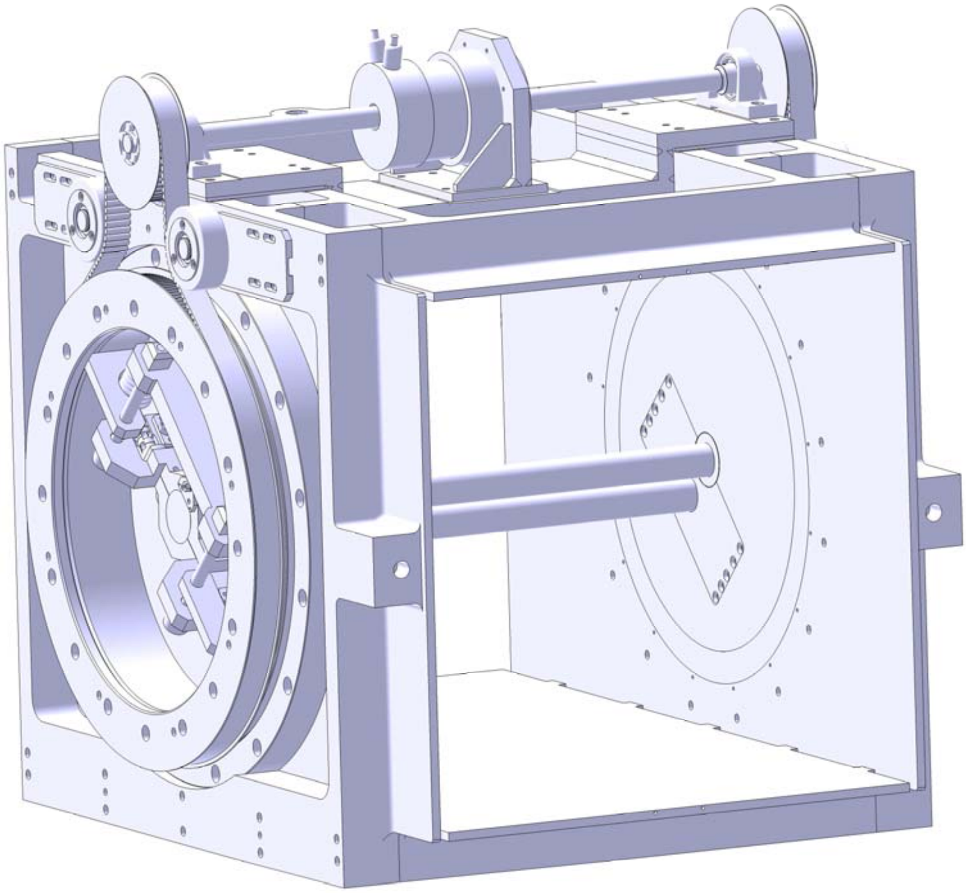

Figure 4: Test section of the DNW-High Pressure Wind Tunnel
including the tandem cylinder.

The drag- and lift forces on the cylinder in the center will be measured by a strain gauge balance. The second cylinder is mounted at the wind tunnel wall and can be rotated by the turn table (see photos). The force coefficients are presented in the fixed wind tunnel system.

**Double Cable Model and structural Properties**

The cylinders, manufactured from aluminium, were milled and then grinded down to the desired surface roughness of k = 5 µm corresponding $k/d = 10^{-4}$.
The lowest eigenfrequencies of the system balance-model (RBM) are fz = 87.3 Hz in lift- and fx = 128.4Hz (slightly increasing with pressure) in drag direction. The corresponding damping values (relative to critical) are δz = 0.35% and δx = 0.37%. The weight of the moving mass inside the balance was determined by inverting the balance and has a value of 14 kg.
D: center-to-center spacing
d: diameter of the cylinder d = 0.038 m
D/d = 1.56
Surface roughness k = 5 µm
$k/d = 10^{-4}$
Reynolds number related to d
Aspect ratio:  1: 15.8
Blockage: 6.3% for $\alpha = 0°$

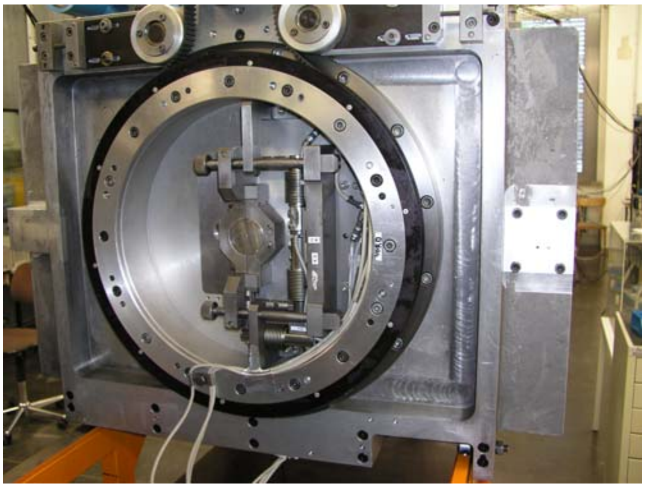

Figure 5 a: Photo of the test section, the turn table and the balance. In the centre there is the clamped cylinder under test. The three force transducer can be recognized by its bellows.

Figure 5 b:  The second cylinder is attached in holes of the walls by clamping collars.

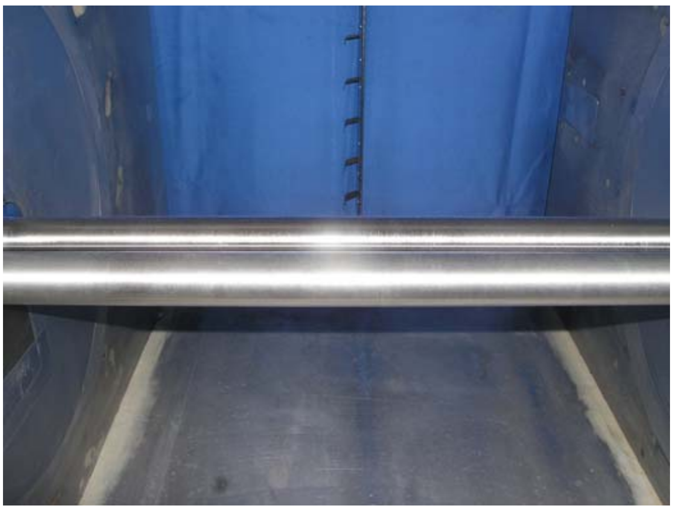

Figure 5 c: View inside the test section

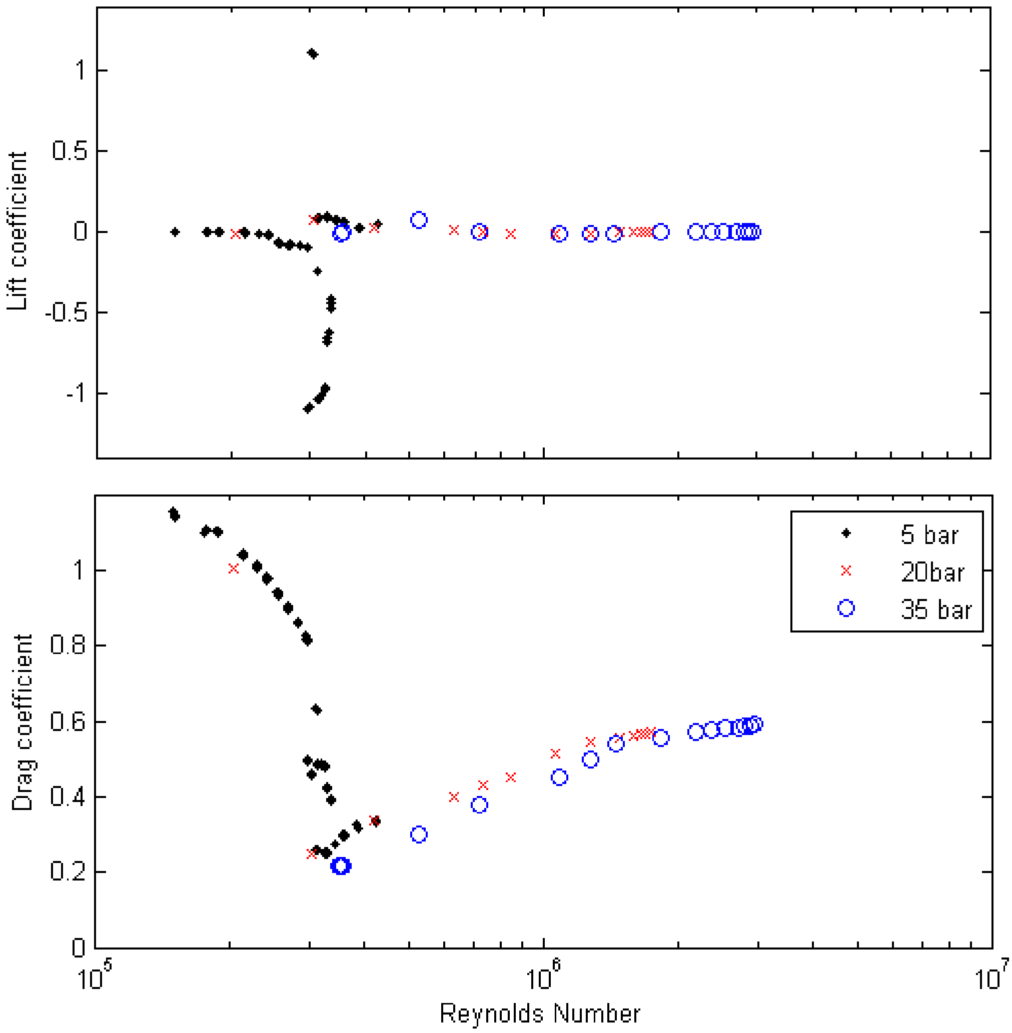


Figure 6: Drag and lift coefficient for a single cylinder depending on the Reynolds number (here roughness 1e-3)

**Results: Single Cylinder**

Figure 6 shows the drag and lift coefficient upon the Re No for a single cylinder. Other than for the following tandem arrangement the roughness related to the diameter was $k/d = 10^{-3}$, the value which was desired in a first stage of the project.
If one compares the shape of the curve with the corresponding one for a smooth circular cylinder (Schewe 1983), then it is obvious that there is no extended supercritical range with low and constant drag coefficient. But the location of the critical Re No regime at $3x10^5$ is nearly the same. Also the occurrence of steady asymmetric states, with both signs (nota bene!) could be observed, although the relative high surface roughness is nearly two orders of magnitude higher. The long transition regime begins after the drag crisis, the plateau of the transcritical range is reached at about at $Re \approx 3 - 4x10^6$ , also similar as in the case of the smooth cylinder.
It should be remarked that the differences in the transition region $3.5e5 < Re < 1e6$ is not caused by less measurement accuracy. Here the flow is very sensitive to even the smallest variations in the surface properties. In order to simulate the first version of the cable surface

structure, the model has a desired fine structure with very fine helical rills (grooves). Before the measurement at 35bar the model was cleaned. Probably the cleaning process filled up a little bit the rills, reducing the surface roughness. The consequence could be a small reduction of the drag coefficient. This effect becomes less significant when approaching transcritical Reynolds numbers.

**Results: Tandem Cylinder**

In figure 7 are plotted the drag coefficients for both individual cylinders depending on the Reynolds number at $\alpha = 0°$. The appearance of the curve for the front cylinder ($Cyl_1$) is similar to the behaviour of a single smooth circular cylinder (Schewe 1983), thus we can use the same nomenclature concerning sub-, super- and transcritical Reynolds numbers. In particular the location of the critical Reynolds number regime at $3 \cdot 10^5$ is nearly the same. There is also a long supercritical range up to about Re $\approx 10^6$. After a second rather long transition regime, the plateau of the transcritical range is reached at about at Re = $5 \cdot 10^6$. At the latest here one has to take into account that more or less regular vortex shedding may reappear.
The curve of the second cylinder is the inverse of the first one.

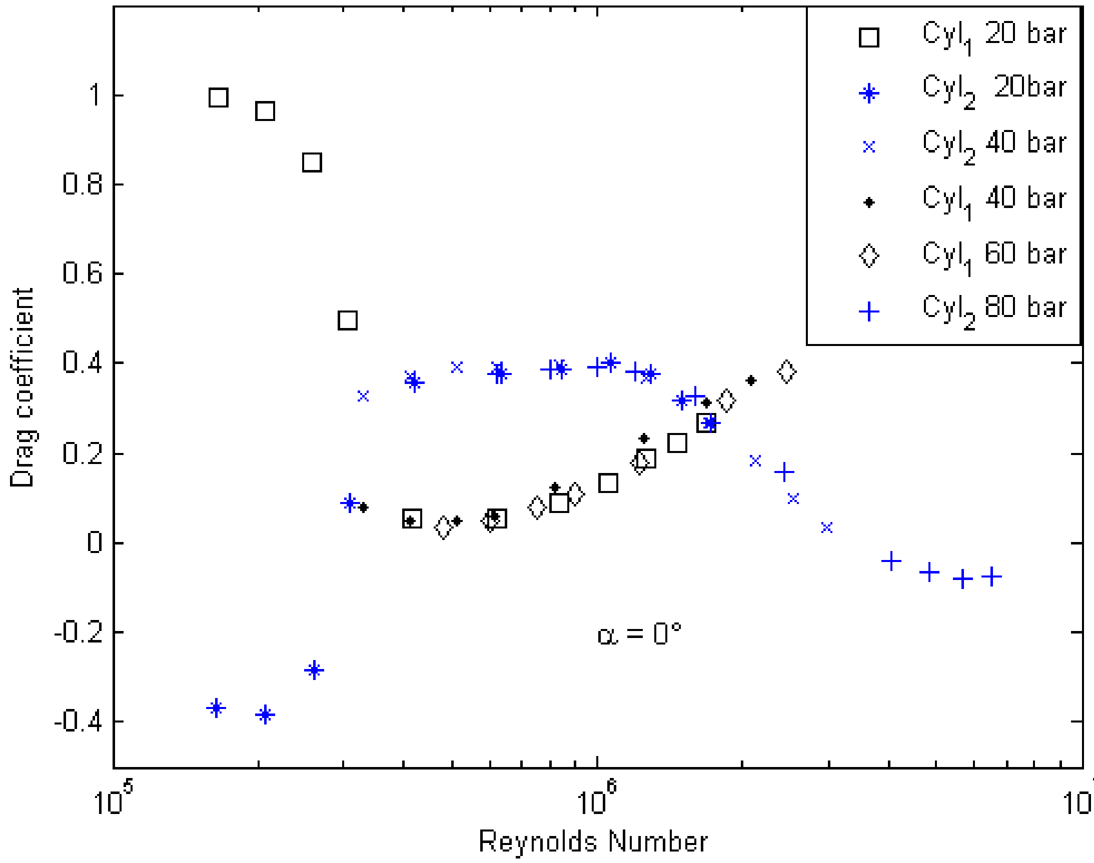

Figure 7: Drag coefficients for both individual cylinders upon the Reynolds number at $\alpha = 0°$

Concerning the tests on the first cylinder we were not able to take measurement for Re > 2.4e6. For $\alpha = 0°$ and p = 80 bar the violent vibrations in lift direction ( 87Hz ) began at a wind speed of about 14m/s (N = 300rpm) i.e. at nearly the same Re No at which we already had measured (60bar). With $\alpha = 20°$ we tried to cross the vibration range (flow speed sweep) but even at about 28 m/s (N = 600) the violent vibration did not cease, thus we had to break off.

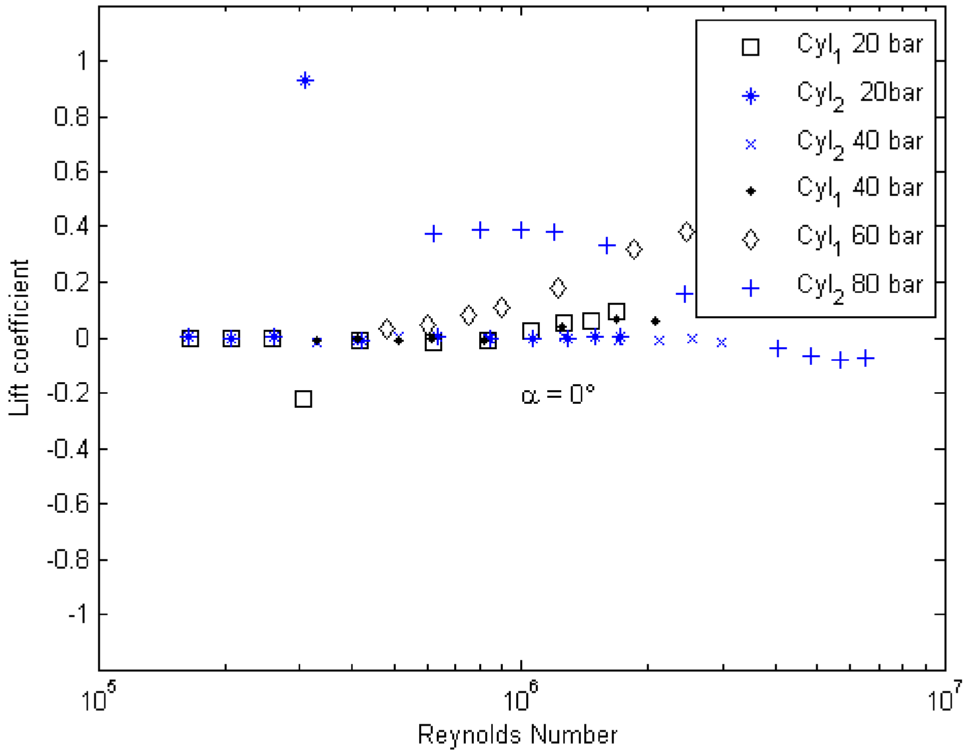


Figure 8: Lift coefficients for both individual cylinders depending on the Reynolds number at α = 0°.

Figure 8 displays the corresponding steady lift coefficients for both individual cylinders depending on the Reynolds number at α = 0°. Also in case of the tandem cylinder, in the transition regimes, there are steady asymmetric flow states as in case of a single cylinder. In the critical regime, for the downwind cylinder there is a steady lift force of Cl ≈ 1. We can imagine that, if we had repeated the experiment several times, then also the other sign would have been occurred. The asymmetric states are caused by one sided separation bubbles and can be interpreted as bifurcation phenomena. Thus, under optimal symmetrical test conditions and α = 0°, the side where the bubble is formed first, is unpredictable (Schewe 1986).

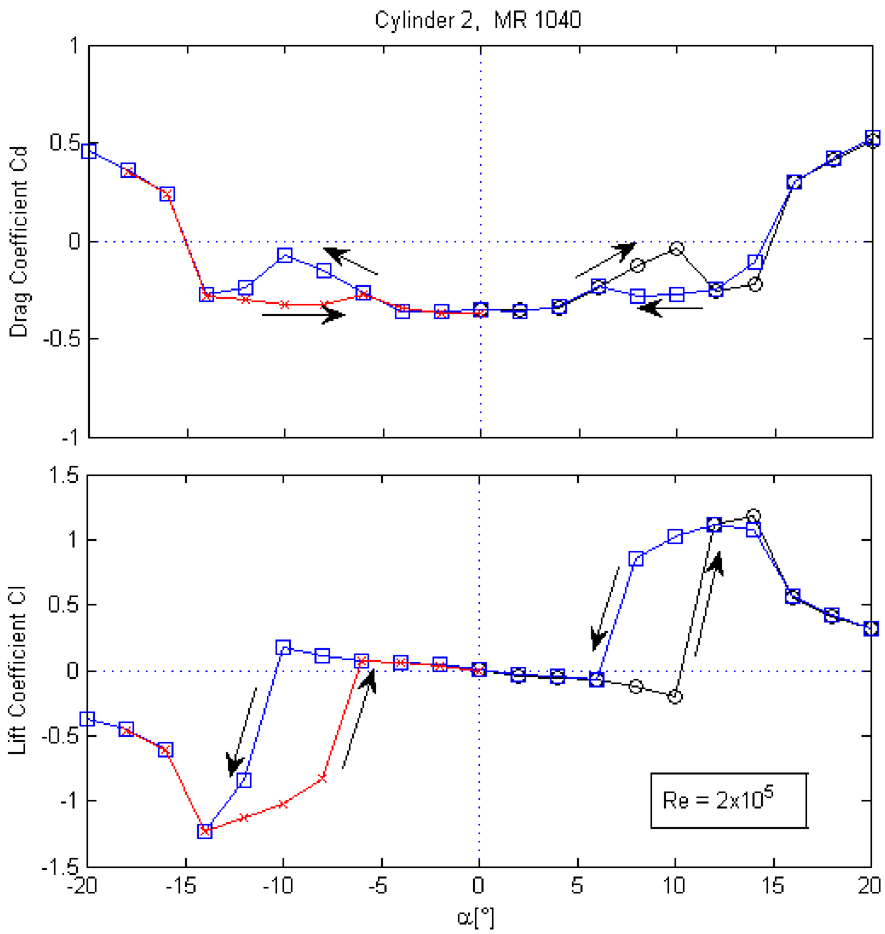


Figure 9: Polar diagram for drag- and lift coefficient on the **second cylinder** for the subcritical Reynolds number-case.

In figure 9: the polar diagram for drag- and lift coefficient on the second cylinder for the subcritical Re No-case is shown. The arrows indicate the direction of the angle variation, thus the strong hysteresis effects are obvious. The sudden increase of the lift, here at ± 10°, is responsible for the propensity to selfexcited oscillations of the downwind cylinder. The acrosswind forces have the tendency to centre the downstream cylinder.  The point symmetry of the curves reflects the good test conditions, even in the case of relatively small forces at the smallest Reynolds number measured.

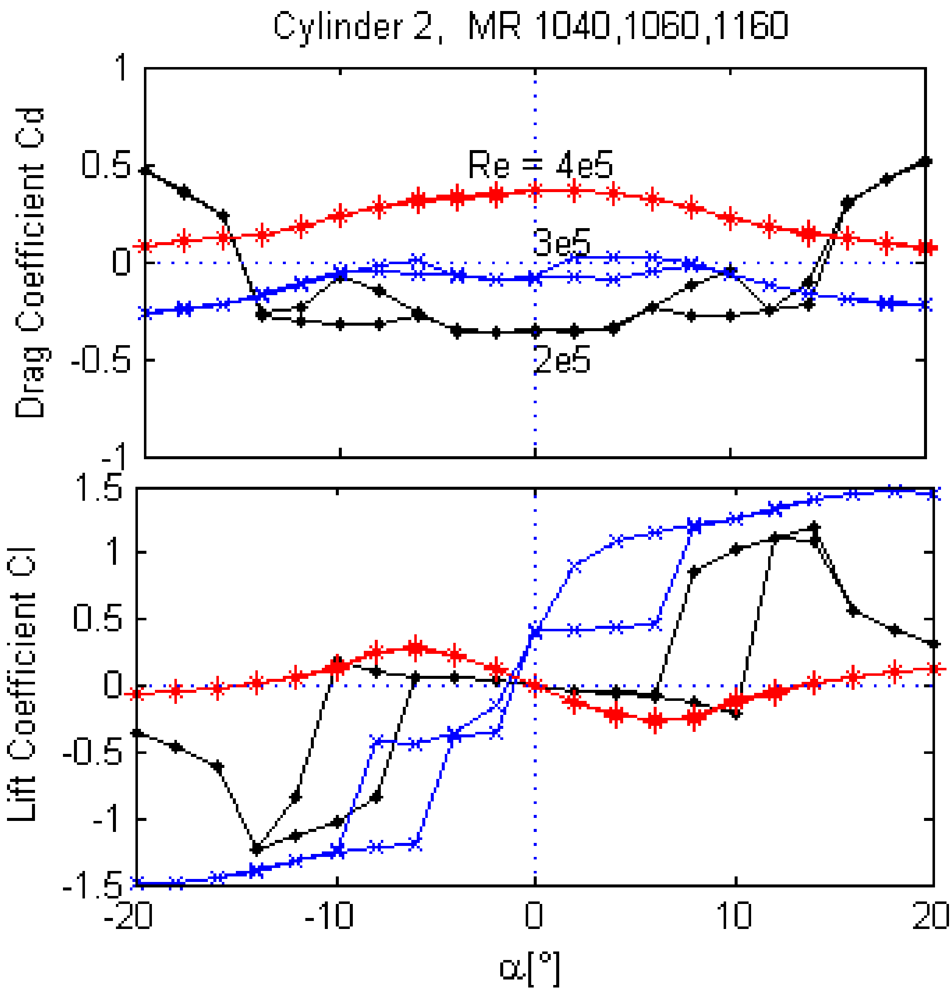


Figure 10: Polar diagram for the drag- and lift coefficient on the **second cylinde**r in and near the critical Reynolds number range. The subcritical case corresponds to figure 9.

The transition from sub- to supercritical Reynolds numbers reflected in the polar diagram for the drag- and lift coefficient on the second cylinder is illustrated in figure 10. The most obvious change to supercritical Re is the fact, that there is no longer the sudden increase in the lift. Concerning the drag coefficient the sign changes not only for α = 0° but also for a larger range of angles around. For Re = 3e5 and α = 0° there is steady lift.

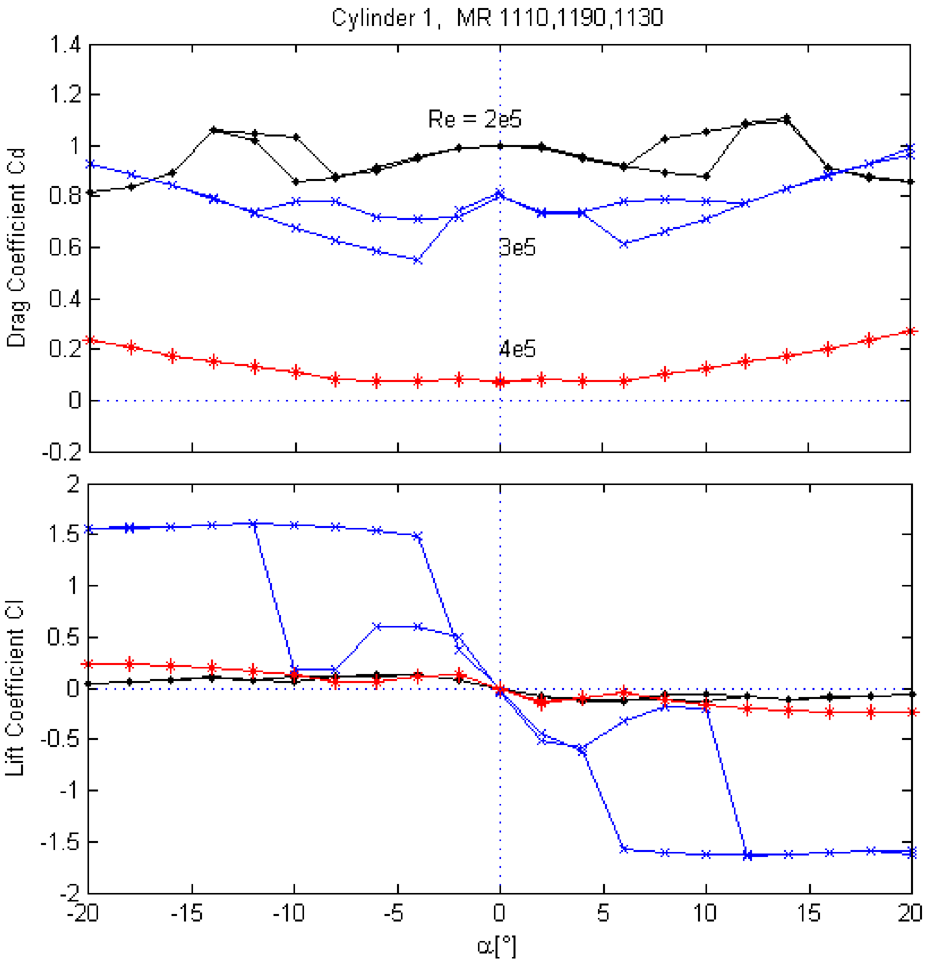


Figure 11: Polar diagram for the drag- and lift coefficient on the **first cylinder** in and near the critical Reynolds number range.

Figure 11 displays the corresponding polar diagram for the drag- and lift coefficient on the first cylinder**.** In particular directly in the critical regime at Re = 3e5 there are strong lift forces with increasing angle, which are coupled with hysteresis and the slopes for both cylinder positions are opposite each other.

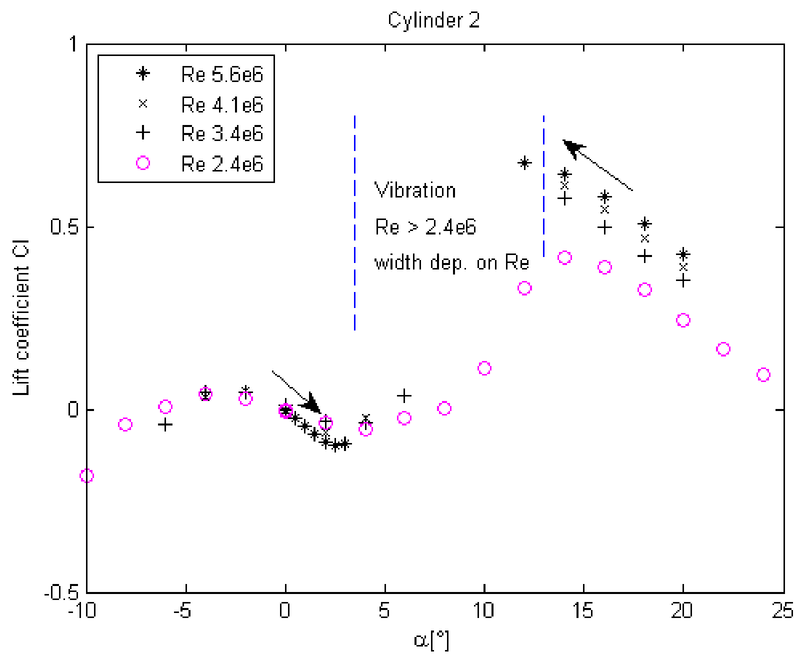


Figure 12: Polar diagram for lift coefficient on the second cylinder for the very high Reynolds number-case

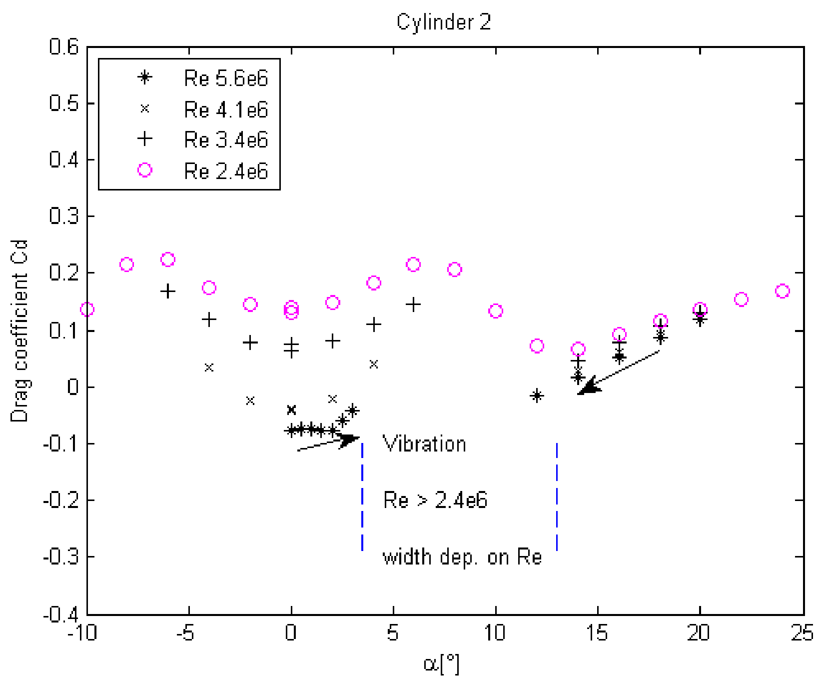


Figure 13: Polar diagram for the drag coefficient on the **second cylinder** for the very high Reynolds number-case

The figures 12 and 13 show the behaviour of the lift- and drag coefficient depending on α for the Re No approaching the desired value of Re = $6 \cdot 10^6$ (in the transcritical range). At Re = 2.4e6 there was the last possibility to take a full polar diagram for the entire range of α. Beginning at Re = 3.4e6, there was a range of angles where violent vibrations in lift direction (87.3Hz) occurred. The arrows indicate how we approached the vibration range. Although we have no measurement in the unstable region, we can conclude from the rest of the curve that with increasing α there must be a drastic increase in the lift force. This behaviour seems to be similar as in the subcritical case displayed in the figure 9. The vibrations occurred also at corresponding negative angles, but in order to preserve the test setup, we decided to take no corresponding measuring point. Obviously there was a risk for damage.

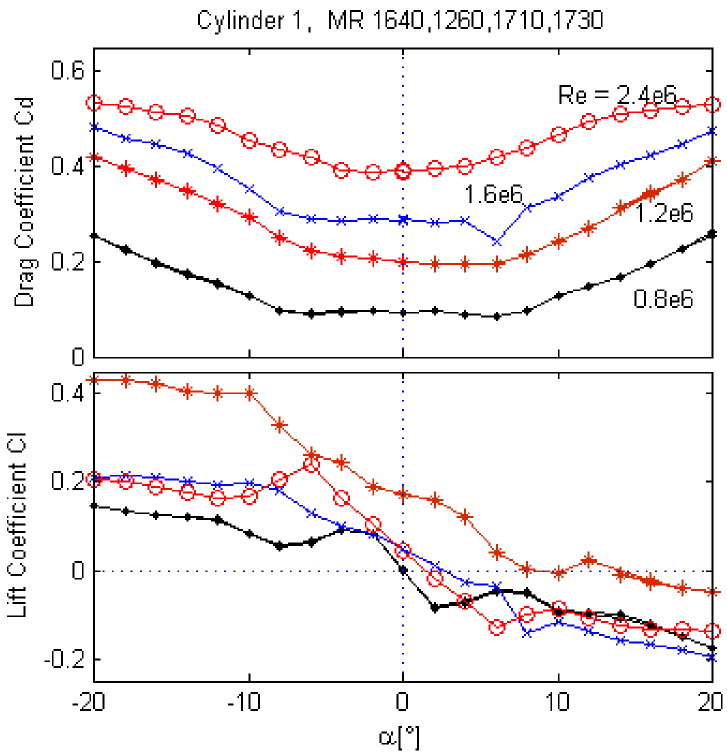


Figure 14: Polar diagram for the drag- and lift coefficient on the **first cylinder** for the Reynolds number approaching the transcritical range.

In figure 14 we see the polar diagram for the drag- and lift coefficient concerning the **first cylinder,** when the Reynolds number is approaching the transcritical range. For Re = 1.2e6 there is still a steady asymmetry in the lift.

As mentioned in the context of figure 7, we were not able to take measurement for Re > 2.4e6. For $\alpha = 0°$ and p = 80 bar the violent vibrations in lift direction ( 87Hz ) began at a wind speed of about 14m/s i.e. at nearly the same Re No at which we already had measured (60bar). We had the impression that in particular around $\alpha = 0°$ the situation was prone to vibrations, thus with $\alpha = 20°$ we tried to cross the vibration range (flow speed sweep) but even at about 28 m/s, the violent vibration did not cease and we had to break off. It seemed that vortex resonance phenomena as well as selfexcited oscillation could have been the reason for the vibrations. Selfexcited oscillations could be associated with the negative slope in the characteristic of the lift, which (the slope) increases with increasing Re. At the highest Re measured for this case, Re = 2.4e6, the lift is nearly linear in the range $\alpha = \pm 6°$ with negative slope.

The derivative of the lift for this case is $\partial Cl / \partial \alpha = -1.7$. Applying the den Hartog criterion yields:

$$\partial Cl / \partial \alpha \ + \ Cd = -1.7 \ + 0.4 \ < \ 0$$ indicating instability.

Unfortunately it is very difficult to obtain the vortex shedding frequency, when using strain gauge balances. By appropriate small variations of the flow speed, we tried to find a significant (Strouhal) peak, but so close to the eigenfrequency of the force measuring system, in the unsteady signal of the balance, we could not find an indication for a spectral Strouhal peak.

## References

Ruscheweyh, H. 1983 Aeroelastic interferences effects between slender structures. J. Wind Eng. and Ind. Aerodynamics, 14 p 129-140

Schewe, G. 1983 On the force fluctuations acting on a circular cylinder in crossflow from subcritical to transcritical Reynolds numbers. J. Fluid Mech. 133, p. 265

Schewe, G. 1986 Sensitivity of transition phenomena to small perturbations in flow round a circular cylinder. J. Fluid Mech. 172, p. 33

Schewe, G. 2001 Reynolds-number effects in flow around more-or-less bluff bodies. J. Wind Eng. Ind. Aerodyn. 89, p. 1267

Simiu, E., Scanlan, R. H. 1996 Wind Effects on Structures. John Wiley & Sons 3. Ed, p. 240

## 1.1 List of all Tests

| Polar Number | Name of Run | Name of Polar | Number of Points |
|---|---|---|---|
| | **Single Cylinder Roughness 30 um** | | |
| 310 | Pk=5bar | U=10-32m/s_kalibriert | 107 |
| 360 | Pk=20bar | U=10-32m/s | 13 |
| 440 | Pk=35bar | U=10-32m/s_kalibriert | 16 |
| | | | |
| 1040 | Pk=5bar | Re=0.2_Mio | 51 |
| 1060 | Pk=5bar | Re=0.4_Mio | 51 |
| 1160 | Pk=5bar | Re=0.3_Mio | 51 |
| 1330 | Pk=20bar | Re=0.4_Mio | 51 |
| 1350 | Pk=20bar | Re=0.8_Mio | 28 |
| 1370 | Pk=20bar | Re_0.4-1.6_alpha0 | 9 |
| 1390 | Pk=20bar | Re=1.2_Mio | 28 |
| 1410 | Pk=20bar | Re=1.6_Mio | 28 |
| 1430 | Pk=20bar | Re_0.4-1.6_alpha0 | 11 |
| 1510 | Pk=40bar | Re_0.5-3.2_alpha0 | 10 |
| 1530 | Pk=40bar | Re_0.5-3.2_alpha2 | 10 |
| 1550 | Pk=40bar | Re=0.8_Mio | 51 |
| 1570 | Pk=40bar | Re=1.6_Mio | 27 |
| 1590 | Pk=40bar | Re=2.4_Mio | 27 |
| 1780 | Pk=60bar | Re_1.0-4.4_alpha0 | 11 |
| 1800 | Pk=60bar | Re=1.6Mio | 27 |
| 1820 | Pk=60bar | Re=3.2_Mio | 7 |
| 1840 | Pk=60bar | Re=3.2_Mio | 5 |
| 1860 | Pk=60bar | Re=3.2_Mio | 5 |
| 1880 | Pk=60bar | Re=4.0_Mio | 4 |
| 1900 | Pk=60bar | Re=4.0_Mio | 3 |
| 1920 | Pk=60bar | Re=4.0_Mio | 5 |
| 1950 | Pk=80bar | Re_0.8-6_alpha0 | 10 |
| 1970 | Pk=80bar | Re=5.68_Mio | 8 |
| 1990 | Pk=80bar | Re=5.68_Mio | 6 |
| 2020 | Pk=5bar | StatischeReihe-110_-60 | 51 |
| | | | |
| 2050 | Pk=5bar_vl | StatischeReihe70_120 | 51 |
| 1090 | Pk=5bar_vl | StatischeReihe70_120 | 51 |
| 1110 | Pk=5bar_vl | Re=0.2_Mio | 51 |
| 1130 | Pk=5bar_vl | Re=0.4_Mio | 51 |
| 1190 | Pk=5bar_vl | Re=0.3_Mio | 51 |
| 1220 | Pk=20bar_vl | Re=0.4_Mio | 51 |
| 1240 | Pk=20bar_vl | Re=0.8_Mio | 27 |
| 1260 | Pk=20bar_vl | Re=1.2_Mio | 30 |
| 1280 | Pk=20bar_vl | Re=1.6_Mio | 12 |
| 1300 | Pk=20bar_vl | Re=1.6_Mio | 27 |
| 1460 | Pk=20bar_vl | Re_0.4-1.6_alpha0 | 11 |
| 1480 | Pk=20bar_vl | Re=1.6_Mio | 4 |
| 1620 | Pk=40bar_vl | Re_0.5-3.2_alpha0 | 8 |
| 1640 | Pk=40bar_vl | Re=0.8_Mio | 51 |
| 1660 | Pk=40bar_vl | Re=1.6_Mio | 27 |
| 1690 | Pk=60bar_vl | Re=1.6_Mio | 11 |
| 1710 | Pk=60bar_vl | Re=1.6_Mio | 28 |
| 1730 | Pk=60bar_vl | Re=2.4_Mio | 27 |
| 1750 | Pk=60bar_vl | Re_1.0-4.4_alpha0 | 7 |

# Appendix

# Polars

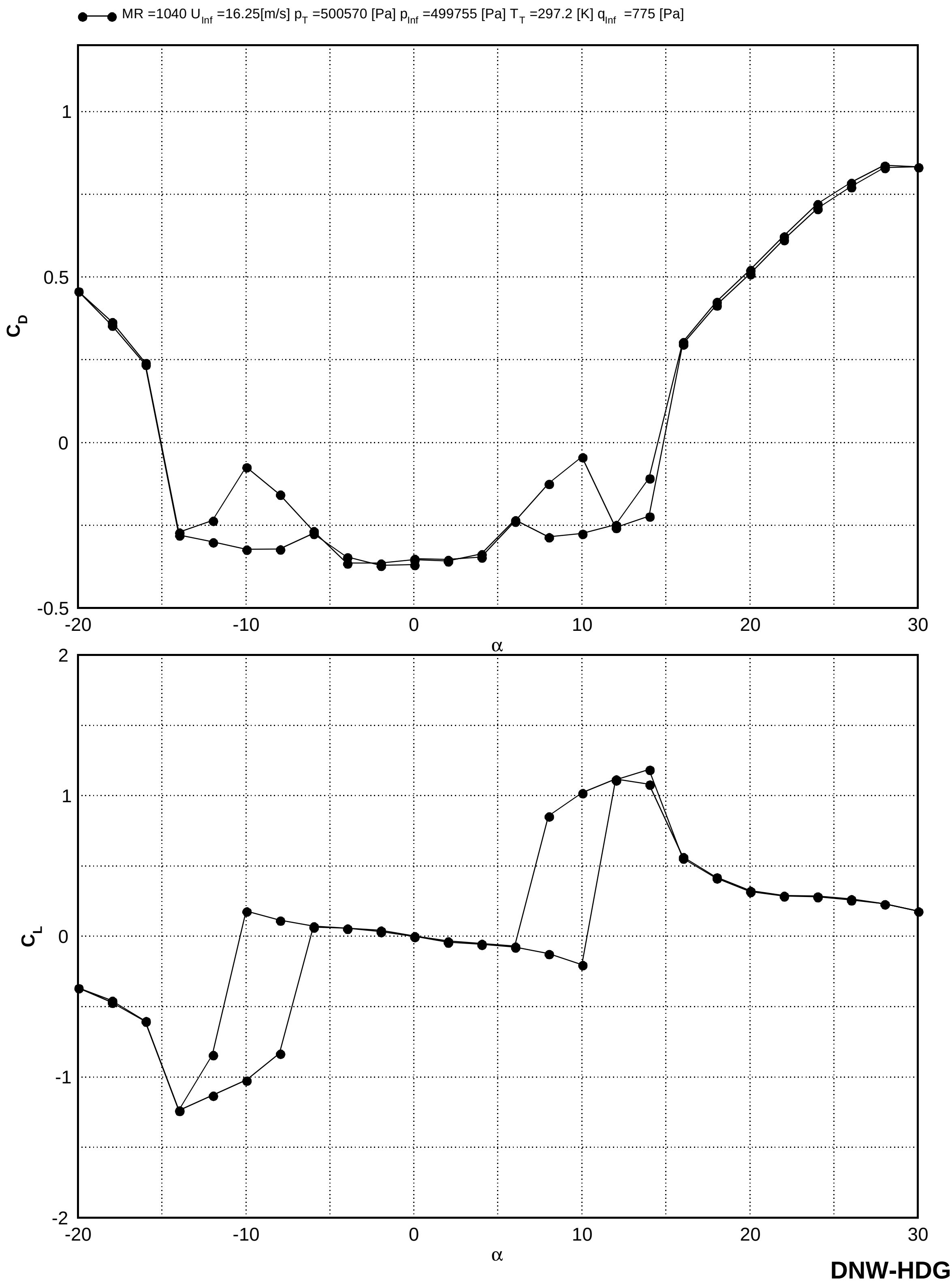


**Figure 1** 2'nd Cylinder Re= 0.199 [Mio] Pk=5bar

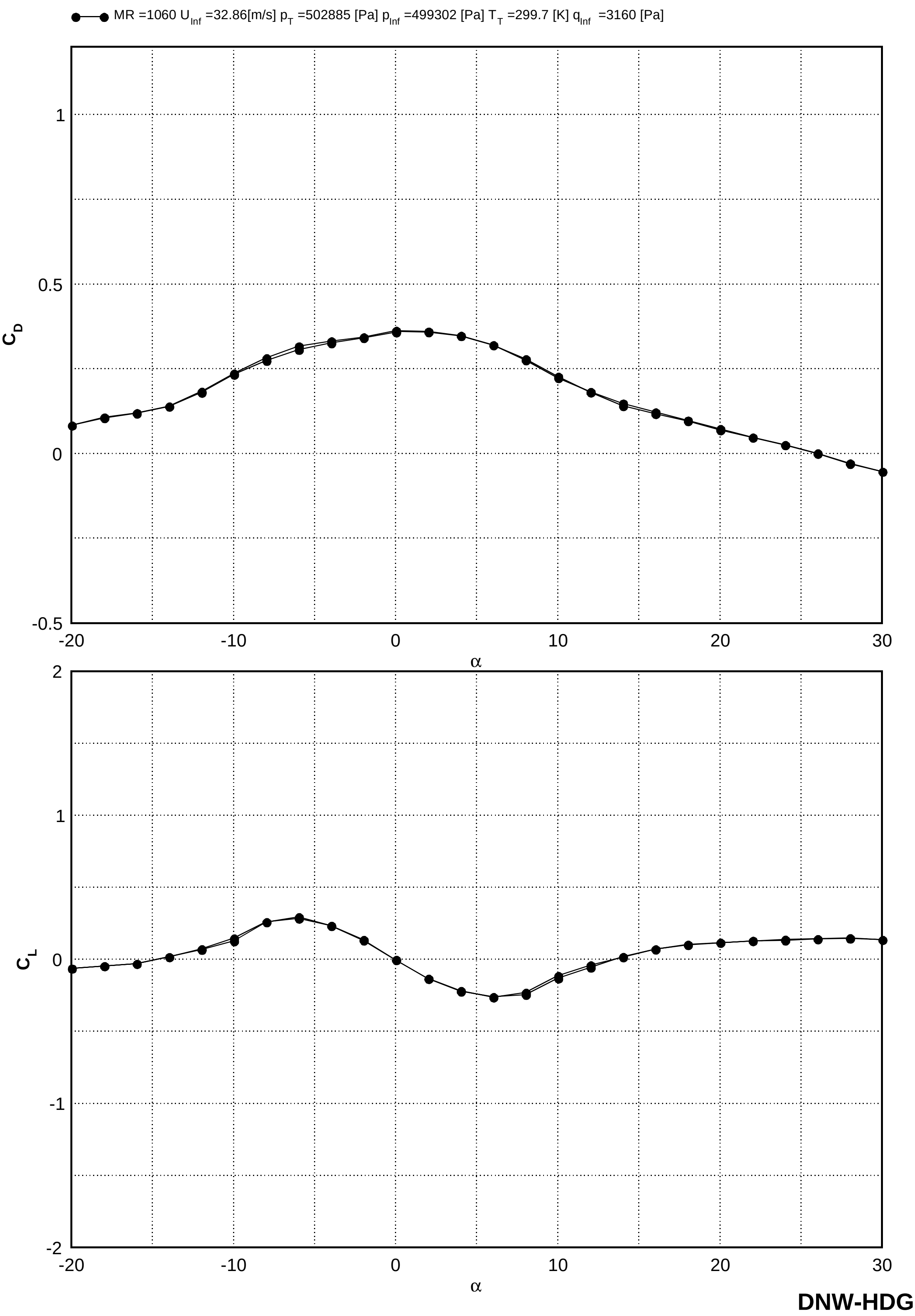


**Figure 2** 2'nd Cylinder Re= 0.399 [Mio] Pk=5bar

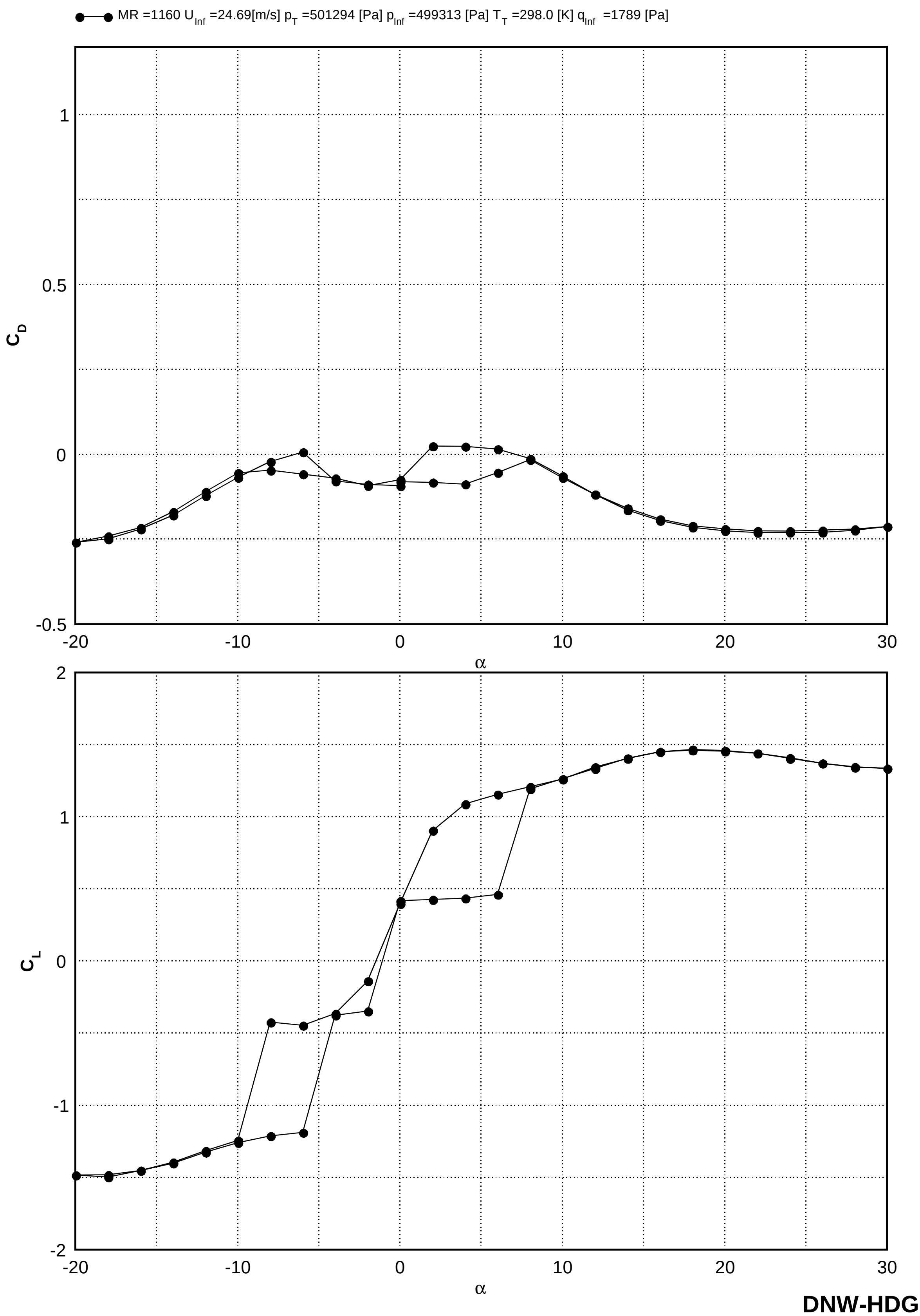


**Figure 3** 2'nd Cylinder Re= 0.302 [Mio] Pk=5bar

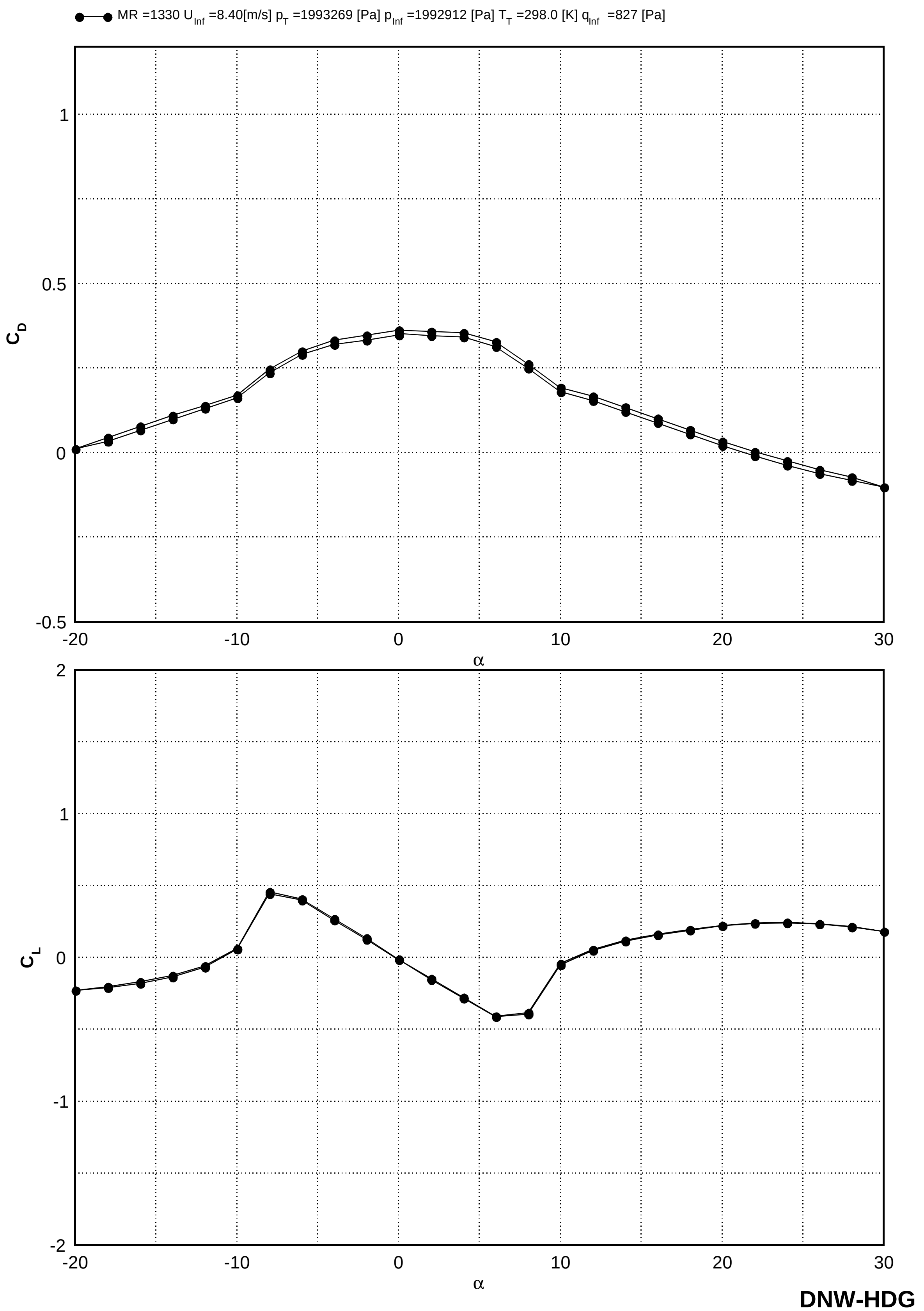


**DNW-HDG**

**Figure 4** 2'nd Cylinder Re= 0.404 [Mio] Pk=20bar

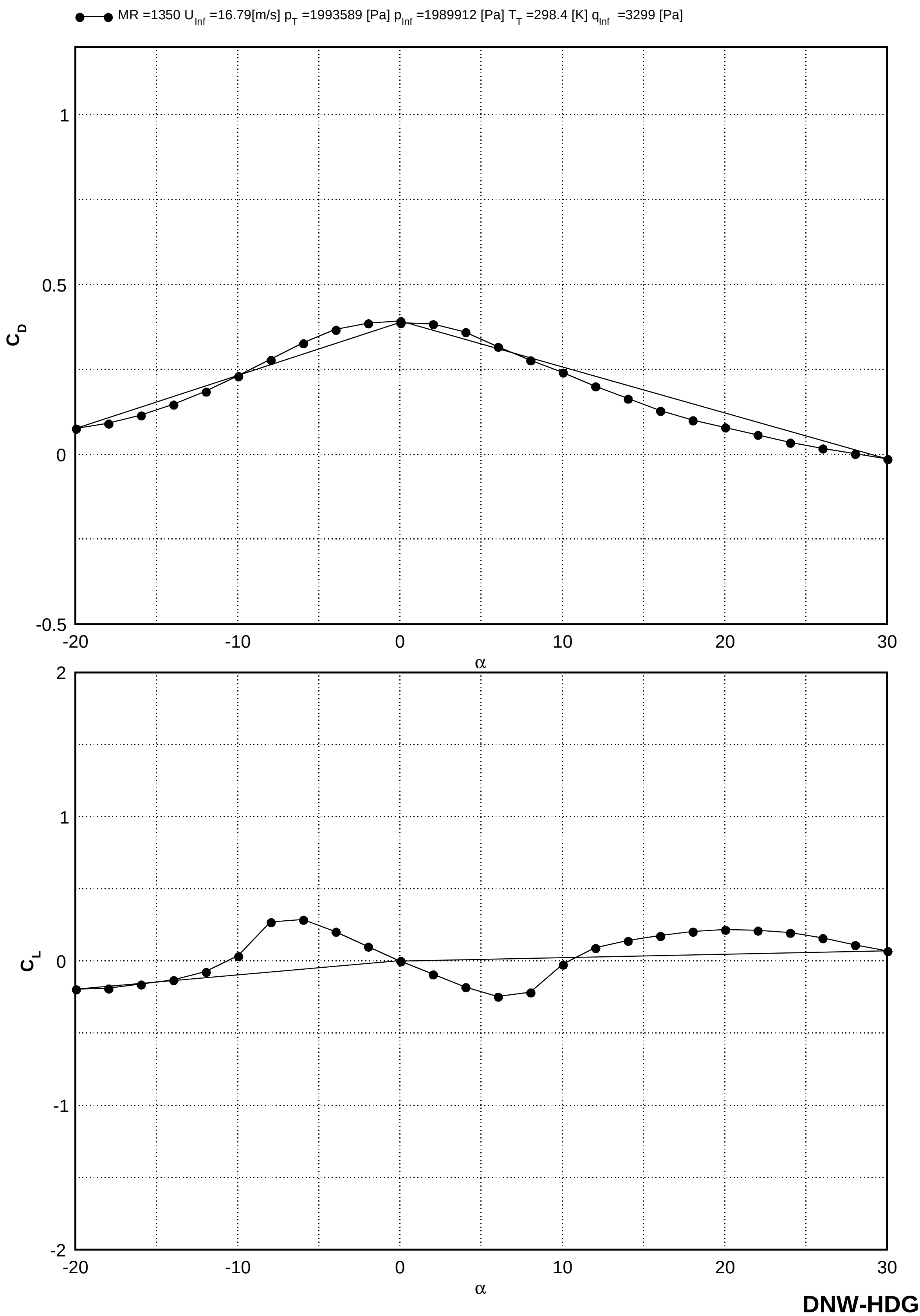


**Figure 5** 2'nd Cylinder Re= 0.806 [Mio] Pk=20bar

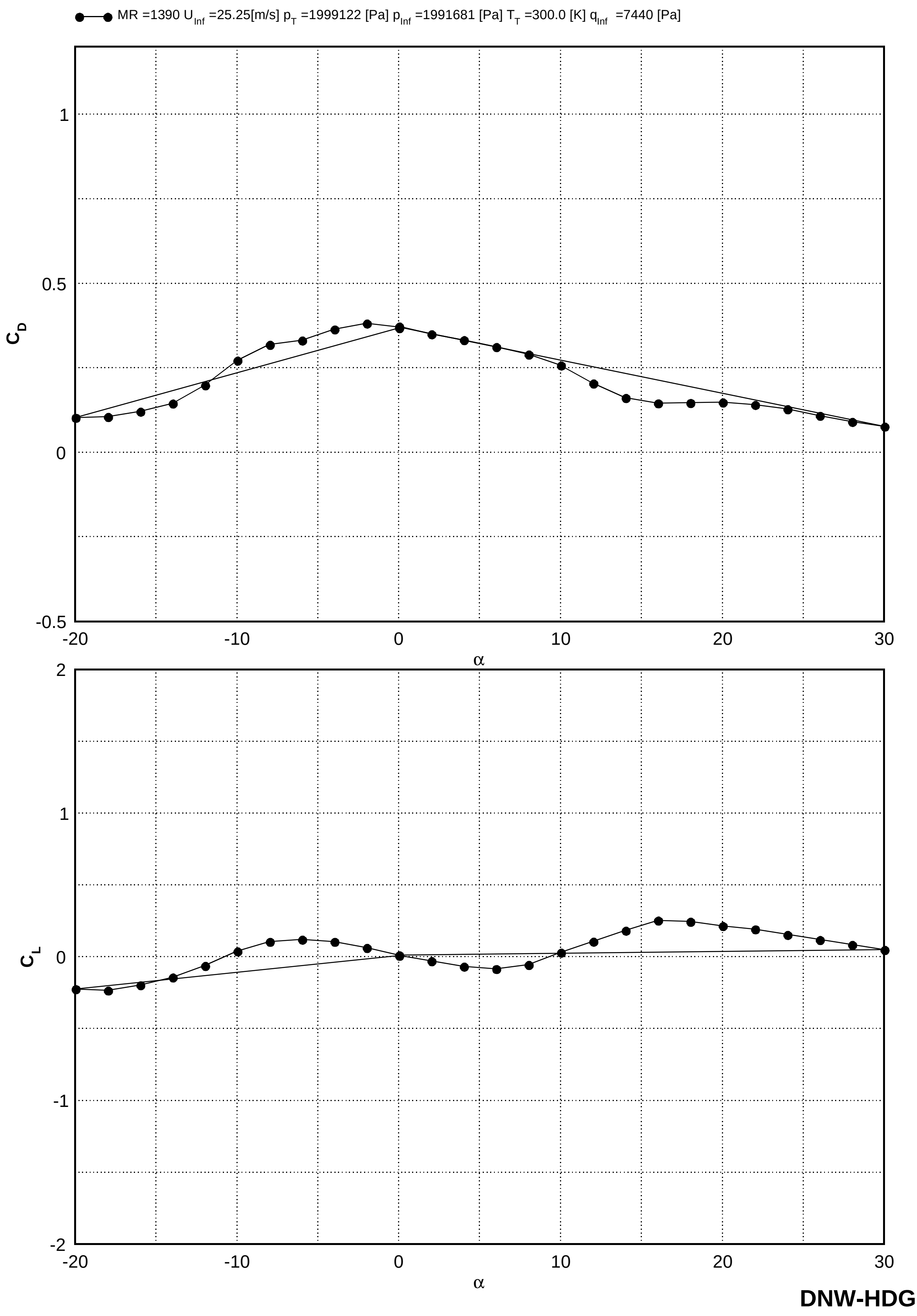


**Figure 6** 2'nd Cylinder Re= 1.204 [Mio] Pk=20bar

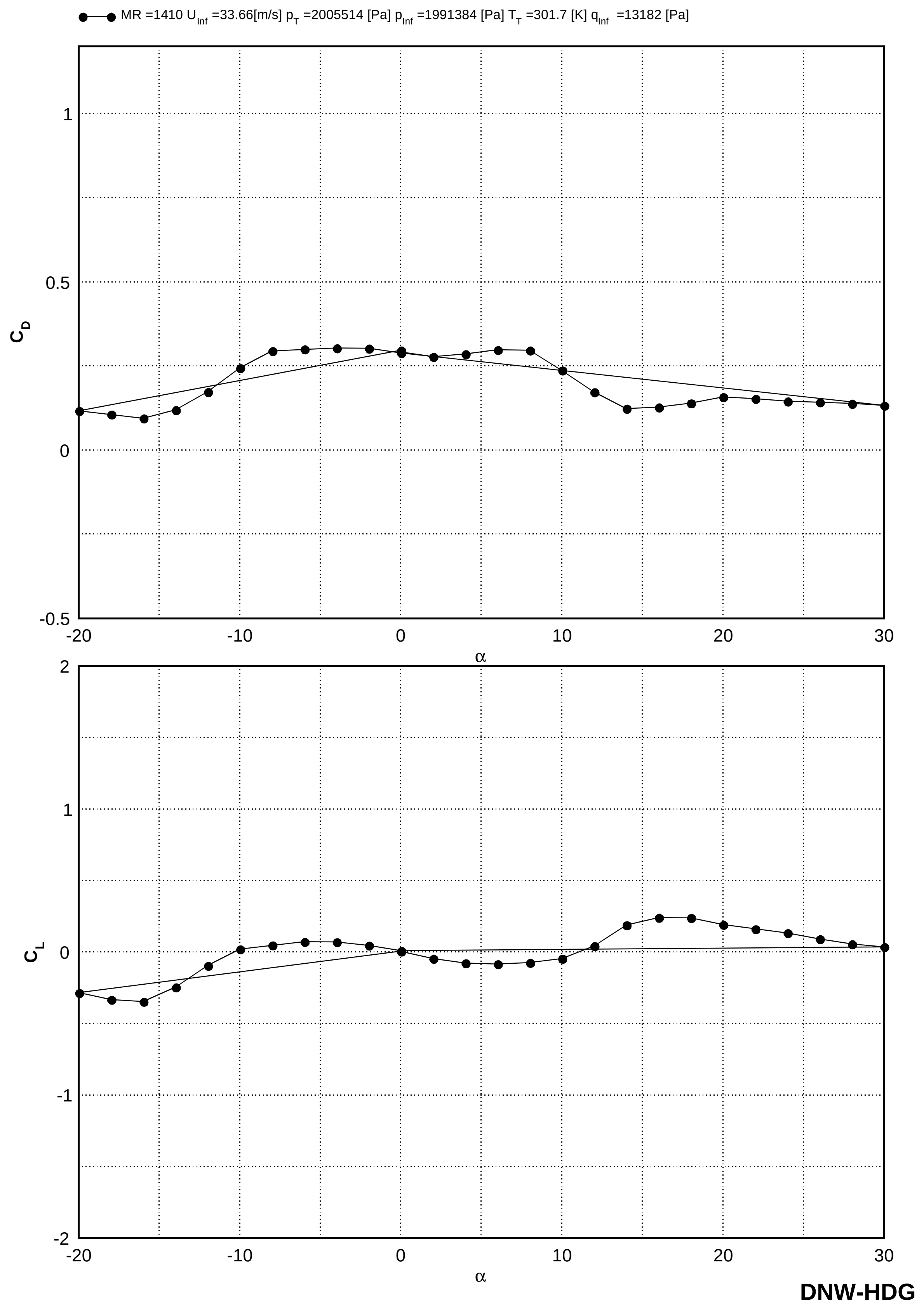


**Figure 7** 2'nd Cylinder Re= 1.594 [Mio] Pk=20bar

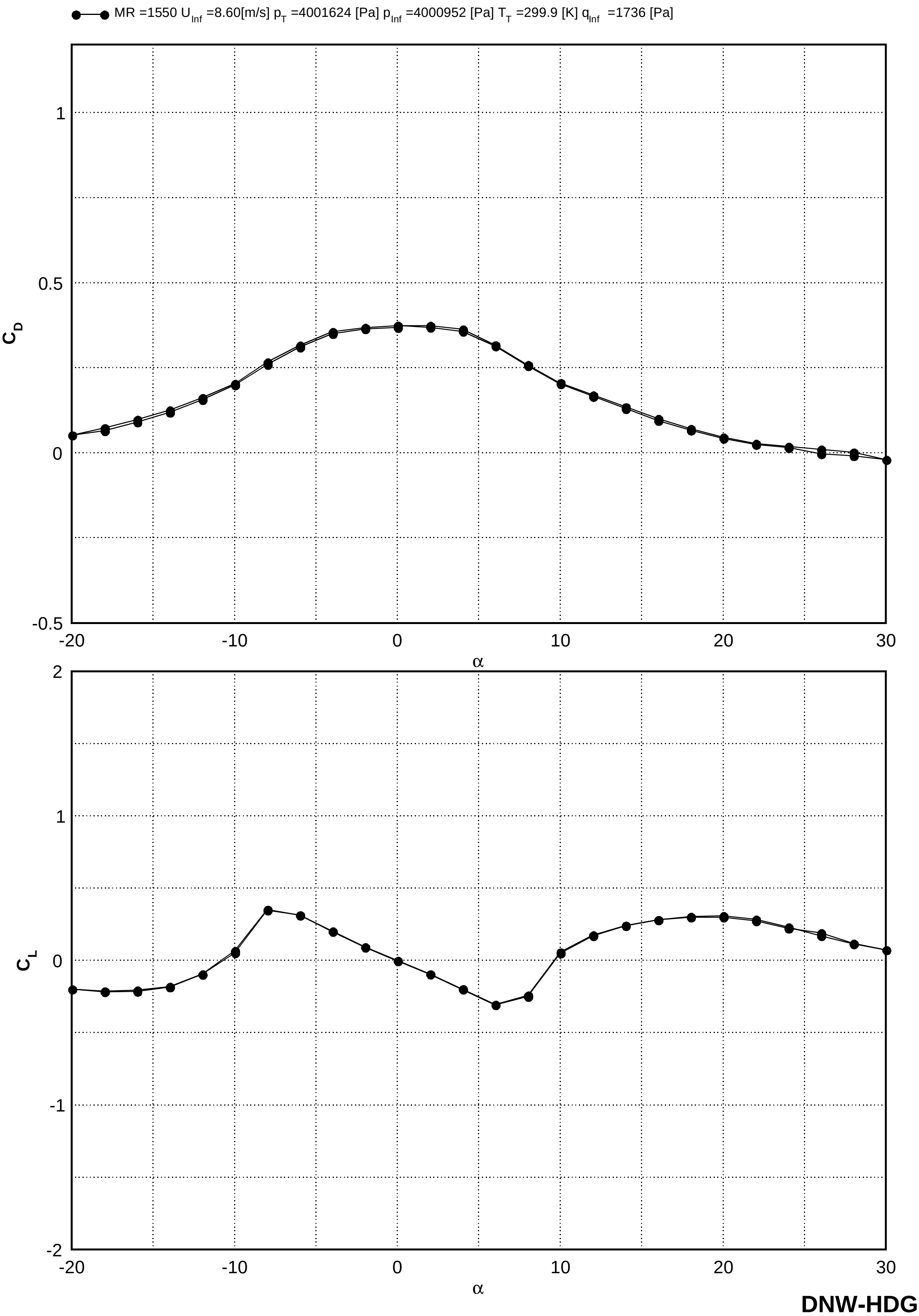


**Figure 8** 2'nd Cylinder Re= 0.808 [Mio] Pk=40bar

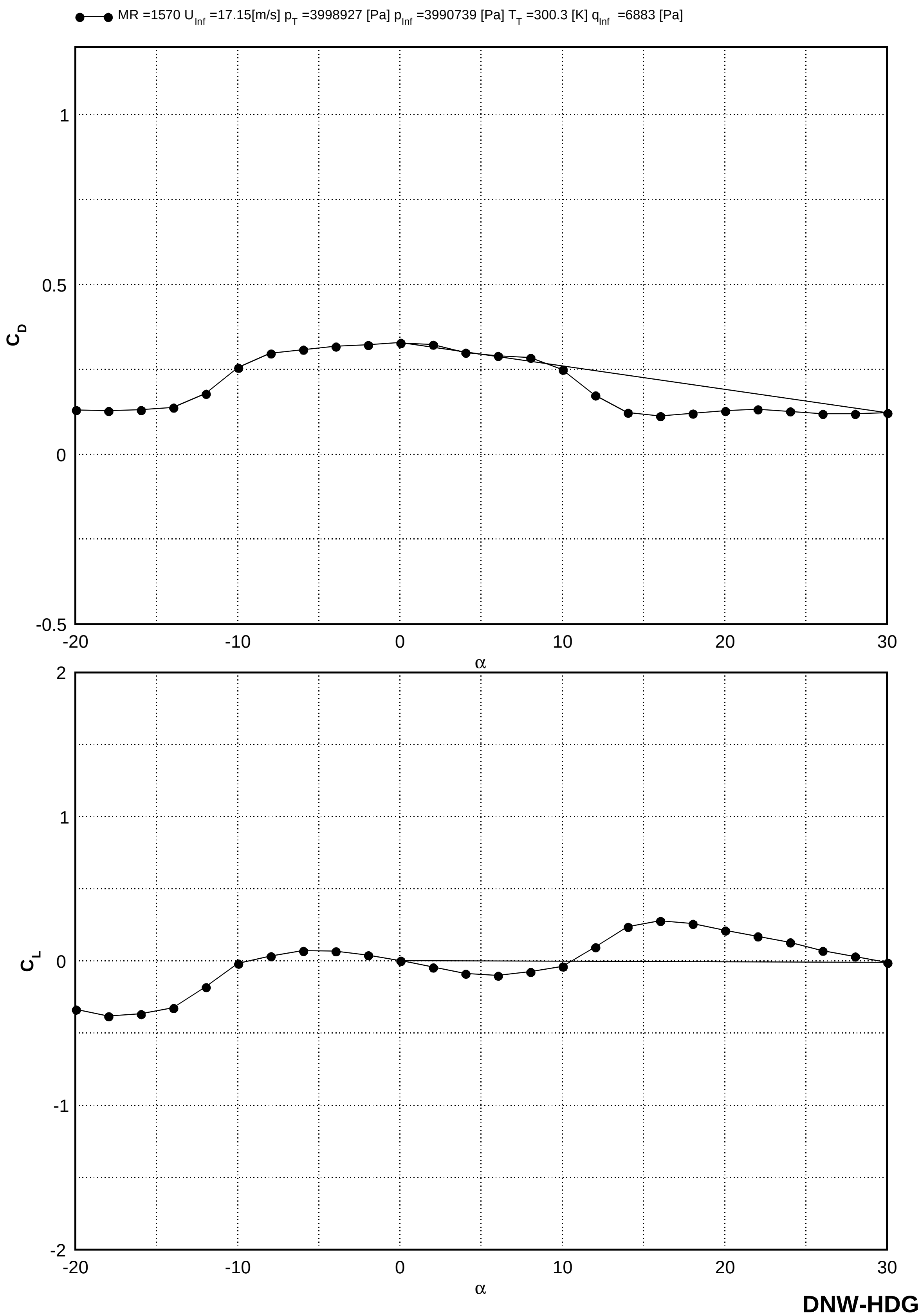


**Figure 9** 2'nd Cylinder Re= 1.606 [Mio] Pk=40bar

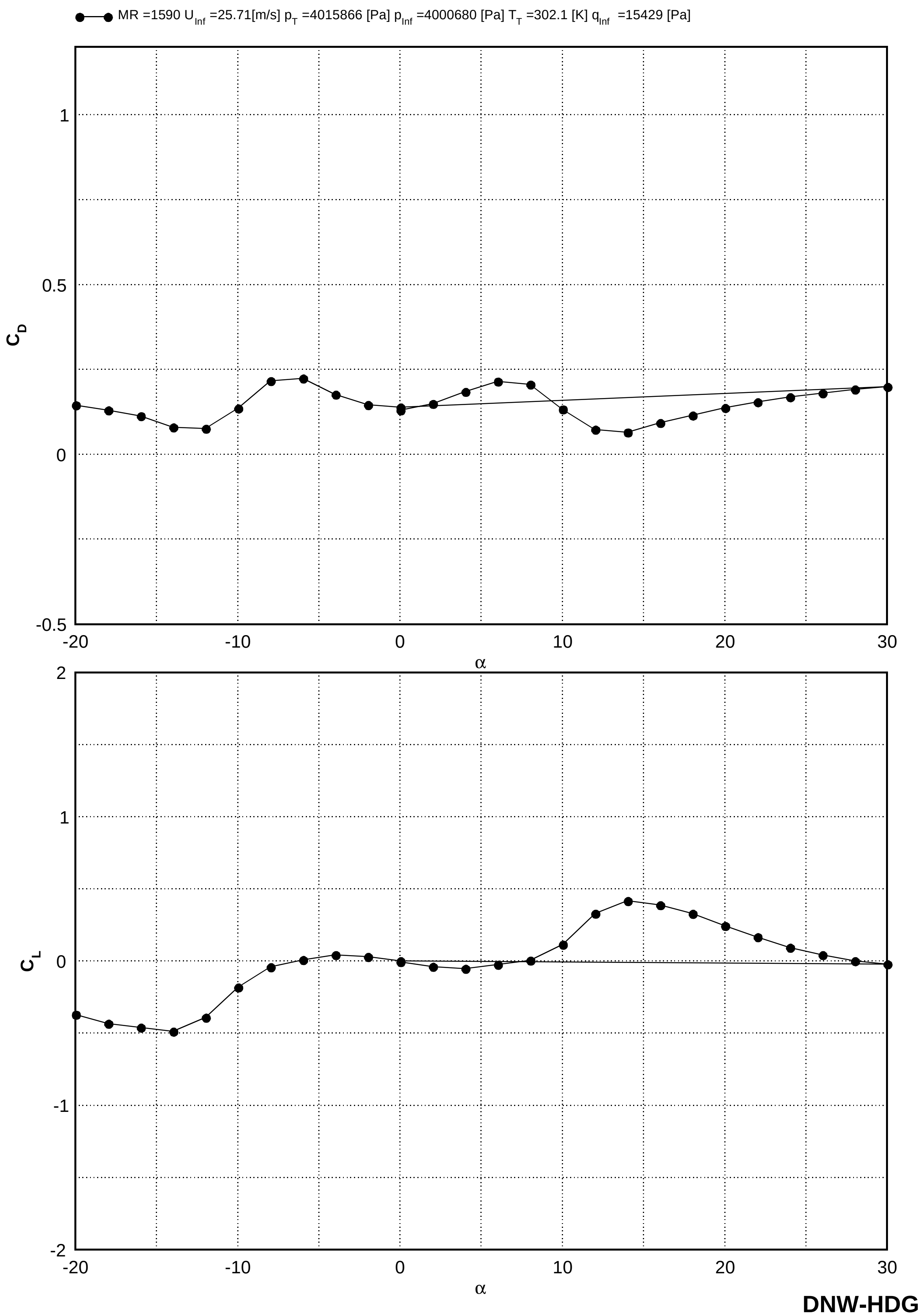


**Figure 10** 2'nd Cylinder Re= 2.392 [Mio] Pk=40bar

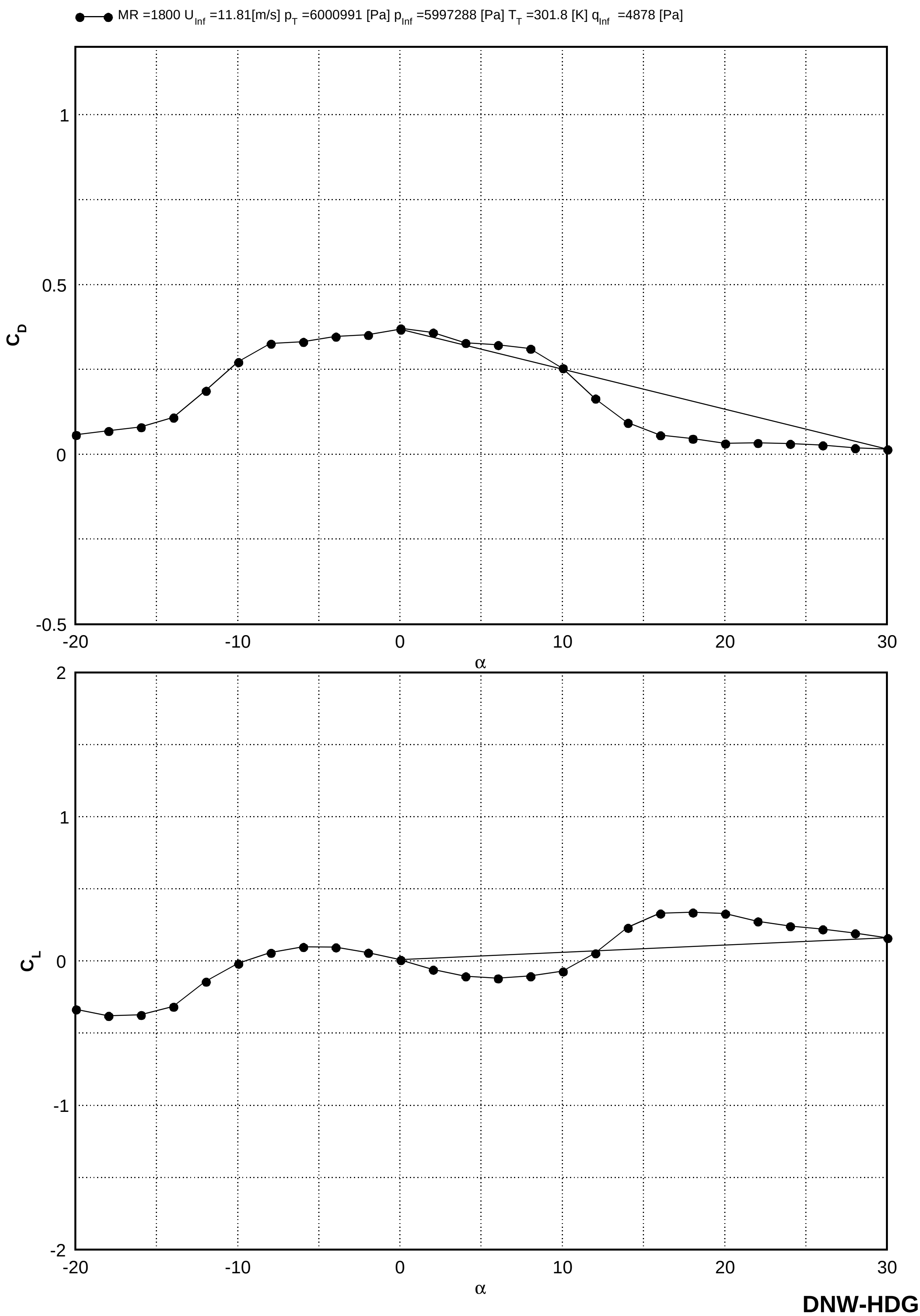


**Figure 11** 2'nd Cylinder Re= 1.612 [Mio] Pk=60bar

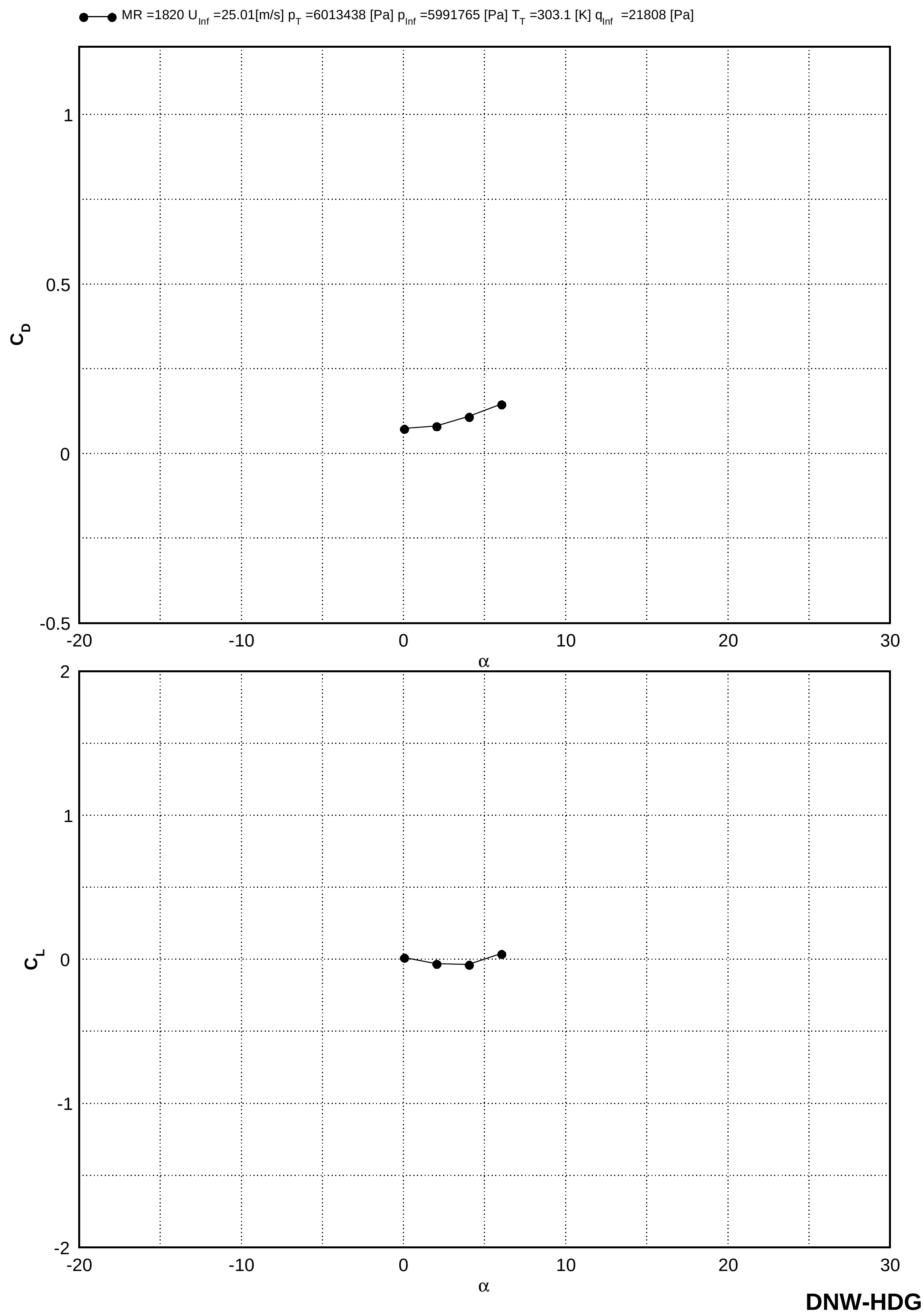


**Figure 12** 2'nd Cylinder Re= 3.394 [Mio] Pk=60bar

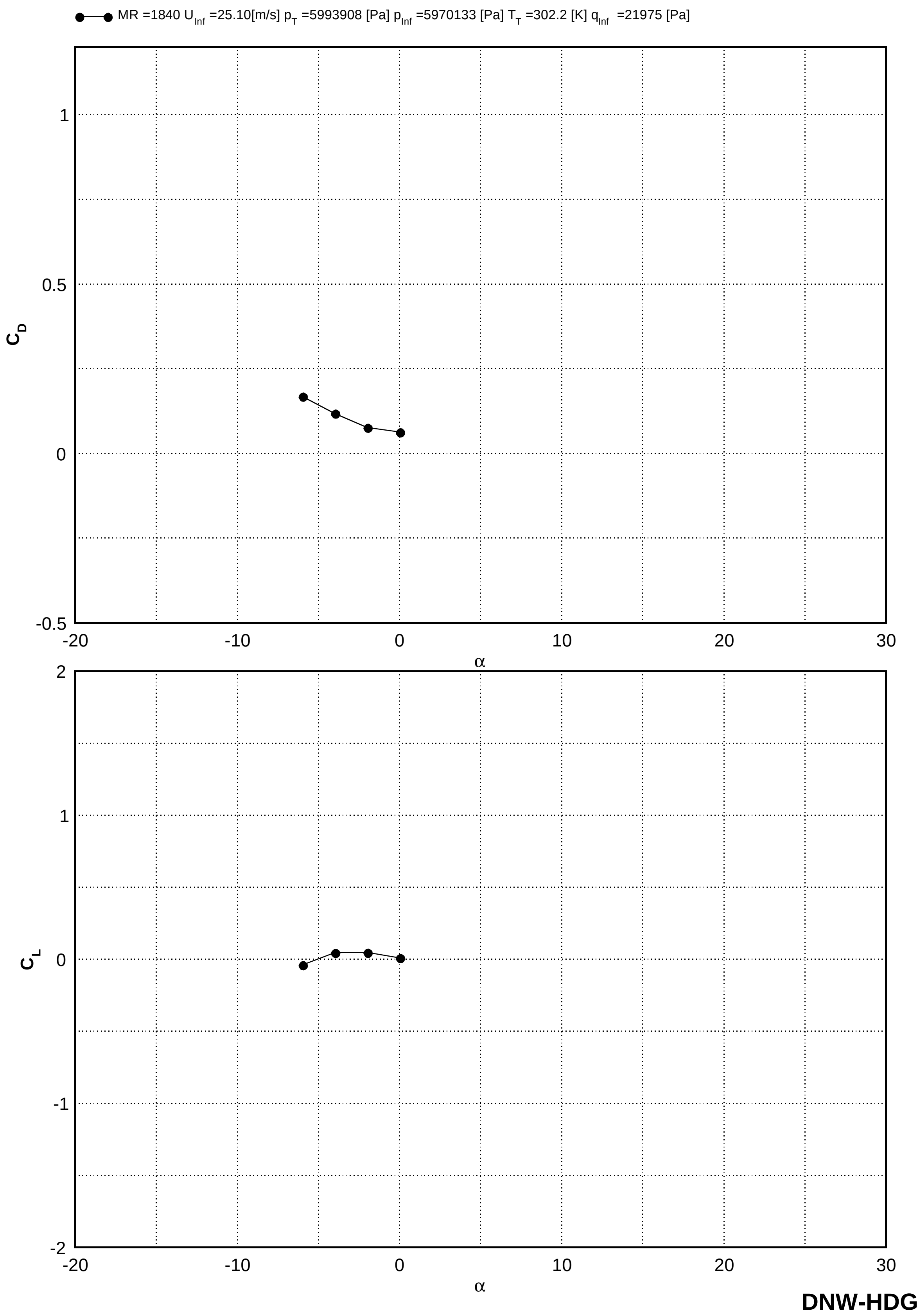


**Figure 13** 2'nd Cylinder Re= 3.415 [Mio] Pk=60bar

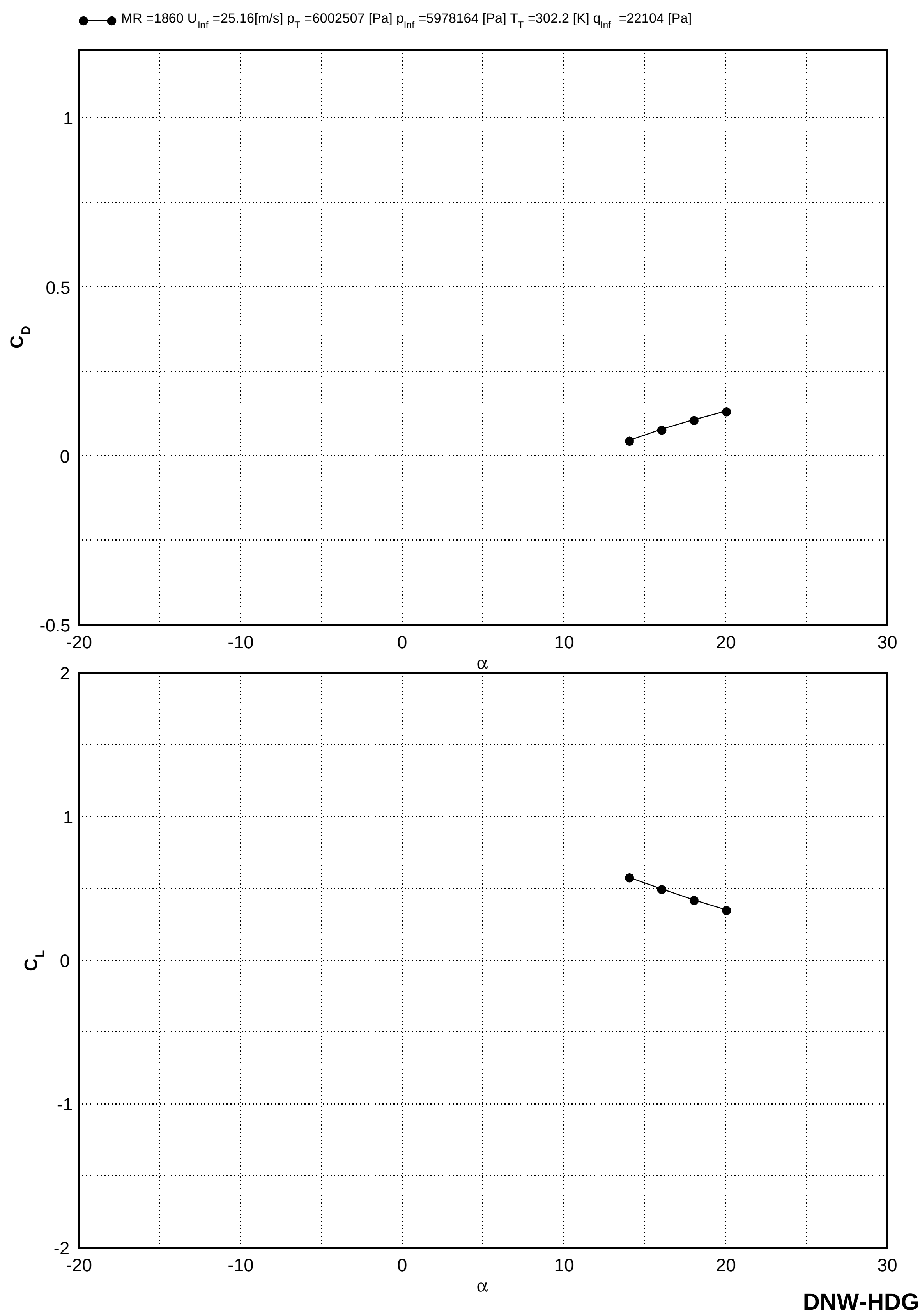


**Figure 14** 2'nd Cylinder Re= 3.427 [Mio] Pk=60bar

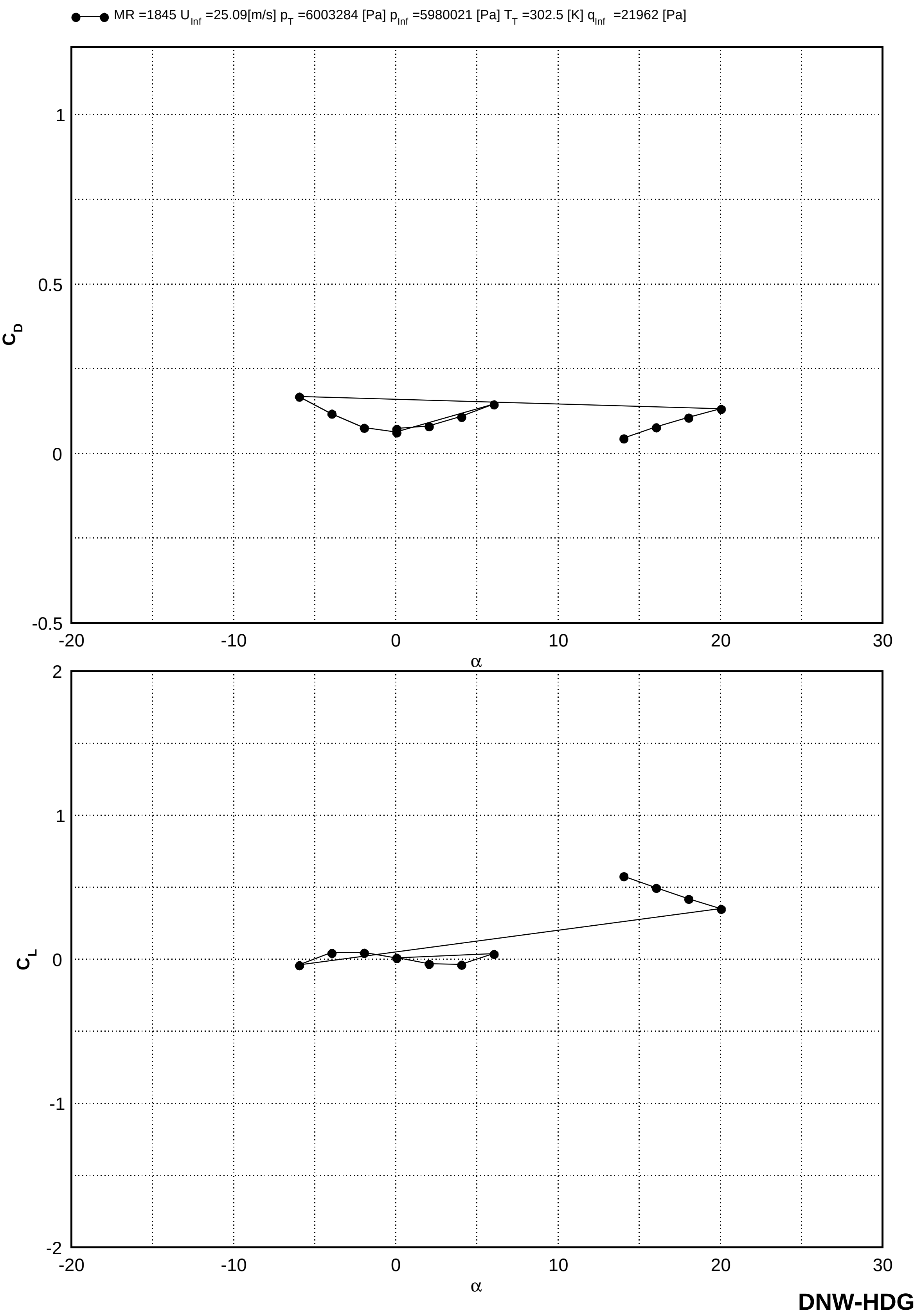


**Figure 15** 2'nd Cylinder Re= 3.412 [Mio] Pk=60bar

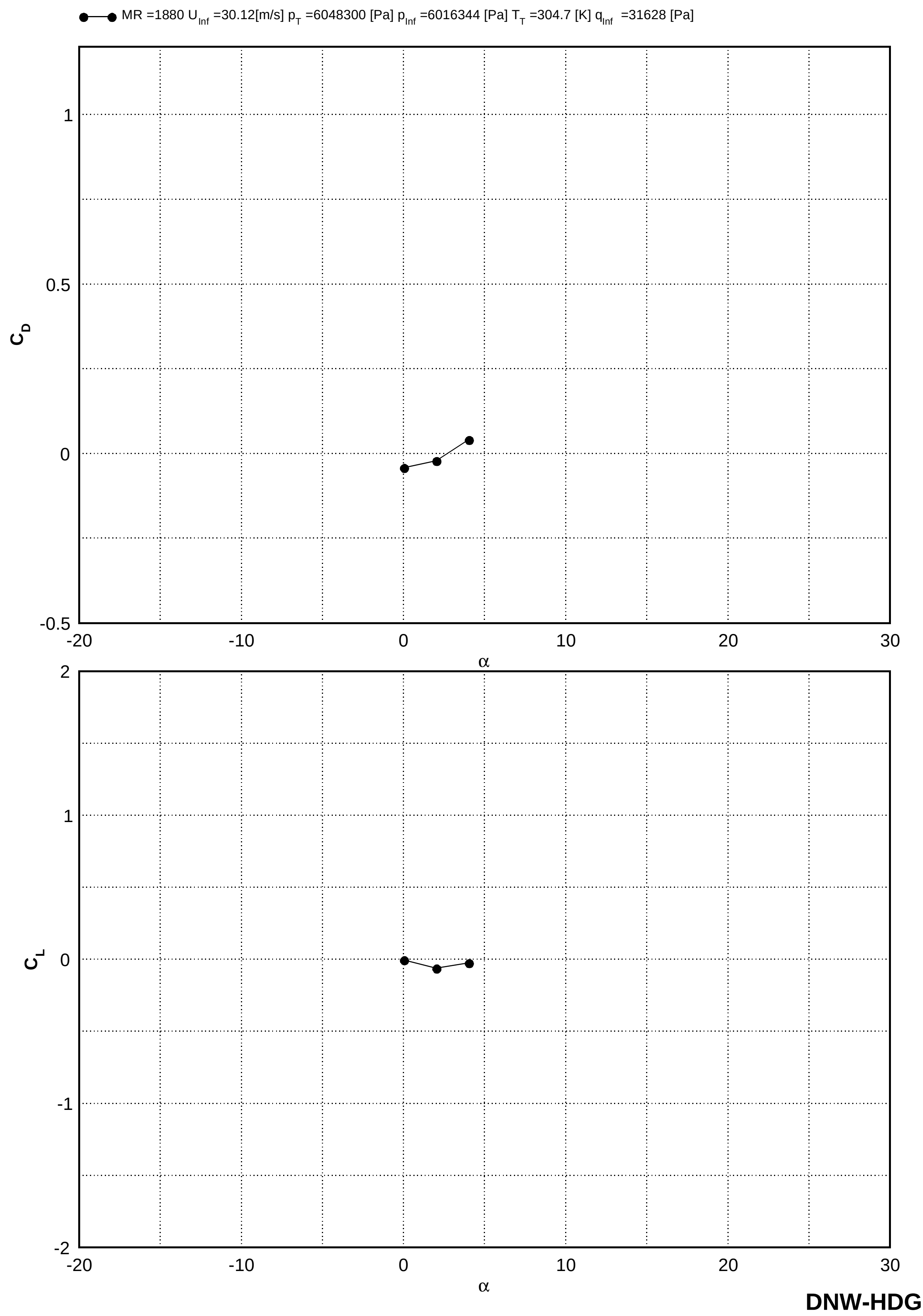


**Figure 16** 2'nd Cylinder Re= 4.072 [Mio] Pk=60bar

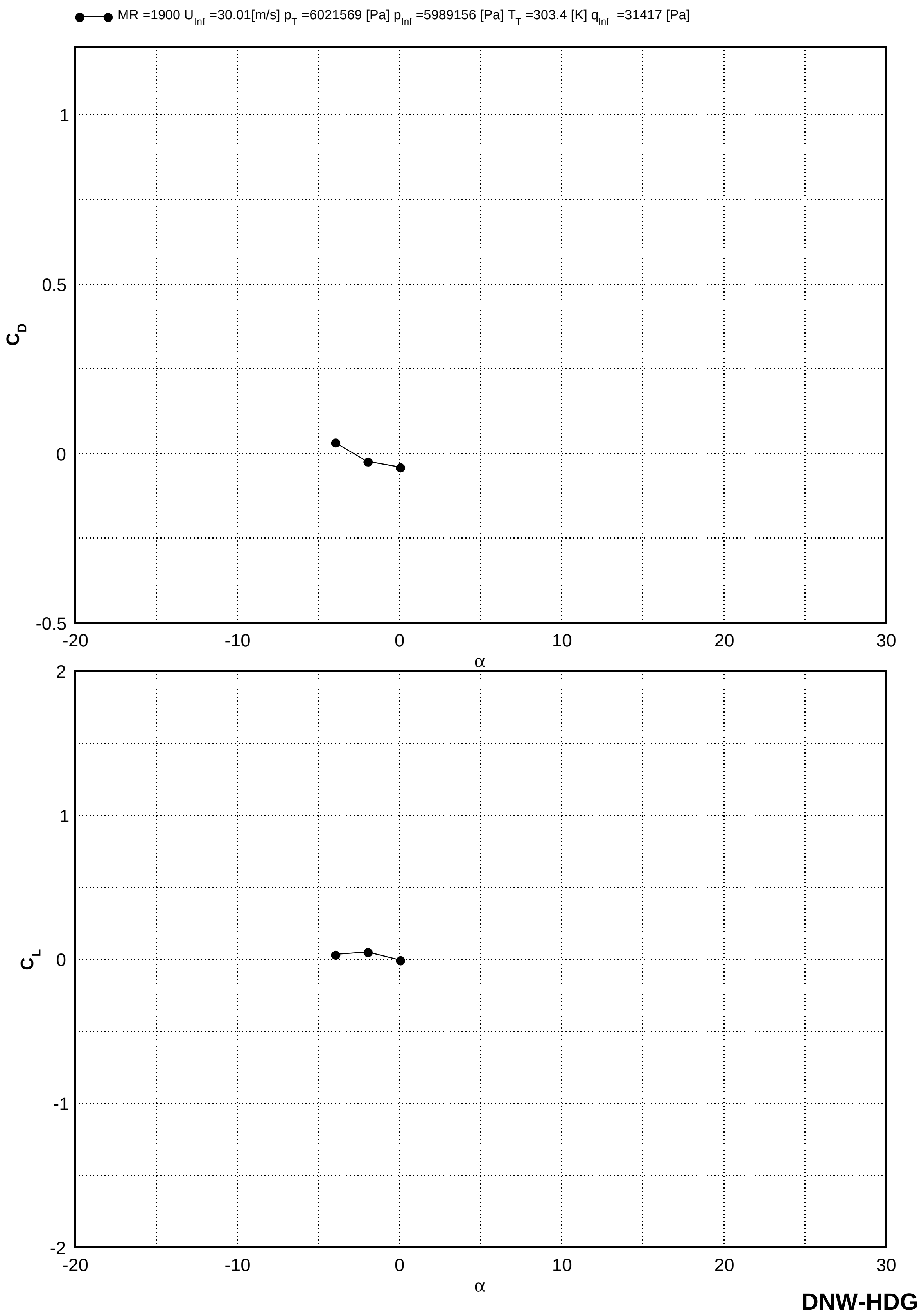


**Figure 17** 2'nd Cylinder Re= 4.071 [Mio] Pk=60bar

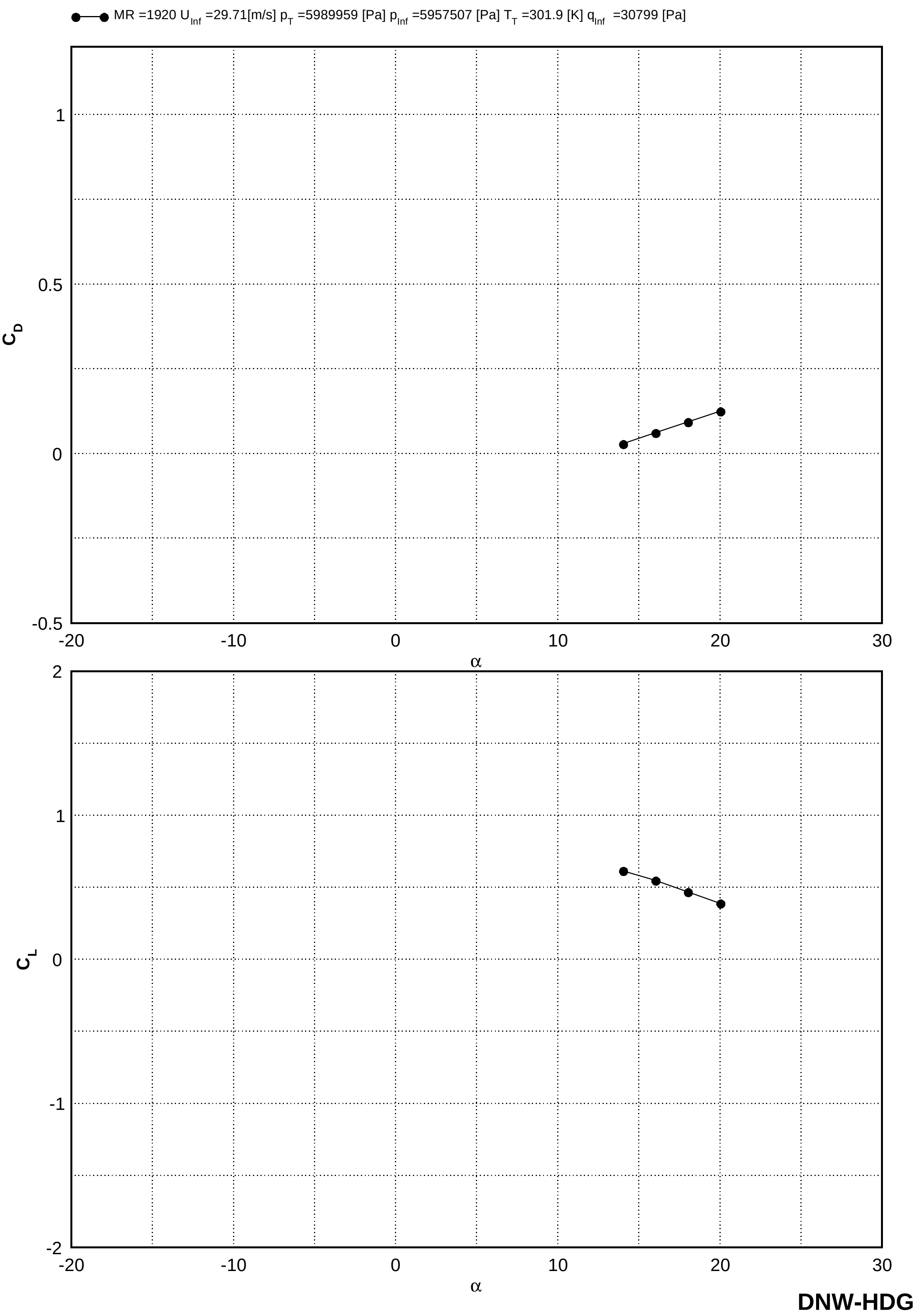


**Figure 18** 2'nd Cylinder Re= 4.046 [Mio] Pk=60bar

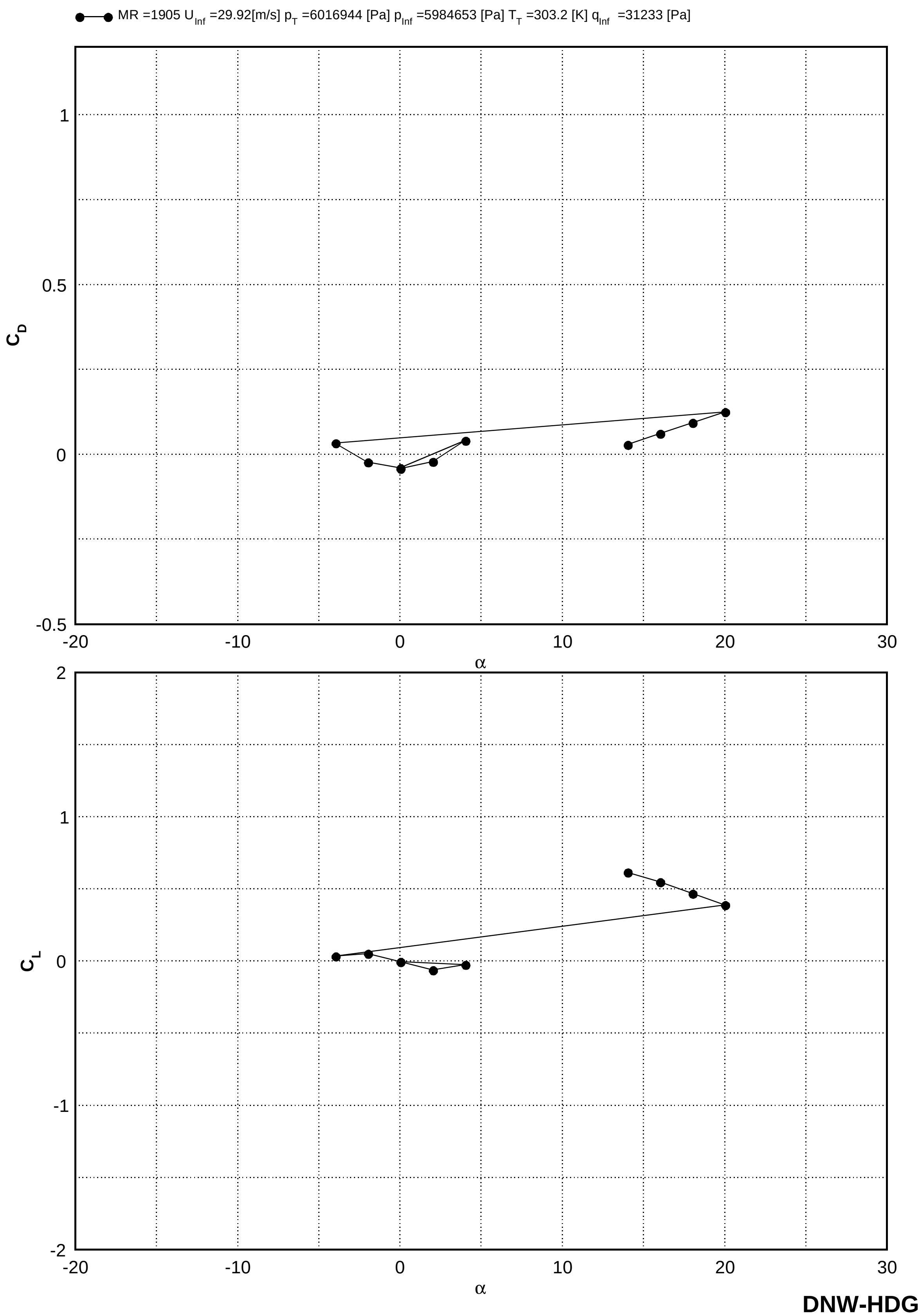


**Figure 19** 2'nd Cylinder Re= 4.062 [Mio] Pk=60bar

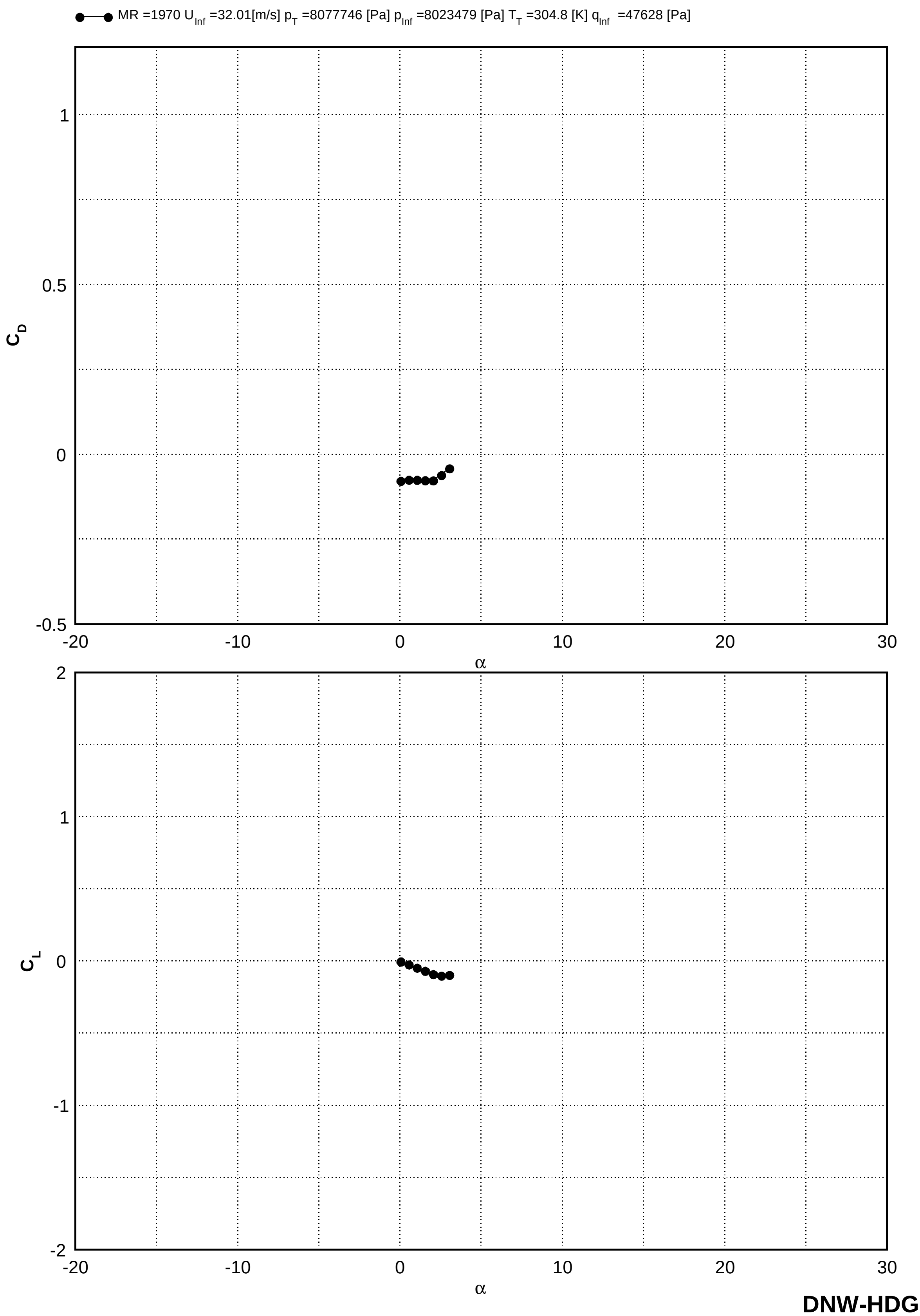


**Figure 20** 2'nd Cylinder Re= 5.641 [Mio] Pk=80bar

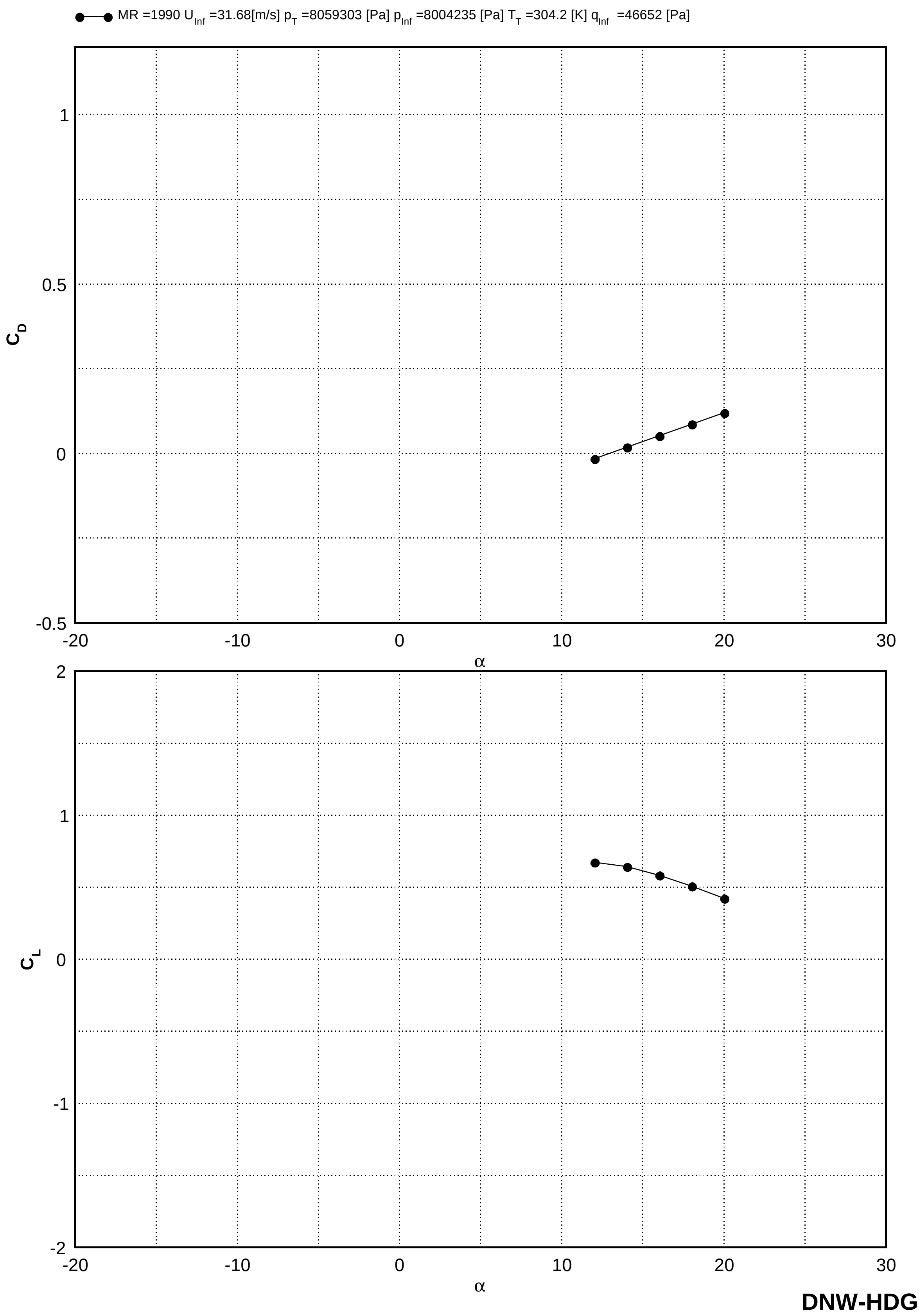


**Figure 21** 2'nd Cylinder Re= 5.591 [Mio] Pk=80bar

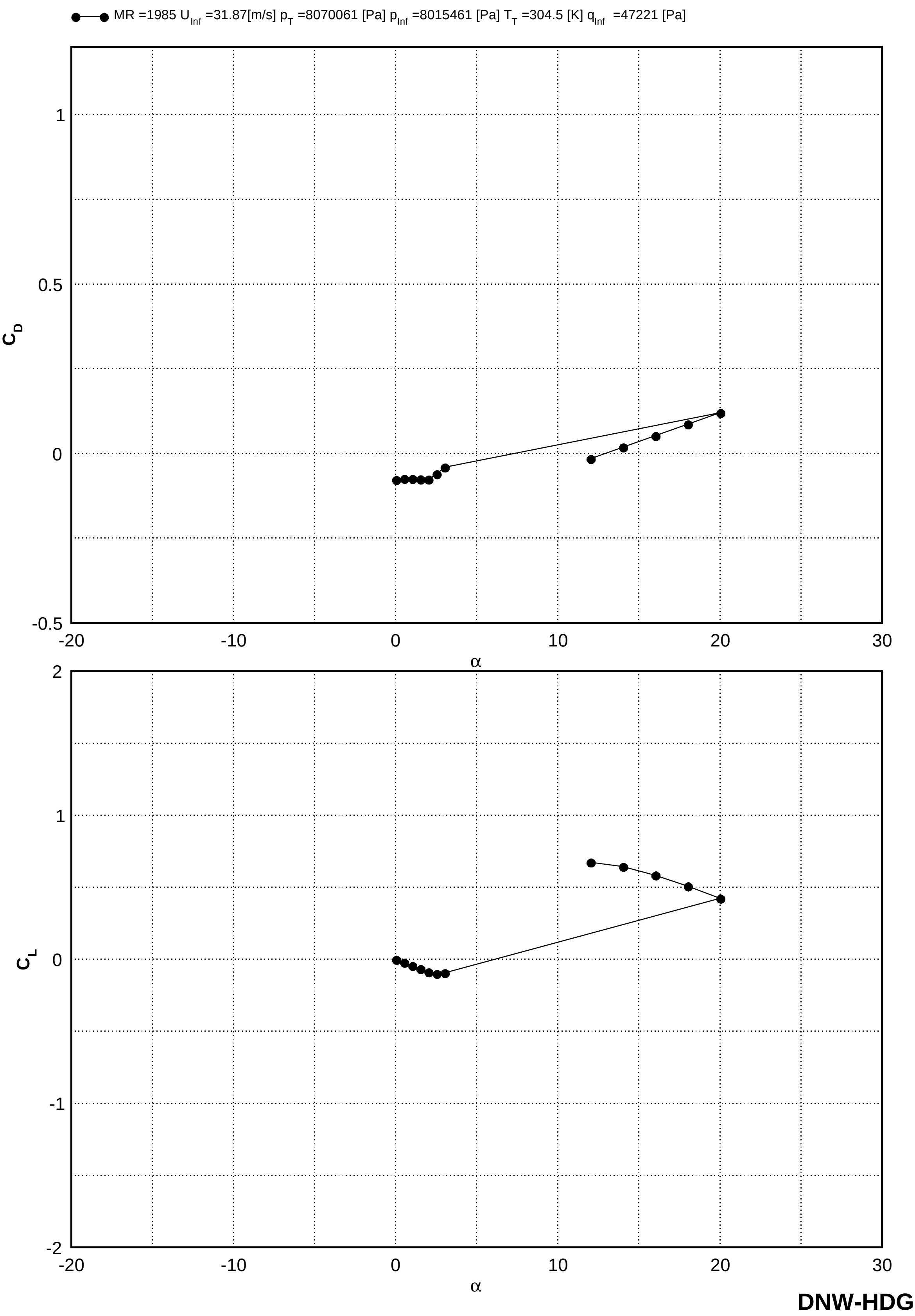


**Figure 22** 2'nd Cylinder Re= 5.620 [Mio] Pk=80bar

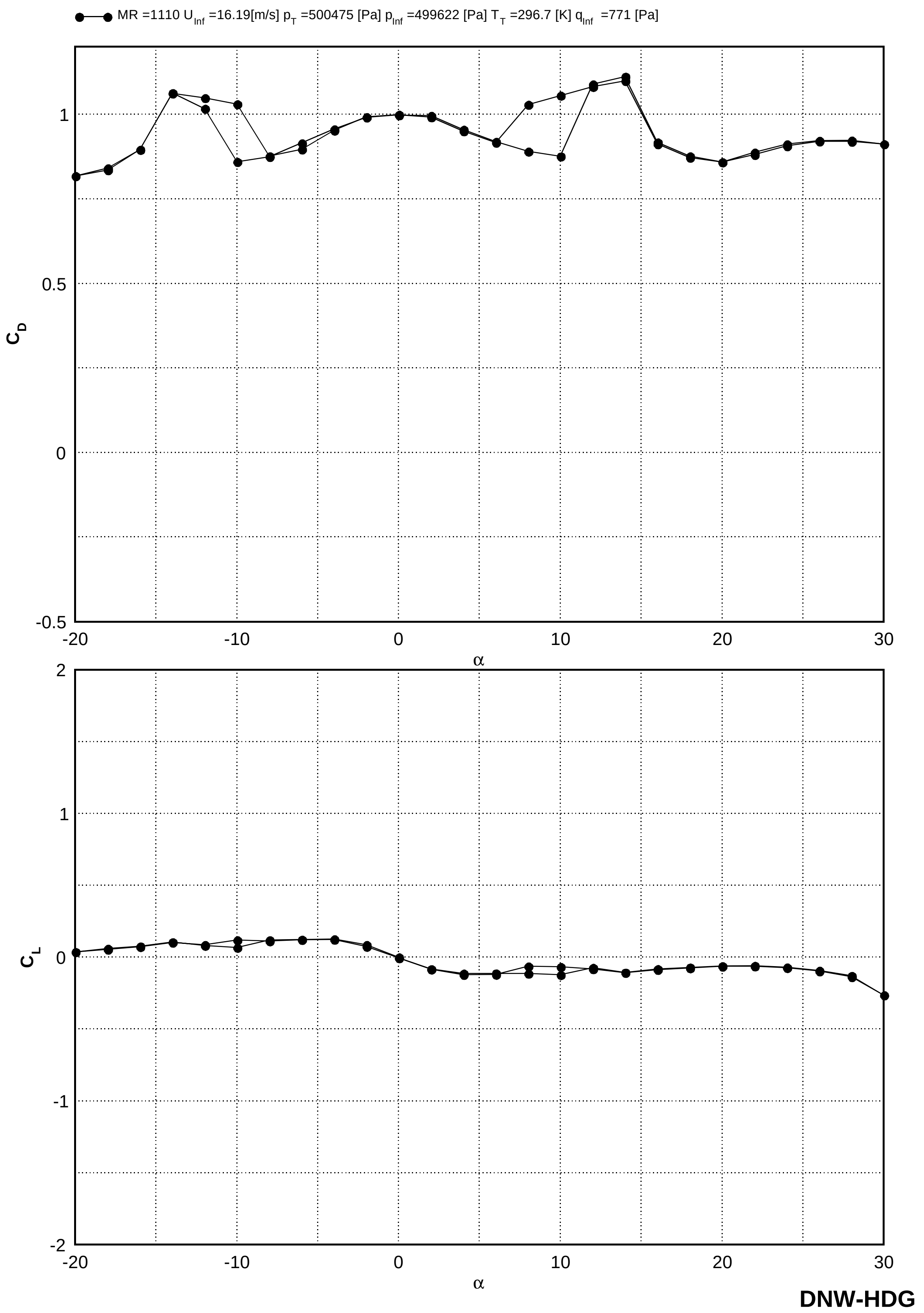


**Figure 23** 1'st Cylinder Re= 0.199 [Mio] Pk=5bar_vl

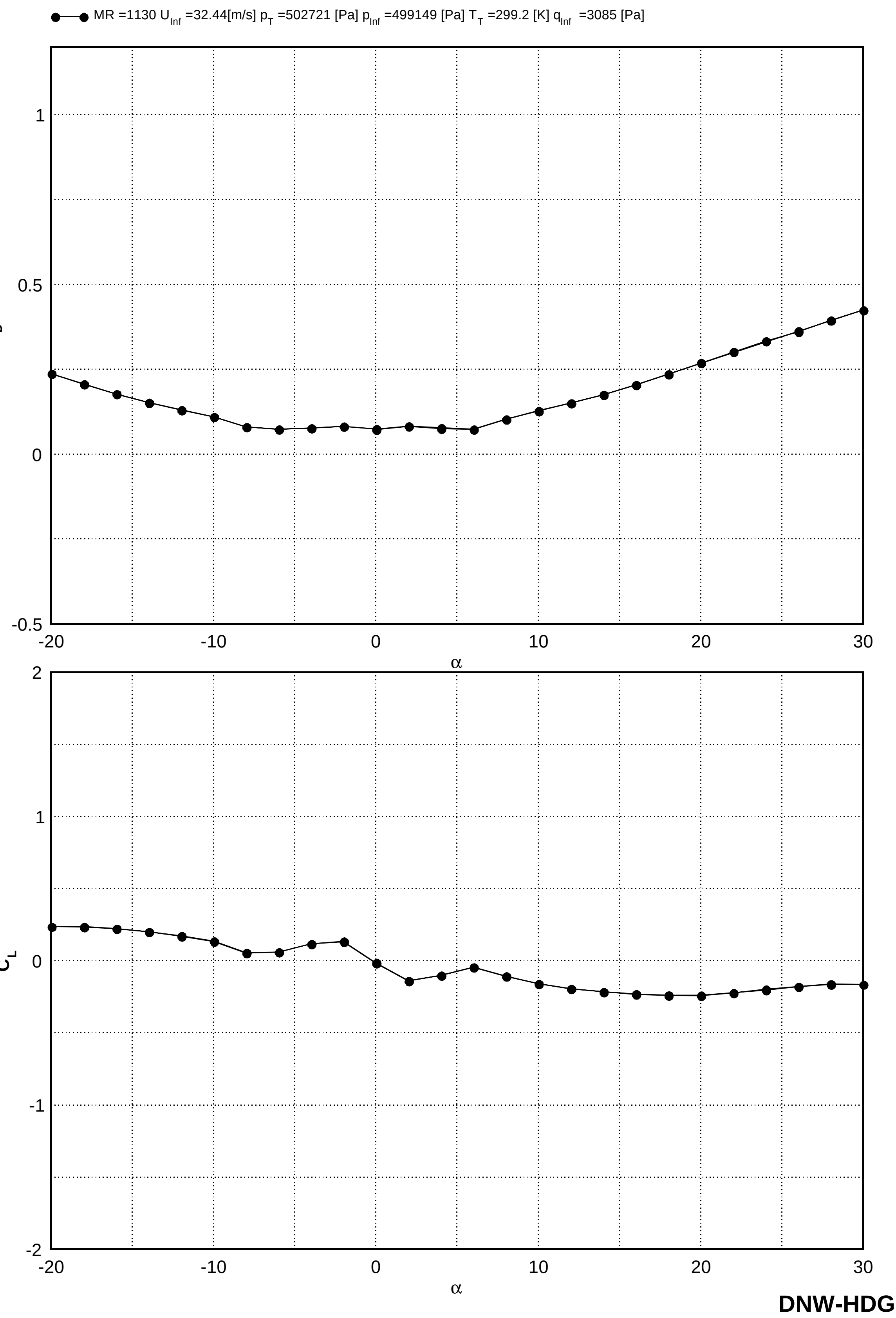


**Figure 24** 1'st Cylinder Re= 0.395 [Mio] Pk=5bar_vl

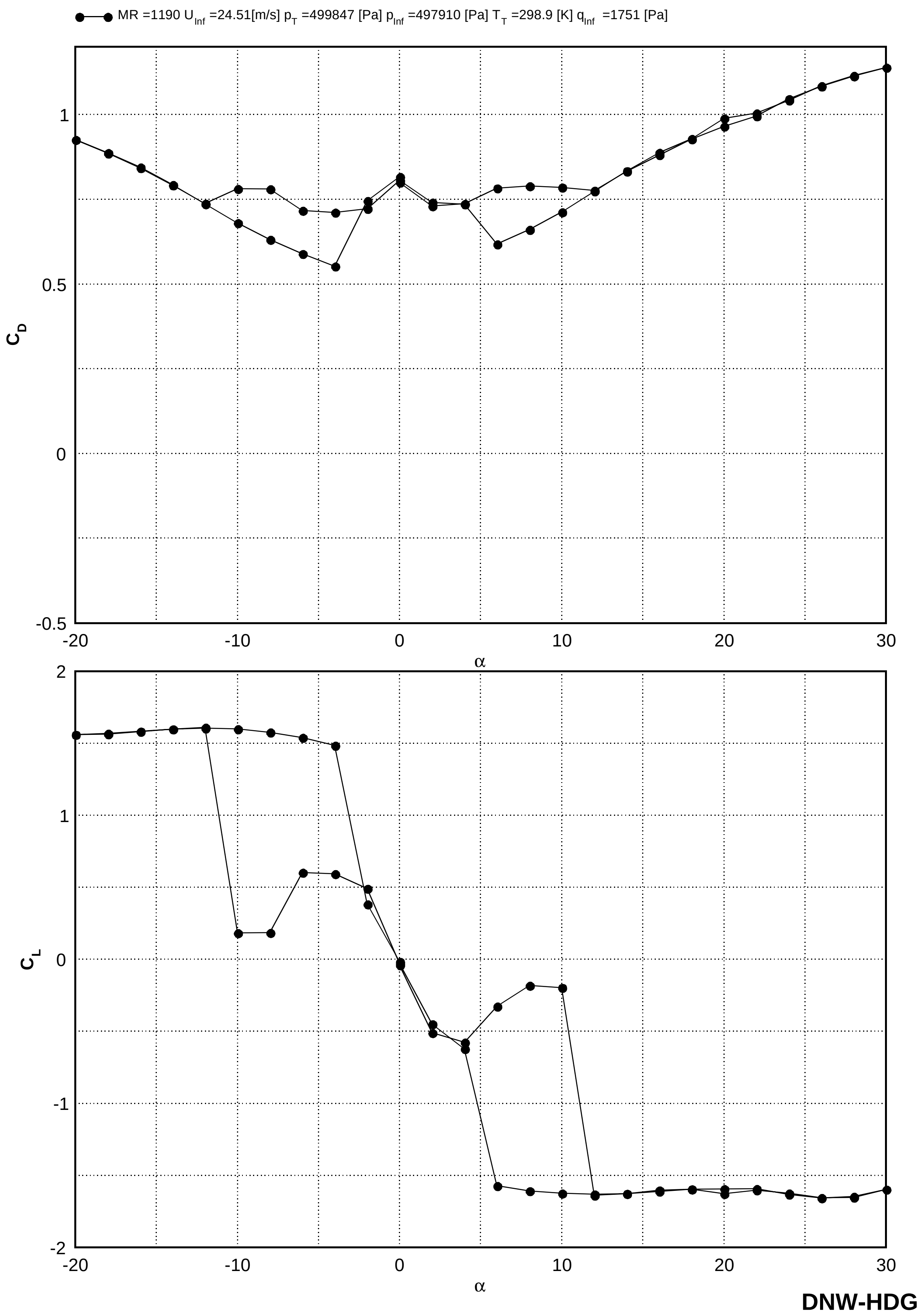


**Figure 25** 1'st Cylinder Re= 0.297 [Mio] Pk=5bar_vl

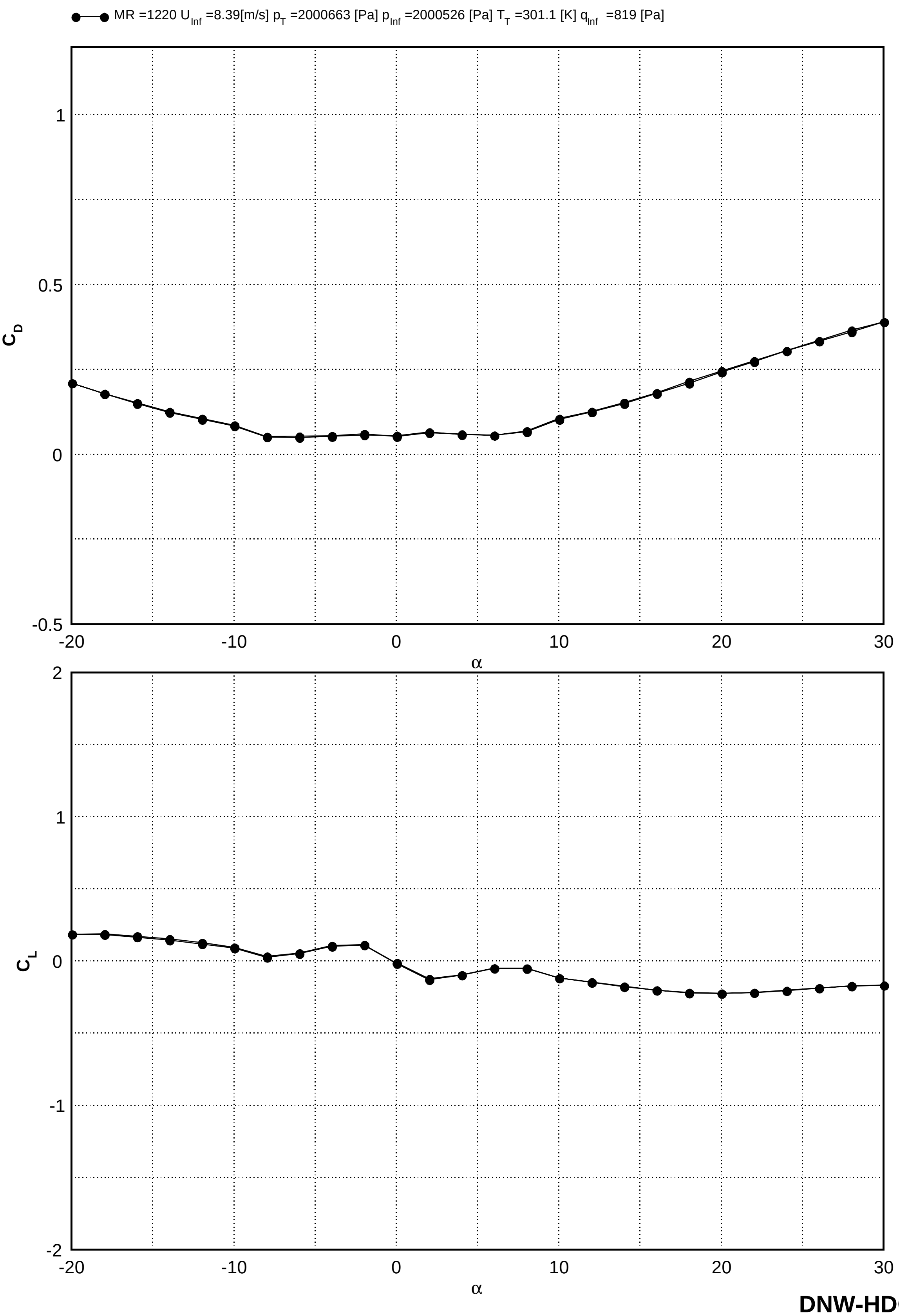


DNW-HDG

**Figure 26** 1'st Cylinder Re= 0.398 [Mio] Pk=20bar_vl

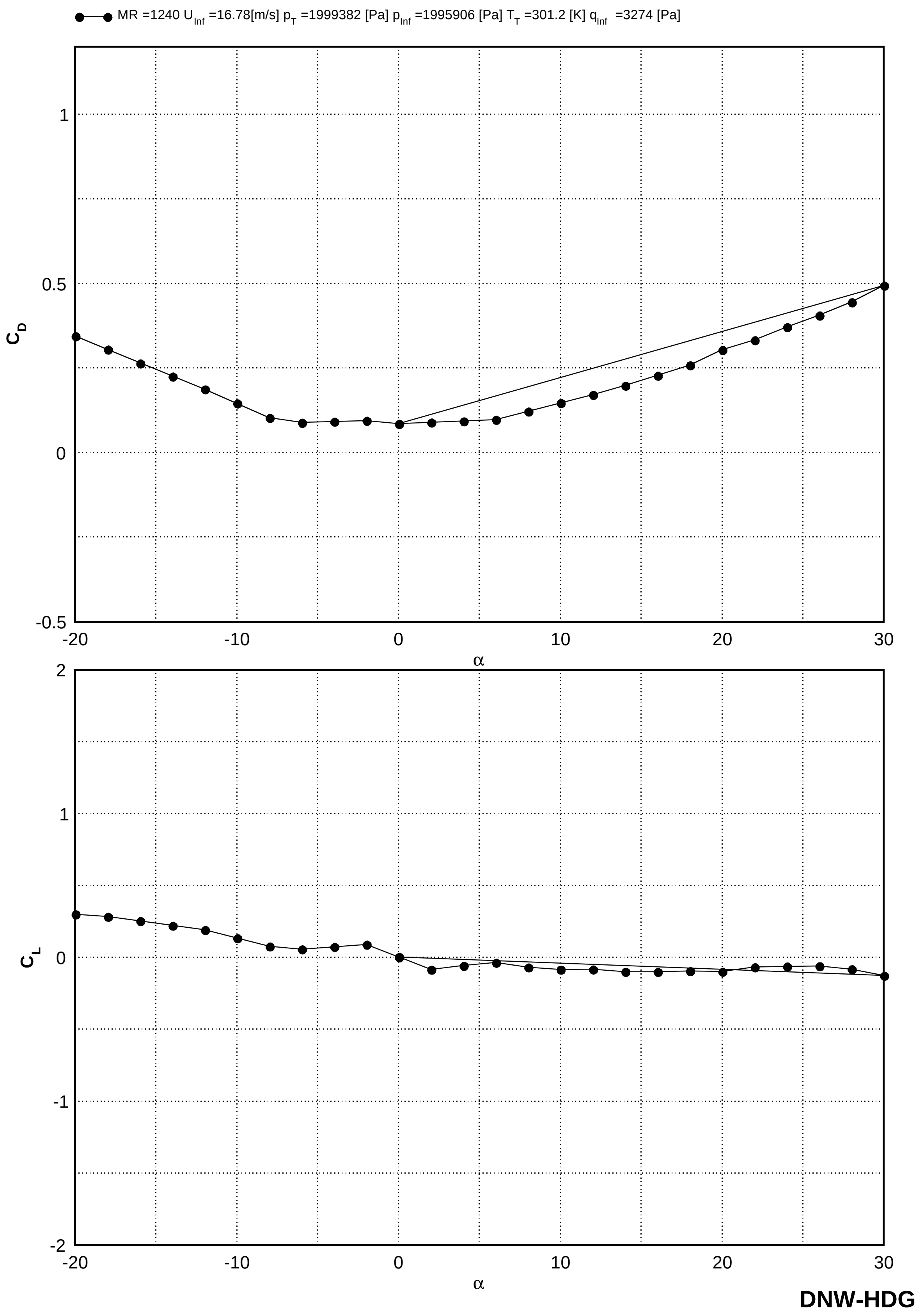


**Figure 27** 1'st Cylinder Re= 0.795 [Mio] Pk=20bar_vl

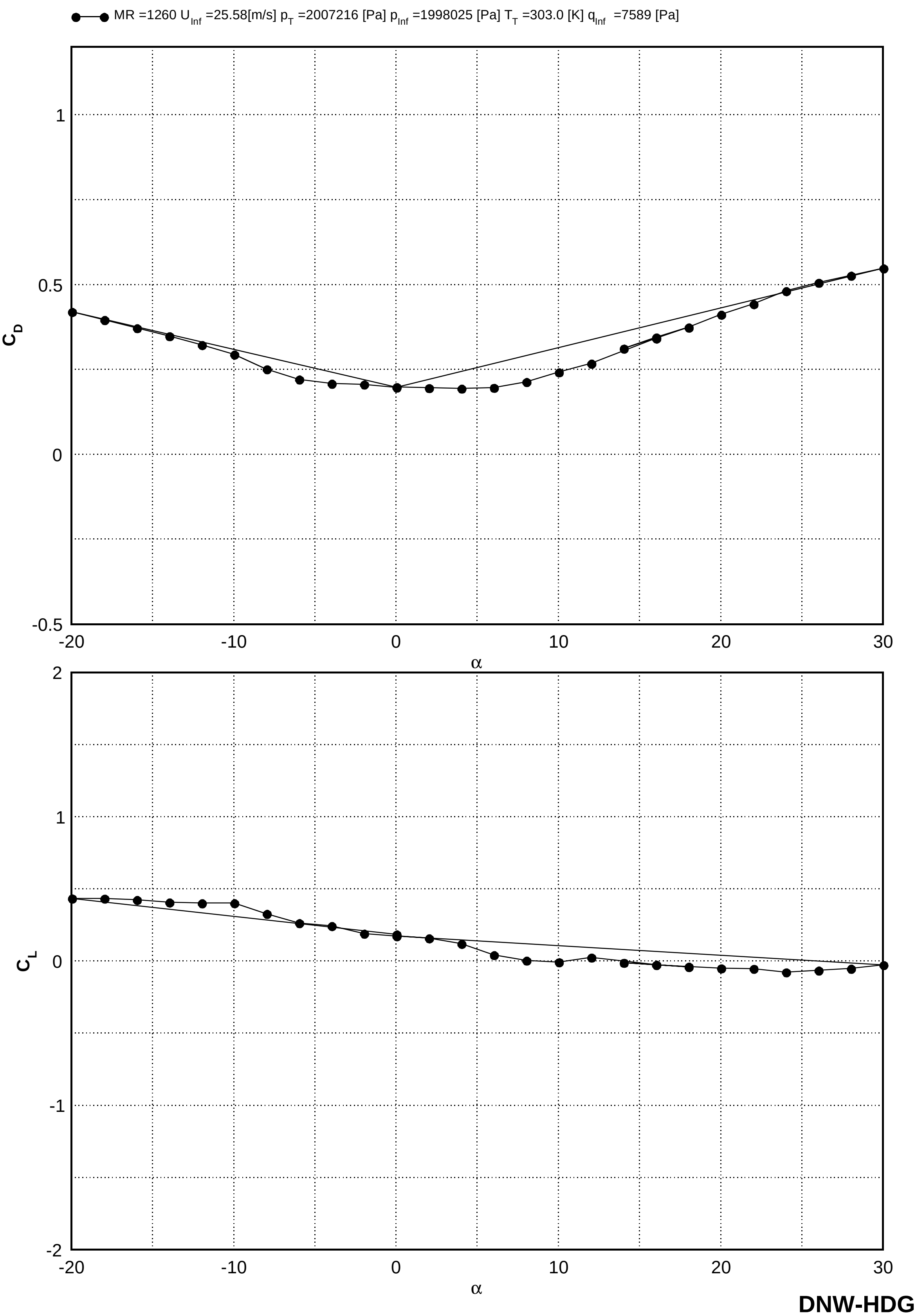


**Figure 28** 1'st Cylinder Re= 1.204 [Mio] Pk=20bar_vl

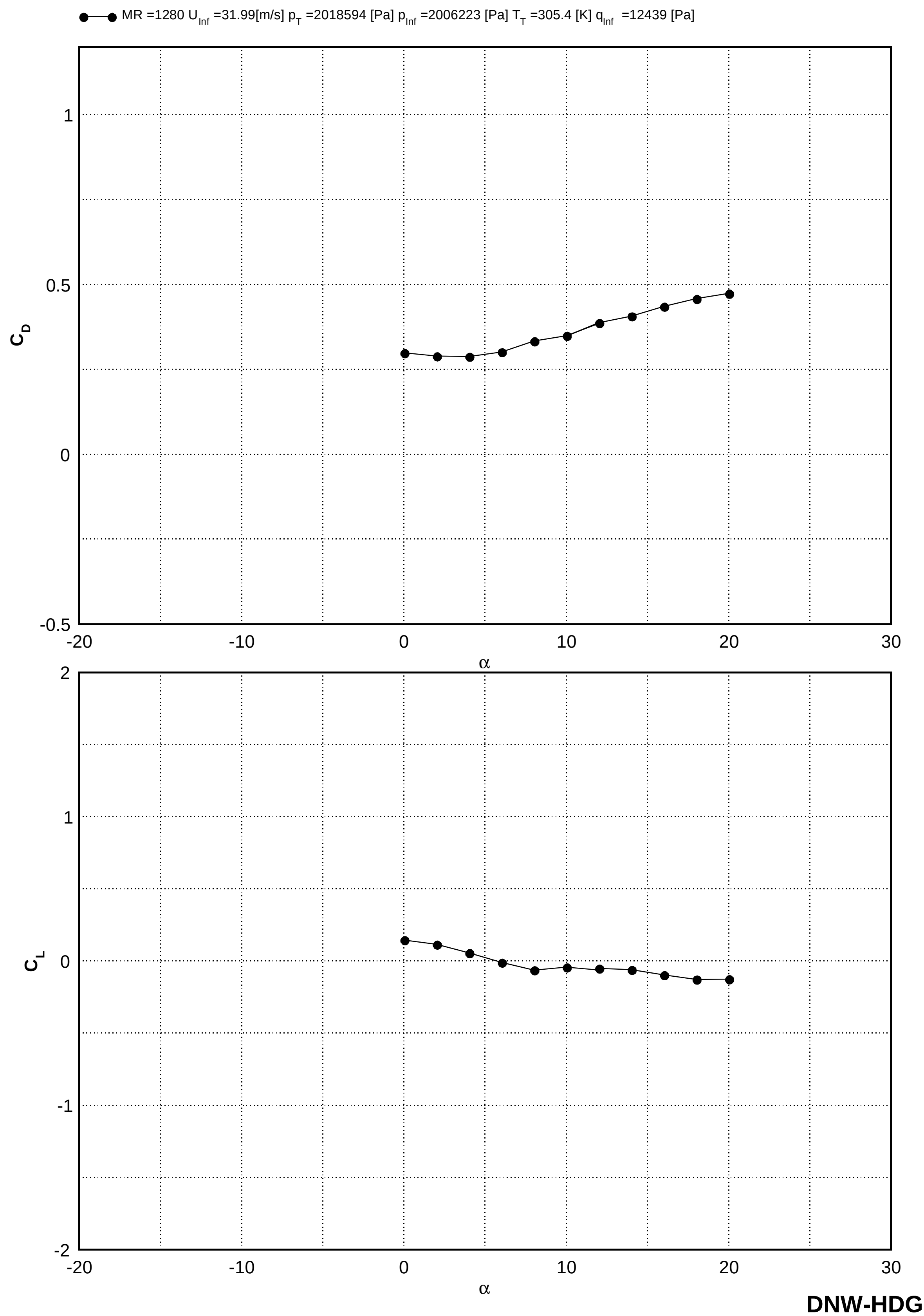


**Figure 29** 1'st Cylinder Re= 1.493 [Mio] Pk=20bar_vl

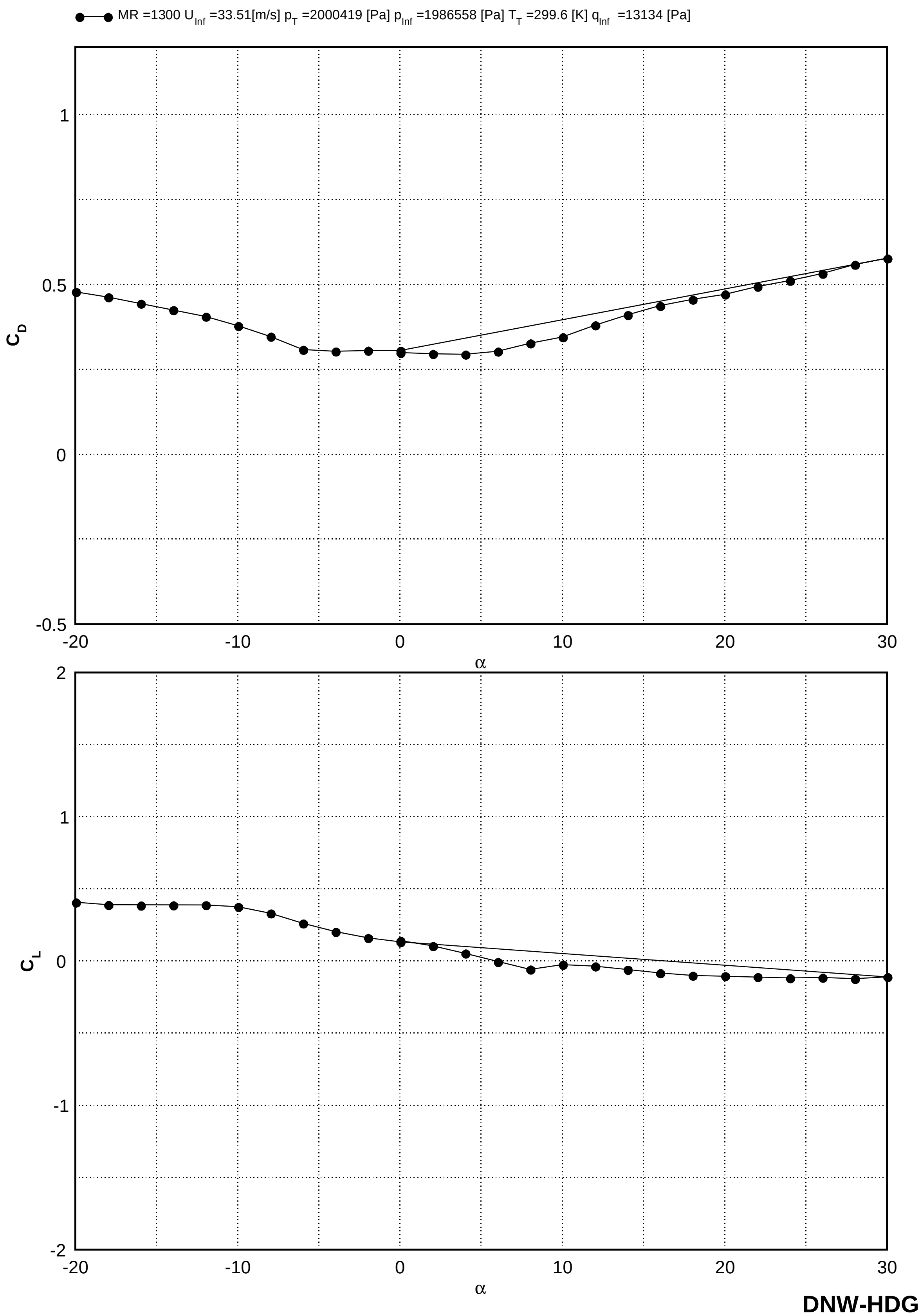


**Figure 30** 1'st Cylinder Re= 1.603 [Mio] Pk=20bar_vl

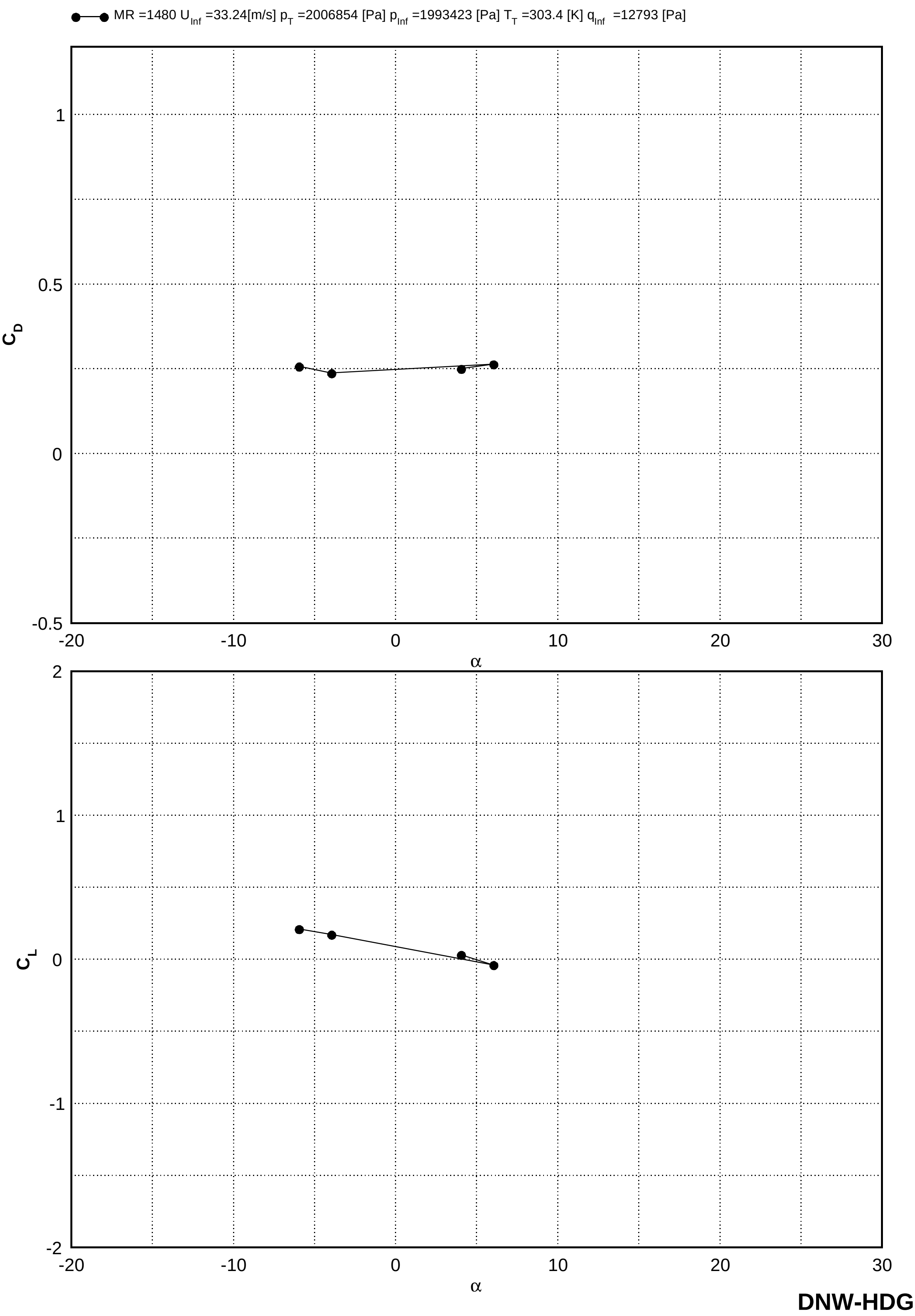


**Figure 31** 1'st Cylinder Re= 1.561 [Mio] Pk=20bar_vl

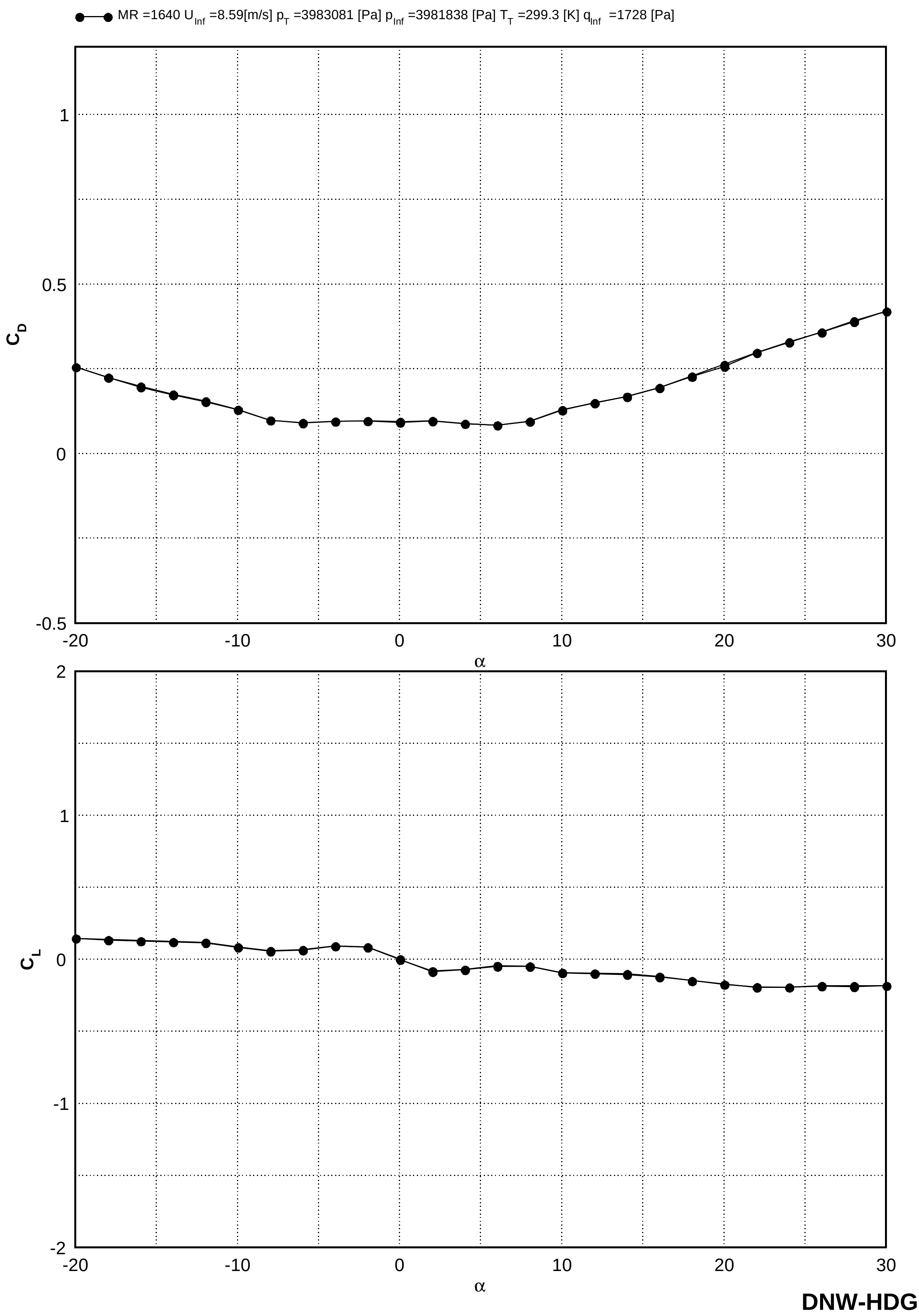


**Figure 32** 1'st Cylinder Re= 0.806 [Mio] Pk=40bar_vl

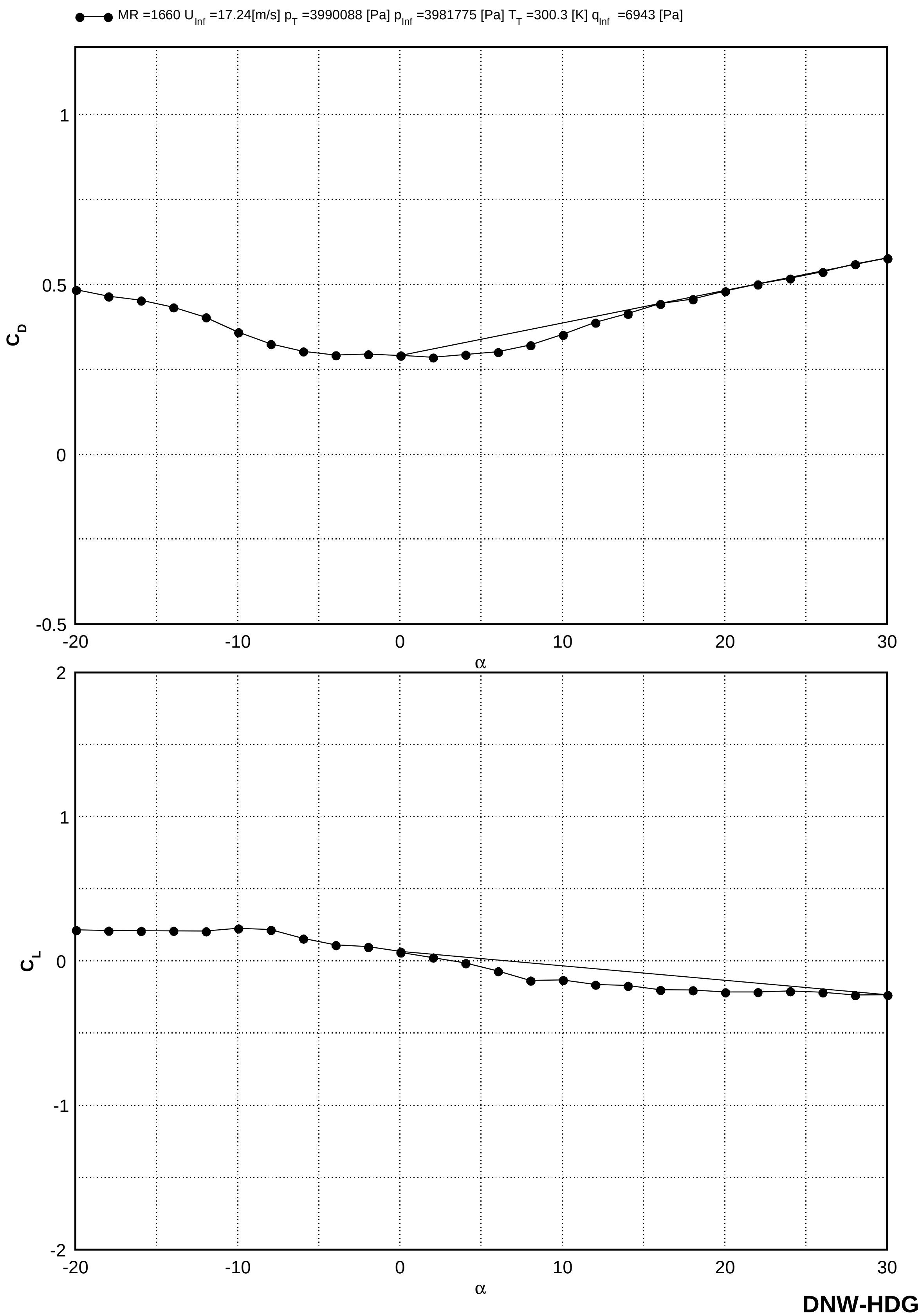


**Figure 33** 1'st Cylinder Re= 1.612 [Mio] Pk=40bar_vl

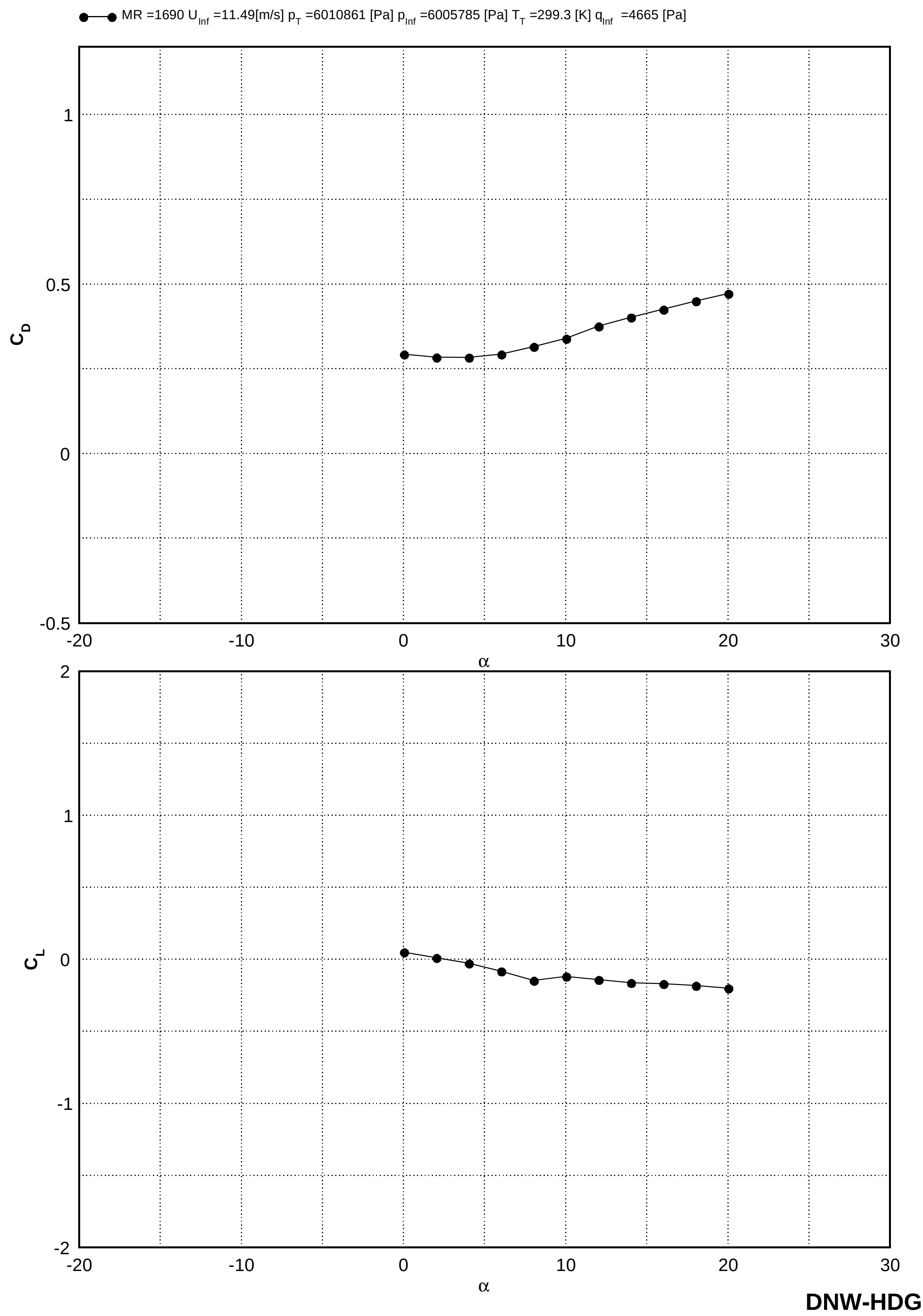


**Figure 34** 1'st Cylinder Re= 1.592 [Mio] Pk=60bar_vl

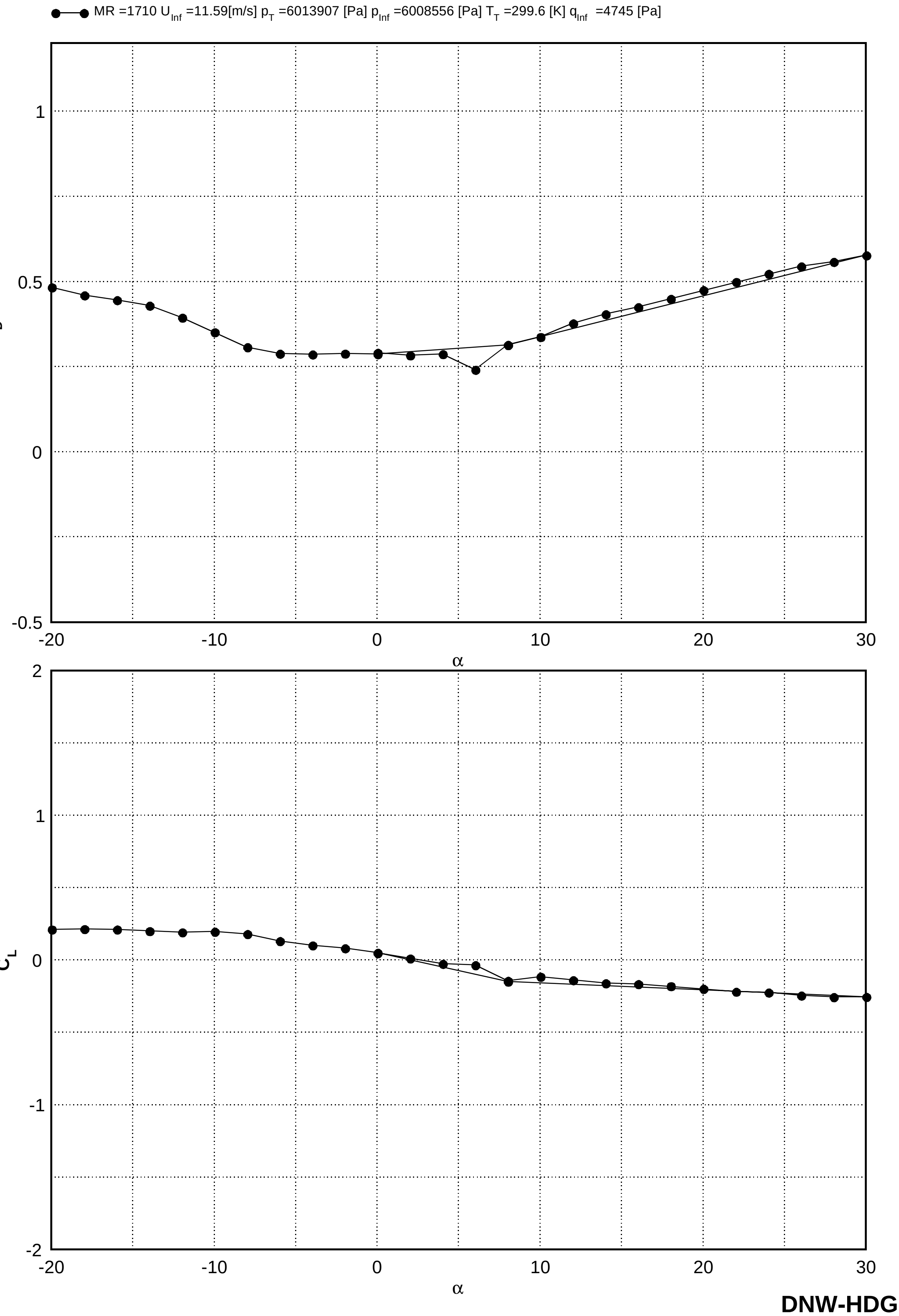


**Figure 35** 1'st Cylinder Re= 1.605 [Mio] Pk=60bar_vl

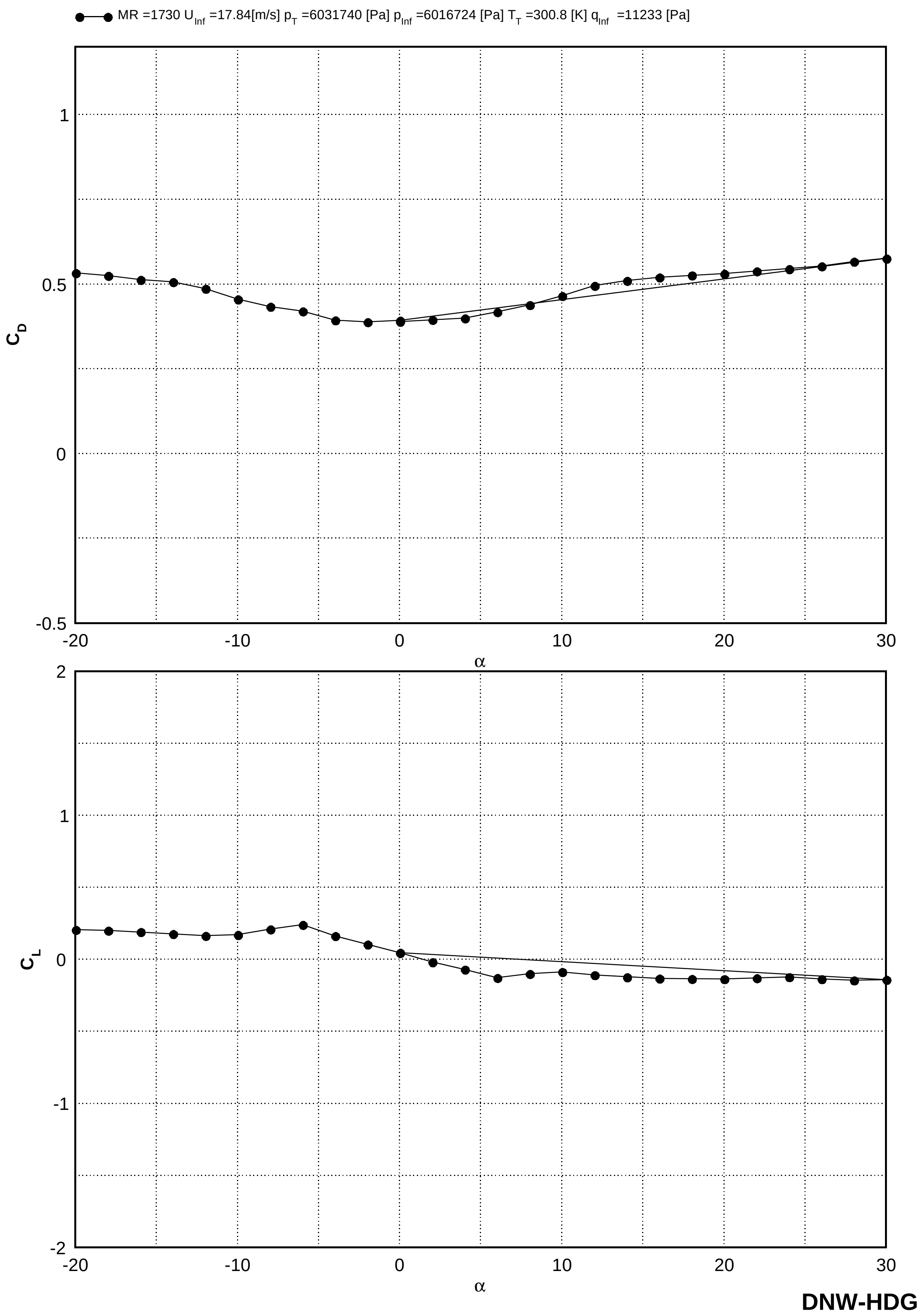


**Figure 36** 1'st Cylinder Re= 2.461 [Mio] Pk=60bar_vl